Departament de Física i Enginyeria Nuclear
Escola Tècnica Superior d'Enginyeria Industrial de Barcelona
Universitat Politècnica de Catalunya

Absolute quantification in brain SPECT imaging

Thesis presented by Albert Cot Sanz

15 June 2003

Thesis directors:
Dr. Francisco Calviño
Dr. Domènec Ros
Dr. Josep Sempau

CONTENTS

LIST OF FIGURES

LIST OF TABLES

Part I

THESIS

1. INTRODUCTION

"Extraction of the Stone of Fools"
painted by Jheronimus Bosch in XV^{th} century

1.1 Nuclear Medicine

The golden inscription shown in the picture which is difficult for a modern reader to decipher, runs: "Meester snijt de keye ras / Myne name is lubbert das" (Master, cut the stone out quickly. My name is Lubbert Das). In the Middle Ages the expression "he has

a stone in the head" was used to mean that someone was crazy. So Lubbert wanted to be cured of his folly as soon as possible. What the surgeon was removing from the head, however, is clearly not "the stone of folly" but a flower, like the one lying on the table. Bax [5] tried to explain the connection between the stone and the flower by referring to identify the flower as a tulip which has the connotation of stupidity. There are a number of other striking elements in the work too: the inverted funnel on the head of the surgeon, the book on the woman's head, the jug hanging from the surgeon's belt, and the clogs beneath the chair. If these objects had a symbolic meaning at the time, it unfortunately eludes us so many centuries later.

Certainly, the diagnostic tools available nowadays provide us a different concept about the basis and causes of neurological illnesses. The use of radiolabelled compounds for scintigraphic detection of metabolic functions or diseases has achieved worldwide recognition in medicine and biology. The study of properties of organs and tissues is performed by successful labelling of compounds of biological interest which has led to a new scientific field: the Nuclear Medicine.

The main elements found in biomolecules are essentially Carbon, Hydrogen, Oxygen and Nitrogen. Although obtaining of radionuclides of these elements by means of a cyclotron was achieved in the 1960s, their short half-life (minutes) and the high energy of their emitted gammas was too much of a difficult challenge for the technology of the time. Therefore, the PET technique did not become available in clinical routines until the 1990's.

Meanwhile, inorganic elements which allowed the in-vivo study of biological pathways were obtained by advanced radiochemical methods. The availability of the radionuclide ^{99m}Tc and the development of the gamma camera by Anger [2] led to the rapid development of Single Photon Emission Tomography (SPECT). This technique has been a major field in Nuclear Medicine since the 1970's [12]. ^{99m}Tc offers three main advantages: a sufficiently long half-life (6 hours), a wide range of complex molecules to which it can be linked and it has a simple decay scheme (solely a low energy photon with an energy of 140 keV). Furthermore, other ^{99m}Tc-labelled compounds such as the inorganic radionuclides ^{131}I, ^{67}Ga, ^{201}Tl, ^{133}Xe, ^{123}I have been used since the SPECT technique [53]. The use of these inorganic elements has originated different scientific disciplines of interest.

Important clinical diagnostic applications of the SPECT imaging technique are cardiology, oncology and neurology. In these fields SPECT is able to non-invasively visualize and analyze different organs and tissues functions or properties. For example, organ perfusion (i.e. ^{99m}Tc-HMPAO for brain perfusion), metabolic function (i.e. ^{123}I-fatty acids have been used to successfully study beta-oxidation of myocardial cells), receptor/transporter density evaluation (i.e. targeting the dopamine presynaptic transporter with ^{123}I-FP-CIT) and drug delivery among others.

1.2 Neurotransmission brain SPECT imaging

Many forms of brain diseases are associated with problems in the neurotransmission systems. One approach to the assessment of such systems is the use of SPECT brain imaging. Neurotransmission SPECT has become an important tool in neuroimaging and is today regarded as a useful method in both clinical [80, 68] and basic research [1]. There are two important reasons for this:

1. It has so far not been possible to view neurotransmitters *in vivo* by other means than PET or SPECT imaging techniques.

2. SPECT is a widely accessible and cost-efficient technique.

Despite controversy about whether or not SPECT imaging of dopamine uptake sites can replace PET imaging in neurological disorders [81], some authors support the view that, at least in clinical settings, SPECT imaging can replace PET imaging for the presynaptic dopaminergic function in Parkinson's disease (PD) [33].

Parkinson's disease (PD) is a progressive disabling neurodegenerative disorder observed in 1% of the population older than 55 years, the mean age at which the disease is first diagnosed [86]. PD consists of a syndrome including tremor, rigidity and postural abnormalities. One of the principal anatomopathologic characteristics of PD is the progressive loss of pigmented melanistic neurons, particularly loss of dopaminergic neurons in the *substantia nigra pars compacta* [41].

The dopaminergic system is one of the neurotransmission systems which may be studied by SPECT techniques. The presynaptic dopaminergic function is associated with the dopamine transporter (DAT). The DAT is responsible for re-uptake of dopamine from the synaptic cleft and it has been shown to be a sensitive indicator of nigrostriatal dopamine function. Dysfunctions of the presynaptic dopaminergic system are involved in PD and, as a consequence, DAT imaging is a useful tool to confirm or exclude PD [80]. A number of cocaine analog SPECT agents, which bind to DAT sites, have been developed [80]. These analogues include ^{123}I agents, such as the recently available FP-CIT [59] or ^{99m}Tc agents such as TRODAT [42].

In the past two decades, the strategy of symptomatic treatments has been improved and deep stimulation surgery has become an effective alternative for motor fluctuations and dyskinesia due to medical treatment. The issue for our new century will be the development of neuroprotective therapeutics aimed at slowing or stopping the degenerative process. This aim stresses the need for very early diagnosis of PD [69].

1.3 SPECT Quantification

Although visual inspection is often sufficient to assess DAT imaging, quantification might improve the diagnostic accuracy of SPECT studies of the dopaminergic system [26, 70]. In particular, quantification of DAT SPECT studies in PD could help us to diagnose this disease in the early pre-clinical stages. One of the main research topics in SPECT is to achieve early diagnosis, indeed preclinical diagnosis in neurodegenerative illnesses. In this field detailed analysis of shapes and values of the region of interest (ROIs) of the image is important, thus quantification is needed. Quantification also allows a follow-up of the progression of disease and to assess the effects of potential neuroprotective treatment strategies.

Quantification is affected by the degradation of the image introduced by statistical noise, attenuation, collimator/detector response and scattering effects. Some of these degradations may be corrected by using iterative reconstruction algorithms, which thus enable a more reliable quantification.

Iterative reconstruction algorithms like maximum-likelihood expectation-maximization (ML-EM) [77] are attractive because they enable to account for Poisson distributions as statistical noise in the projection data. The ordered subsets expectation maximization algorithm (OS-EM) was proposed by Hudson et al. [39] as an improved algorithm from ML-EM.

OS-EM algorithm has led to a significant reduction in computing time with the result that iterative reconstruction algorithms are starting to be employed for attenuation correction in clinical practice. Moreover, present-day iterative algorithms include this correction using attenuation maps obtained from transmission scans.

However, other degradations may be corrected during the reconstruction step. Iterative algorithms also permit modelling of the projection process, allowing for correction of spatially variant collimator response and the photon crosstalk effect between transaxial slices (along the tomographic axis). Thus, our work will focus on the modelling of the collimator/detector response for the fan-beam collimator on multi-head systems which offers a good trade-off between resolution and noise. Moreover, a full 3D reconstruction with OS-EM algorithms will be developed instead of the 2D slice-by-slice reconstruction.

Finally, scattering has recognized to be one of the most significant degradation effects in SPECT quantification [24]. Nowadays this subject is an intensive field of research in SPECT techniques. There are different methods for scatter correction [16] and some empirical approaches based on experimental data have been used. Nevertheless, Monte Carlo techniques appear to be the most reliable way to include this correction.

Once all the degrading effects were corrected, the absolute quantification could be achieved, thus providing new significant information to clinical diagnosis. The quantification results should be evaluated in order to test their reliability and accuracy. To this end,

Monte Carlo simulations with virtual phantoms will be employed. The theoretical values of the phantoms will be compared with those values obtained from the quantification algorithms.

1.4 Objectives

The aim of this thesis is to achieve quantification of both absolute activity values and relative values of the reconstructed SPECT images. In order to achieve this goal, we have set the following objectives:

1. The study of an optimized Monte Carlo simulator for SPECT studies.

2. The modelling of the collimator/detector responses using Monte Carlo techniques. The resulting analytical functions which model the PSFs could be incorporated in the Monte Carlo simulator in order to accelerate the simulation.

3. The development of a full 3D reconstruction algorithm.

4. The development of a scattering correction method using Monte Carlo simulation and full 3D reconstruction algorithms.

5. The accuracy evaluation of absolute and relative quantitative results in the corrected images.

It is important to note that the application of the developed tools and methods on brain SPECT imaging, and specifically to neurotransmission studies presented in this thesis, is an application of the results and the accuracy obtained, but is not a restriction on other SPECT studies.

1.5 Contents of this thesis

Once we have introduced the aim of this thesis in Chapter 1, the contents are organized as follows. Chapter 2 describes the methodology of SPECT techniques. The Monte Carlo simulator is presented in detail in Chapter 3. Chapter 4 describes the PSFs of low energy photons using the Monte Carlo code PENELOPE for different collimator/detector configurations: both parallel and fan beam. In Chapter 5 the PSFs of high energy ^{123}I photons are analyzed using another version using the PENELOPE Monte Carlo code, which includes the effect of secondary particles. The modelled PSF functions are used in the Monte Carlo simulator in order to accelerate the simulation process in Chapter 6. Finally, we present a new full 3D iterative reconstruction algorithm with a Monte

Carlo-based scatter correction in Chapter 7. The assessment of the quantification of the reconstructed images is performed with a 3D volume evaluation of the regions of interest in neurotransmission SPECT studies. The thesis ends in Chapter 8 with a discussion of the proposed methods and some concluding remarks.

2. SPECT IMAGING

"The Anatomy Lesson of Doctor Nicolaes Tulp"
painted by Rembrandt van Rihn in 1632
"Definition of Autopsy (*Auto/opsis*): a seeing with one's own eyes"
Webster's Dictionary

2.1 Methodology used in SPECT

The SPECT technique may be split into two different steps. The first step is the process of measure, which consists of acquiring projections of emitted photons from a distribution source of unknown activity. The second step is the reconstruction of this projection data set in order to estimate the unknown activity distribution by compilation of the reconstructed images.

During the detection process several physical effects degrade the direct geometric projection of the emitted photons from the distribution source. Accordingly, it is very difficult to obtain high quality, quantitative accurate SPECT images without taking into account

such corrections. In this Chapter we present a detailed description of each effect and the means of using corrections in reconstruction.

2.2 The measure: SPECT gamma camera

A SPECT scanner uses a gamma camera to detect the photons emitted from the radiopharmaceutical distribution in the patient or the object. A modern gamma camera (see Figure 2.2) consists of several detector heads which contain a collimator and a detector. Each detector head is shielded by a lead layer in order to prevent the measure of background radiation from outside the field of view of the camera. The detector consists of a large-area with a thin (a few millimeters thick) NaI(Tl) crystal which converts the photon energy into a light beam. This light is then optically guided through the photomultiplier (PMT) system which converts the light into an electrical signal. Electronic circuits position the signal and accept or reject the detected event depending on its amplitude. Finally, the projection data set consists of a distribution of detected events in each detector head.

Fig. 2.1: The two-headed gamma camera available at the Nuclear Medicine department in the Hospital Clínic of Barcelona.

The SPECT study consists of a set of projections acquired at discrete angles about the patient. Most SPECT systems consist of one or more detector heads which are mounted on a frame in such a way that they can rotate about the patient. The distribution source of the projections is obtained by compilation of the reconstructed images. In order to reconstruct the final images, the acquisition of planar gamma camera images at a sufficient number of angles around the patient is needed. Because of the large field of view of these scintillation cameras (typically 25×50 cm), a significant portion of the patient can be examined in one scan. The scintillation detectors used in this way were

incapable of determining the direction of the incoming photons by themselves (this is the main difference with PET techniques —where the direction is determined by the Line Of Response (LOR) of the spatial coordinates of the annihilation photon impact—). This is the reason why SPECT system cameras are always provided with a collimator, similar to that of a photographic camera with a lens.

A collimator is usually a slab of lead with several tens of thousands of holes covering the entire detector surface. These holes are typically a few centimeters long and a few millimeters in diameter. Since few photons are able to go through the lead, mainly the photons that traverse the holes are detected. The elongated geometry of the holes ensures that the direction of the detected photons is well determined. This information is essential in order to reconstruct the distribution of the radiopharmaceutical. Unfortunately, this directional information is achieved at great cost, namely a tremendous loss of sensitivity (number of detected photons). The typical sensitivity of a gamma camera is $\sim 10^{-4}$, meaning that 1 out of 10,000 emitted photons will actually traverse the collimator and be detected. Accordingly, collimation is the main reason why counting statistics in SPECT images are poor.

The scintillation detector is currently the main technique for gamma radiation detection in Nuclear Medicine imaging. It is based on the emission of visible or near-visible light from scintillation crystals when energy is absorbed from ionizing radiation. This emission of light is a result of inelastic collisions between secondary electrons and other atomic electrons. The photo-multiplier (PM) tubes amplify the light and convert it into electrical pulses. A property of many inorganic scintillators is that light emission is proportional to the energy deposited in the material. This allows measurement of the detected photon energy.

A typical value of the energy resolution of scintillation detectors used in modern gamma cameras is about 10% for low energy windows (100-200 keV) [67]. This means one can discriminate only to a limited extent by applying a photo-peak window, between unscattered photons (primary photons) and photons which have scattered and have thereby lost energy. In order to collect a large fraction of primary photons, the width of this window has to be set normally 15-20% of the photo-peak energy. As a consequence, a significant part of the photons detected in the photo-peak window have undergone scattering, thus causing a blurring spot which spoils the final image.

2.2.1 Image degrading effects in SPECT

The detection of photons in SPECT is seriously affected by collisions within the patient or object (photon attenuation and scattering), and the inevitable inaccuracy of the collimator (collimator blurring). The images are also severely degraded because of noise, partly due to the collimation reduction of accepted photons. Accordingly, it is very difficult to obtain

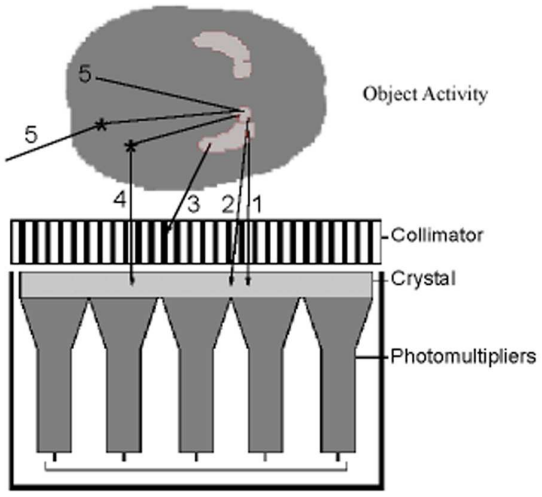

Fig. 2.2: Schematic view of the acquisition of a projection using a gamma camera. The scatter interactions within the patient are represented by $*$. Photon 1 and 2 are directly detected, although photon 2 entered under a slight angle from the collimator hole axis, causing blurring of the projection. Photon 3 is rejected by the collimator. Photon 4 is detected after scattering. Photons 5 are not detected due to scatter and photoelectric interactions within the body which cause the attenuation effect.

high quality, quantitatively accurate SPECT images without taking into account such corrections. As we will show in the following subsections, each factor is a well-understood physical phenomenon, and therefore corrections can be included in the reconstruction algorithm for each of these image degrading effects.

Attenuation

The interaction of photons in the patient or the attenuation media diverts the photon path to the detector (see photon 2 in Figure 2.2). This causes attenuation of photon flux directed towards the detector and it decreases the signal.

The interactions of photons with matter are described mainly by four processes: photoelectric absorption, Compton scattering, coherent scattering (Rayleigh) and pair production. Each process will occur with a probability which strongly depends on parameters such as photon energy and the object attenuation map. The total probability for the occurrence of any of the processes is therefore the sum of the cross-sections of the different effects. Figure 2.3 shows the cross-sections of the aforementioned interactions and the total cross-section. From Figure 2.3 it is clear that for photons with an energy of 50-1000

keV, the most probable interaction process is Compton scattering. In heavier materials such as the collimator lead and at at low energies (below 100 keV), photo-electric absorption also becomes significant. Pair production is a typical effect used in PET radiotracers where two annihilation photons are generated. However, below 1022 keV this effect does not appear. Hence, Compton scattering and photo-electric absorption are the relevant effects to be modelled for an accurate description of photon interaction in SPECT. However, coherent scattering may also contribute to blur the image due to its high probability at low angles of scatter (near 0^o) and high energies [45].

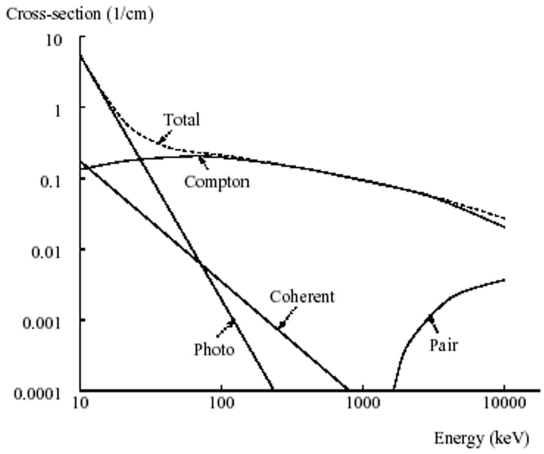

Fig. 2.3: Differential cross-sections for the photo-electric effect, Compton scattering, coherent scattering and pair production and total cross-section for water as a function of photon energy.

Attenuation is mainly the result of Compton scattering (and some photo-electric interaction) and depends on the total length of the tissue which has to be traversed, the type of material and the photon energy. The attenuation of a narrow beam of photons passing through a non-homogeneous medium of thickness d is given by:

$$\psi \;=\; \psi_0 \exp(-\int_0^d \mu(r)dr) \tag{2.1}$$

where ψ is the photon flux after attenuation, ψ_0 is the incident photon flux and μ is the linear attenuation coefficient (the total sum of all possible differential cross-sections). For water, the linear attenuation coefficient μ is approximately 0.152 cm^{-1} for 140 keV gamma rays [54].

Collimation blurring

As shown in Figure 2.6 the image of a point source in air through a collimator/detector system is a spot, a 3D distribution called the Point Spread Function (PSF). The PSF does not depend on the object attenuation map but varies with the collimator/detector configuration and the photon energy.

The PSF is described by two variables: Firstly, the sensitivity S, which is defined as the number of photons detected per emitted photon. It is calculated as the ratio between the sum of counts under the PSF volume and the number of photons emitted by the source. The other variable, resolution, equals the Full Width at Half Maximum (FWHM) of the image corresponding to a point source. The FWHM may be modelled for low energy photon PSFs as a Gaussian function which contains two contributions: the collimator resolution and the intrinsic resolution of the detector as described in equation (2.2).

$$FWHM \;=\; \sqrt{FWHM_c \;+\; FWHM_i} \tag{2.2}$$

The intrinsic resolution of the detector may be described by means of a Gaussian distribution with a full width at half maximum (FWHM) that is proportional to the square root of the deposited energy [47].

Because the collimator holes are not infinitely narrow and their septa walls may be crossed by certain photons (the probability of crossing the septa wall is larger for higher photon energies), the photons that traverse the collimator will not all come from a direction that is exactly aligned with the holes. This leads to a substantial loss of resolution in the gamma-camera images and in the reconstructions. A collimator design with a higher width or septa wall (distance between holes) would decrease the collimator blurring but would also greatly reduce the sensitivity of the collimator. It can be shown that a twofold increase of the collimator resolution, would decrease the sensitivity by a factor of about 4. Therefore, a compromise has to be found between collimator resolution and sensitivity. Since the collimator resolution depends on the distance between the source and the camera, it is important to position the camera as close as possible to the patient or to use a focused collimator such as the fan beam type collimator. Accurate mathematical descriptions of collimator blurring can be found in [56, 83, 32] by modelling different collimator PSFs.

Each clinical study has different requirements: field of view (FOV), radiopharmaceutical tracer, organ or tissue to be imaged and associated dose. Thus, the best collimation methodology differs for each type of study. Therefore, several types of collimators have been developed to achieve an adequate compromise between spatial resolution and sensitivity. As shown in Figure 2.5, collimators are classified depending on the geometrical design of the hole array.

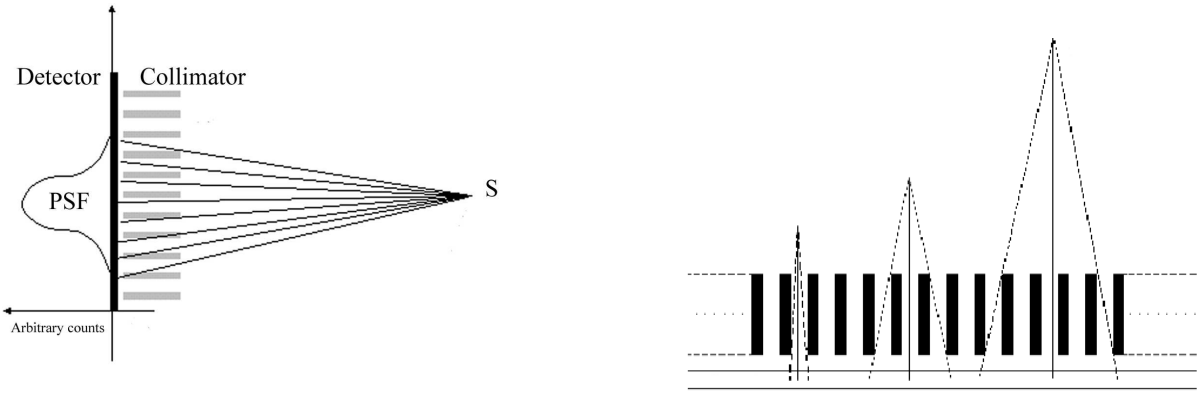

Fig. 2.4: PSF response for a parallel collimator. Same sensitivity and different resolution at different heights for a parallel collimator.

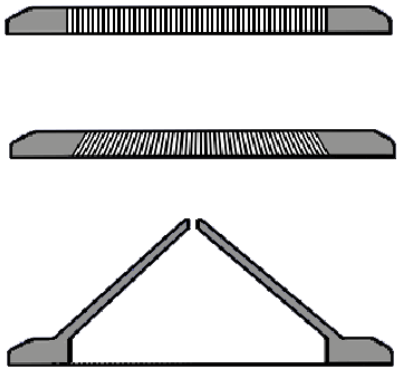

Fig. 2.5: Different collimator configurations used in SPECT imaging. Above there is the parallel collimator and below the convergent type: fan beam collimator and pin hole collimator.

Another design variable for collimators is the energy of the collimated photons. For cardiac imaging with low energy (^{99m}Tc, ^{201}Tl, ...) tracers, the usual collimators are Low Energy All-Purpose (LEAP). In brain SPECT imaging image resolution is a major objective, thus Low-Energy High Resolution (LEHR) collimators are used. Finally for medium- or high-energy rays (^{131}I,...) Medium Energy (ME) is the best choice.

In general, the most widely used collimator for SPECT studies is the parallel collimator. However, convergent fan-beam collimators are designed in order to focus the holes through a focal line. This design provides greater sensitivity and a wider area of detection. These advantages are especially indicated in order to improve SPECT brain imaging.

In this thesis we present a characterization of parallel and fan beam collimator PSFs at different energies by using Monte Carlo simulations. Furthermore, PSF responses were calculated for different source locations in order to model a PSF function for the reconstruction algorithms and the Monte Carlo simulator.

Scattering

An important image degrading effect in SPECT is the fact that photons which have suffered scattering processes enter the collimator/detector system. Scatter results in the detection of "incorrect" photons and is also the cause of the attenuation effect. These effects are shown in Figure 2.2.

A photon can penetrate matter without interaction or it can be absorbed and/or it can scatter and thereby lose a certain amount of energy. If a photon is scattered and then detected in the photo-peak (with a detectable energy window), this may lead to detection at a detector position which suggests an incorrect emission point (e.g. photon 4 in Figure 2.2). This causes severe degradation of the contrast and quantitative accuracy of the reconstructed image if scatter events are not corrected.

Compton scattering is an interaction between a photon and an atomic electron. Since the energy of the incoming photon is very high compared with the binding energy of the electron, the interaction can be interpreted as a collision between the photon and a free electron. The photon is scattered by an angle θ relative to its incident direction and loses energy which is then transferred to the electron. The scattered photon energy E'_γ is given by the Compton formula:

$$E'_\gamma = \frac{E_\gamma}{1 + \frac{E_\gamma(1-\cos\theta)}{m_e c^2}} \tag{2.3}$$

where E_γ is the incident photon energy and $m_e c^2$ is the rest energy of the electron. From the last equation it is evident that the maximum amount of energy is transferred to the electron when the photon is backscattered ($\theta = \pi$) and that little energy is lost

by the photon when $\theta \sim 0$. A comprehensive description of Compton scattering is given by [73]. For Nuclear Medicine applications, the angular distribution can be described by the Klein-Nishina approximation, which relates the differential cross-section $\frac{d\sigma}{d\Omega}$, or scatter probability, with the scatter angle θ.

Statistical Noise

The detection of photons in Nuclear Medicine is a Poisson process. The low detection probability $\sim 10^{-4}$ and the huge number of emitted photons from the radiotracer implies that measures of the projections also include Poisson noise. As an example, a 2 mCi injection of ^{99m}Tc-HMPAO for 30 minutes of acquisition emits 13.32×10^{10} photons. The probability of detection is about $\sim 10^{-4}$ due to the isotropic source emission, the finite number of detectors and the collimation phenomena. Therefore, 13.32×10^6 accepted photons will be split between about 2 million bin detectors (120 projections of 128×128 leads to 2×10^6 detector bins). Thus the detected photon number per bin is about 6 counts. The statistical result in the bin is $6 \pm \sqrt{6} = 6 \pm 2.5$ which provides an indication of statistical noise phenomena in Nuclear Medicine.

Since the variance of Poisson noise in the detector bin A is proportional to the mean of counts N_A of that particular projection bin, the acquisition of a high number of counts will increase the signal-to-noise ratio (SNR). The SNR is defined as the ratio between the noise (defined as the square root of the variance) over the mean:

$$SNR = \frac{\sqrt{Var(N_A)}}{N_A} = \frac{\sqrt{N_A}}{N_A} = \frac{1}{\sqrt{N_A}} \tag{2.4}$$

However, for several reasons the number of counts is small. Basically the detected counts are proportional to:

1. The length of scan. Decreasing the duration of the scan decreases patient discomfort and the possibility of patient movement. Usual data acquisition lasts longer than 30 minutes and the number of patients per day is a variable related directly with the cost of the hospital service.

2. The radiation dose injected to the patient. Radioactive isotopes are administered in sufficiently low doses so as not to affect the physiological process under study. Decreasing the radiation dose, likewise decreases number of counts, but also reduces costs and increases patient safety. The cost/benefit ratio has to be balanced.

3. The size of the detector bin. The detector is subdivided in pixels. Different configurations of pixel arrays are possible, usually 64×64 is the standard, whereas 128×128 is used for high resolution imaging demands (e.g. brain imaging). A larger pixel

would acquire a greater number of counts N_A, but this would mean poor resolution in the final image. Thus, a balance between resolution and SNR is also needed.

4. The number of camera heads. The gamma camera uses different rotating camera heads which detect radiation simultaneously. The greater the number of detector heads used, then the greater the number of counts it gets for the same scanning time. The limit of the number of heads obviously depends on geometry, and nowadays the maximum is three heads placed at 120º to each other.

The quality of a SPECT image is minimized to the point technically available ("As Low As Reasonable Achievable"). However, a low signal-to-noise ratio is inherent to a SPECT image and thus noise is a major cause of image degradation.

Other image degrading effects

Other instrumentation-related processes influencing the quality of SPECT images are non-linearities and non-uniformities of the detector and inaccuracy of the center of rotation of the detector. Correction methods for these effects exist. Therefore, their influence is relatively small compared with noise, collimator blurring effects, attenuation and photon scattering. Finally, image quality can be significantly affected by biological factors such as tracer kinetics and target specificity, and by patient and/or organ movement during image acquisition.

2.3 Reconstruction: SPECT algorithms

In the previous section 2.2 the gamma camera was described as the tool used in Nuclear Medicine to measure the signal. However in Nuclear Medicine scans the final result is not the projection data set but the reconstructed image. Therefore the image is obtained by using mathematical algorithms which process and reconstruct the projection data set on a computer.

The purpose of tomographic reconstruction is to obtain cross-sections of an object from projections of that object. In 1917 Radon showed the reconstruction of a 2D object from its 1D projections using an infinite number of directions [24]. Two different approaches are commonly used for SPECT reconstruction. Until recently, Filtered Back Projection (FBP) was the universal method because of its simplicity and speed. As soon as advanced computers appeared, a more accurate technique was implemented: iterative reconstruction. The latter technique permits modelling of all image degrading factors although it requires a much longer computational effort. The acceleration that has been achieved by designing fast codes and using advanced hardware has brought them within the range of clinical application over the last decade.

2.3.1 Iterative Reconstruction

In iterative algorithms, estimated projection data are generated by means of a forward projector using an initial estimate of the activity distribution (image). These calculated projections are compared with the measured projections. On the basis of this comparison, one can obtain a better estimate of the image using an update step. This process of forward projection, comparison and updating can be iterated until an acceptable image is obtained. The model of forward projection is represented by the transition matrix which is used in the iterative algorithm. The more accurately this transition matrix is modelled, the better the agreement will be between the estimated images and the real activity distribution.

SPECT projection data are severely affected by Poisson noise, which implies that low pixel count values give a less accurate prediction of the time-average photon flux received in the pixel. A possible way to model the Poisson nature of the measures is to treat the data as stochastic variables and not as exact measures; noise-free projections are taken as the mean of the Poisson distributions. Calculating the maximum likelihood estimate of the emission distribution that generated the measured projections takes into account the Poisson nature of the projections. Without making any a priori assumptions about the activity distribution, the statistically most likely emission distribution can be calculated using the Maximum Likelihood-Expectation Maximization (ML-EM) algorithm [77, 49]. The ML-EM algorithm updates all image elements s_i of the estimated image at iteration $k+1$ according to:

$$s_i^{k+1} = \frac{s_i^k}{\sum_j t_{ij}} \sum_j \frac{t_{ij} p_j}{\sum_l t_{lj} s_l^k} \tag{2.5}$$

where s_i^k represents the k-th image estimate, $T = [t_{ij}]$ represents the transition matrix, $P = [p_j]$ represents the measured data, and $\sum_i t_{ij} s_i^k$ is the projection bin j after forward projection of the k-th image estimate.

This algorithm has the following important properties:

1. The algorithm increases the likelihood that the image estimate will generate the measured data until an absolute maximum during each iteration. However, as the number of iterations increases it also will enhance the noise level of the reconstructed data. A balance between accuracy and variance has to be made.

2. Image elements in each iteration are constrained to remain positive; The algorithm takes into account the Poisson nature of the noise in the projection data. These features of the ML-EM algorithm lead to images which are not noisy as, for example, images reconstructed using FBP.

3. A drawback of ML-EM is that reconstruction is extremely slow, especially when accurate transition matrices are used. In order to render ML-EM fast enough to be used within a clinical setting, the scheme is often accelerated, for example, using block iterative methods such as the Ordered Subsets Expectation Maximization (OS-EM) algorithm of Hudson and Larkin [39]. OS-EM involves grouping projection data into an ordered sequence of subsets. The EM algorithm is then applied to each subset, and the result is used as the starting estimate for processing the next estimate. It has been shown that OS-EM can reach acceleration factors that are close to the number of subsets used [39, 44], while achieving an image quality that is similar to standard ML-EM.

2.3.2 Calculation of the transition matrix

The transition matrix describes the forward projection and re-projection used in iterative SPECT reconstruction. In order to generate an accurate transition matrix one requires an accurate method for calculating photon transport in SPECT.

T_{ij} is a matrix whose elements are the probabilities that a photon originating in the source element s_i is observed in detector projection bin p_j. Given a source distribution s_i, the solution of the photon transport equations through a detailed media (attenuation map, collimator/detector configuration, boundary conditions, ...) yields the projection data (p_j). The reconstruction algorithm solves the inverse problem: given the projection data p_j, find the source distribution s_i.

$$T_{ij}\ s_i\ = p_j \tag{2.6}$$

Since the linear system will typically be overrestricted (more equations than unknowns) and it will often be inconsistent due to instrumental and statistical errors in the projection data (noise), a minimum variance solution is sought using the MLE-EM algorithm.

Despite the fact that physical effects occur both within and across transaxial planes, most iterative methods that have been used to date treat each transaxial plane independently (2D) due to computational considerations. One would expect, however, improved image quality from the more accurate three-dimensional (3D) reconstruction methods —those that model in-plane and cross-plane effects— compared with 2D methods [35]. In Chapter 7 a new application of the 3D physical model for iterative reconstruction in SPECT and the corresponding validation using Monte Carlo techniques is presented.

Modelling photon transport in SPECT (i.e. scatter, attenuation and collimator blurring) for its use in iterative reconstruction is often considered to be challenging, since the calculation method must be accurate for acceptable quality of the image reconstruction and at the same time efficient and fast if it is to be used in clinical practice. In Chapter

6 a new variance reduction technique for SimSET code is used in order to accelerate the simulator.

Attenuation modelling

Attenuation is an elementary effect which has to be modelled. Its mathematical description is simple enough to be described using only two variables, as has been mentioned in section 2.2.1: the photon path length d through the attenuating object from the voxel source s_i to the projection bin p_j, and the type of material and density the photon travels through. Attenuation factors are computed for each pixel at each detector angle as the line attenuation integral between the voxel and the detector pixel along the projection ray of an ideal detector.

The estimate of the density distribution of the patient (μ map or attenuation image) can be precisely represented by a transmission CT map or by a Magnetic Resonance Image (MRI). Acquisition of a transmission CT image has become a common part of the total SPECT acquisition protocol. Other arguments for acquisition of a transmission CT image are improved anatomical localization of activity (e.g. in tumors and infectious foci), registration with other imaging modes and dose calculations. A straightforward way of acquiring a transmission CT (TCT) image would be to carry out a separate scan of the patient on an X-ray CT scanner. However, this is an expensive option and it requires accurate registration of the CT and SPECT images, which is nontrivial in many cases. Great effort has been made in developing ECT systems that simultaneously acquire transmission CT data with the emission data (ECT-TCT scanning). The simultaneous acquisition of these scans immediately solves the registration problem, and makes accurate attenuation correction possible.

PSF modelling

Correction of collimator/detector response may be carried out by modelling the spatially variant resolution and sensitivity functions. These Point Spread Functions (PSF) were defined in section 5.6 and may be included in the transition matrix by determining the contribution of a point source in the voxel source s_i to the projection bin p_j as shown in Figure 2.6.

The PSF model may be obtained by experimental procedures or by Monte Carlo simulation. Experimental studies sometimes involve the use of complex acquisitions (activity calibration, accurate location, etc.) for each collimator/detector configuration. The use of Monte Carlo simulations provide accuracy and flexibility for whatever geometry or photon energy and is a feasible tool in order to design new collimator configurations.

The modelling of PSF for different collimators and energies is presented in this thesis

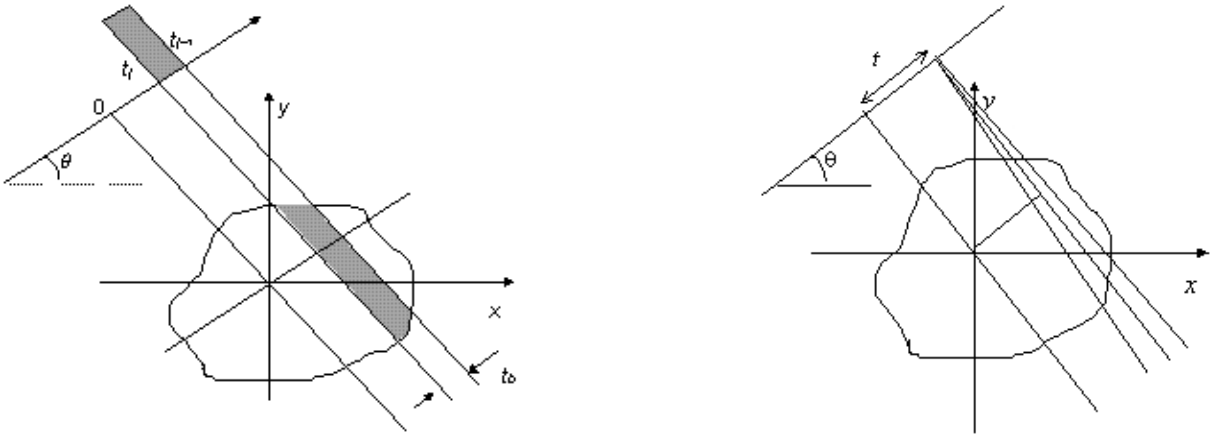

Fig. 2.6: The contribution of a point source in the voxel source s_i to the projection bin p_j without and with PSF.

for low- and high-energy photons in Chapters 4 and 5. Although deterministic modelling of PSF is accurate enough at low-energy ranges, it cannot be used at high-energies. In this case, only Monte Carlo techniques or experimental studies allow correct modelling of PSF functions.

Scatter modelling

There are different methods for scatter correction in reconstruction algorithms [16]. Nowadays, this subject is an intensive field of research in SPECT techniques. The stochastic behaviour of scattering processes make modelling difficult. Some empirical approaches based on experimental data are used, but Monte Carlo techniques appear to be the most reliable way to include this correction.

One type of empirical methods is the Triple Energy Window (TEW) method [60, 40]. This method consists of estimating scatter photons in each projection bin from the detected photons in two additional energy windows W_1^{sc}, W_2^{sc} 4 keV each which are located at either sides of the central window. The counts of the central window (primaries p_j^{prim}) are then corrected by the lateral windows:

$$p_j^{prim} \;=\; p_j - (\tau\; p_j^1 - \varsigma p_j^2) \tag{2.7}$$

However, due to the small size of the windows used in this technique, noise can be substantially increased in the scatter corrected data and accurate results are not always obtained. As an advantage, TEW does not require accurate calibration and it does not need a transmission scan.

A second type of empirical method, which includes the acquisition of data of a transmission scan (TCT-ECT), is the Transmission Dependent Convolution Substraction (TDCS) technique [55, 57]. The scattering effect is estimated deterministically by first convolving the observed photopeak projection data p_j, with a radial mono-exponential scatter function SC in order to provide an initial estimation of scatter p'_j:

$$p'_j = p_j \otimes SC(r) = p_j \otimes \zeta \exp^{-\varsigma r} \tag{2.8}$$

This estimate of the scattering is then corrected with scatter fraction values $k(x, y)$ at each pixel given by the emission projections from the transmission projections as follows:

$$k(x, y) = 1 - \frac{1}{A - Bt(x, y)^{\frac{\beta}{2}}} \tag{2.9}$$

where $t(x, y)$ is the transmission factor at the detector bin position (pixel (x, y)) and A, B and β are geometrically dependent constants. The corrected data p_j^{prim} are then given by the difference of the projection and the estimated scatter fraction pixel by pixel:

$$p_j^{prim}(x, y) = p_j(x, y) - k(x, y)p'_j(x, y) \tag{2.10}$$

However this method assumes an "a-priori" hypothesis about the radial mono-exponential function which implies an empirical but not general approach. Thus, the method which can readily handle media with non-uniform density and large angle scatters is the Monte Carlo (MC) simulation. Different means of scatter correction can be implemented using MC tools:

1. **The Inverse Monte Carlo (IMOC)** method computes the entire transition matrix T_{ij}. MC provides solutions to the photon transport equation for SPECT detection from a unit source activity $s_i = 1$ in each reconstruction source voxel [28, 29]. In the photon transport equation scatter is included as well as attenuation and collimator blurring is accounted for by modelling PSF functions and attenuation factors. The inputs are physical characteristics of the acquisition apparatus such as the energy window setting, the system energy and the spatial resolution, the radius of rotation and the attenuation map of the body and its contours. Due to photon cross-talk between slices, caused by collimator blurring and scattering, full 3D SPECT reconstruction (instead of slice-by- slice (2D) reconstruction) is required for optimal image quality [9]. Unfortunately, hundreds of Giga-bytes, and up to several Tera-bytes of memory are required to store the complete non-sparse transition matrix when the full 3D MC matrix approach is used including all of the corrections. It can take several days to generate the full matrix on a state-of-the-art workstation. In addition, the procedure has to be repeated for each patient.

2. **The Slab Derived Scatter Estimation (SDSE)** first calculates and stores the scatter responses of point sources behind slabs for a range of thicknesses, and then tunes these responses to various object shapes with uniform density [8, 31]. A table occupying only a few megabytes of memory is sufficient to represent this scatter model for full 3D reconstruction [9]. A full 3D reconstruction of a ^{99m}Tc cardiac study based on SDSE can be performed in only a few minutes on a state-of-the-art single processor workstation. A disadvantage of SDSE compared with the matrices generated by IMOC techniques is that it only includes first order Compton scattering and the photoelectric effect, so it neglects multiple-order Compton scattering, coherent scatter and high-energy scatter effects. The Utrecht Monte Carlo System (UMCS) [21] calculates scatter responses using a three-dimensional source emission-distribution (activity image), a mass density distribution (attenuation image) and the geometry and characteristics of the SPECT system. These scatter responses are used in the probability density functions (PDFs) describing the physics of the photon transport, including emission, scatter and detection processes.

3. **The Scatter Monte Carlo Feedback Correction (SMFC)** is a new method developed in this thesis and presented in Chapter 7. SMFC estimates an initial activity distribution (activity image) by reconstructing the experimental projection using P3D-OSEM with a deterministic transition matrix which only includes attenuation and collimator blurring. Afterwards estimated scatter distributions are generated by means of a Monte Carlo simulation as forward projector. The input data for the simulation are the reconstructed activity distribution (activity image), the attenuation map (attenuation image) and the constant geometry and characteristics of the SPECT system. The Monte Carlo simulation of forward projection includes all image degrading effects, that is, the attenuation modelling, collimator blurring, scattering and noise equivalent counting on the projections. The transition matrix used in the iterative algorithm should only include attenuation and collimator blurring modelling because the scattering effect is corrected on the projections. The more accurately the Monte Carlo simulation is performed, the better the agreement between the estimated activity images and the real activity distribution.

A drawback of MC simulation is that it can take several days to calculate accurate, almost noise-free data. This was the reason to focus the research described in this thesis on the development of acceleration methods for MC simulation in SPECT imaging. Furthermore, MC techniques need new hardware implementation infrastructures such as PC clusters or new, powerful workstations in order to make clinical image reconstruction feasible.

2.3.3 Analysis of reconstruction algorithms: Phantom studies

As shown in section 2.3.2, the transition matrix includes several correction factors for different degrading effects on the projection acquisition. Moreover, the choice of the number of iterations is important when using iterative algorithms. Thus, the performance of an iterative reconstruction algorithm has to be tested by using "gold standard" references.

The gold standard must be a phantom with an a-priori known activity and attenuation map. Phantoms "emit" photons which are detected. The projected data set is reconstructed by using the algorithm under study. Finally, both reconstruction and phantom objects are compared using quantification procedures.

There are two kinds of phantoms: experimental and **virtual phantoms**. The former are human organs or tissues made with equivalent attenuating materials and shapes. However, these phantoms are highly complex, expensive and they are not flexible enough in order to change object parameters (geometric dimensions, activity distributions, statistical noise on the projections, etc.). Virtual phantoms are described by means of an "electronic" attenuation and activity map. These maps include a discrete voxelization of the organs and tissues obtained by CT or MRI techniques. Virtual phantoms "emit" photons by simulating them using Monte Carlo techniques (See Chapter 3). The Monte Carlo simulation reproduces all the physical interactions involved in photon flight from the object through the detector: the SPECT measure.

3. MONTE CARLO IN NUCLEAR MEDICINE

"Definition of Radiograph: a photographic image produced by the transmission of x-rays"
Webster's Dictionary

3.1 Monte Carlo in Nuclear Medicine

In Chapter 2 a summary of image degrading corrections was presented. Most of these corrections involve the use of Monte Carlo techniques:

1. The modelling of the PSF for the collimator/detector response correction.

2. The scattering correction on the projection data set.

3. The use of virtual phantoms simulators in order to test the accuracy of the reconstruction algorithms.

The Monte Carlo technique is a mathematical solution for a wide range of applications with different conditions and objectives to be fulfilled. For instance, in Nuclear Medicine

the modelling of the PSF will include a very accurate physical description of particle interactions in the collimator/detector system (both photons and x-rays) and a complex geometry. On the other hand, the virtual phantom simulator will perform a simplified physical description of particle interactions in the human body in order to speed up results. Therefore, we will choose different Monte Carlo codes depending on each application.

In this Section we present the different available Monte Carlo codes and their main features. We present the reasons for using PENELOPE as the Monte Carlo simulator for PSF modelling. The choice for the virtual phantom simulator is accompanied with the correspondent analysis of its results. Some modifications were implemented in this MC, the SimSET code. In order to understand the changes implemented in the original SimSET code, a revision of Monte Carlo basis is presented in Appendix A.

3.1.1 Definition of Monte Carlo

"The Monte Carlo method is a numerical solution to a problem that models objects interacting with other objects or their environment based upon simple object-object or object-environment relationships[1]. It represents an attempt to model nature through direct simulation of the essential dynamics of the system in question. In this sense the Monte Carlo method is essentially simple in its approach. It searches for a solution of a macroscopic system through simulation of its microscopic interactions" [11].

A solution is determined by random sampling of the relationships, or the microscopic interactions, until the result converges. Thus, the mechanics of executing a solution involves repetitive action or calculation. To the extent that many microscopic interactions can be modelled mathematically, the repetitive solution can be executed on a computer. However, while the Monte Carlo method predates the computer, in most cases computers make the determination of a solution much faster.

The products of both basic and applied science are dependent on the trinity of measurement, theory and Monte Carlo simulation. Monte Carlo is often seen as a "competitor" to other methods of macroscopic calculation, which we will call deterministic and/or analytic methods. The practice of science should decide whether it is sufficiently accurate to go through the deterministic approach or use the Monte Carlo method. Monte Carlo techniques become advantageous as the complexity of a problem increases. In Nuclear Medicine the deterministic approach was initially used to model the attenuation and PSF corrections. However, the scattering model has not been modelled accurately enough by deterministic methods. Thus, the Monte Carlo method presents a case-by-case approach using the particle interaction theory to provide guidance to the process of discovery.

[1] This presupposes that all uses of the Monte Carlo method are for the purposes of understanding physical phenomena. There are other uses of the Monte Carlo method for purely mathematical reasons, such as the determination of multi-dimensional integrals.

There are many examples of the use of the Monte Carlo method that can be drawn from social science, traffic flow, population growth, finance markets, genetics, quantum chemistry, radiation sciences, radiotherapy, and radiation dosimetry. Our focus on Monte Carlo methods will concentrate on the simulation of particles being transported in human bodies and tissues. As the scope of our work is restricted to SPECT studies in Nuclear Medicine most of our simulations include only photon transport. Electron transport is only needed when working with high-energy rays above 300 keV (see Chapter 5).

3.1.2 Monte Carlo history

The usual first reference to the method of Monte Carlo is that of Comte de Buffon [20] who proposed a Monte Carlo-like method to evaluate the probability of tossing a needle onto a ruled sheet. This reference goes back to 1777, well before the existence of automatic calculating machines. Later, Laplace [50] suggested that this procedure could be employed to determine the value of π, albeit slowly. Several other historical uses of the Monte Carlo method predating computers are cited by Kalos and Whitlock [43].

Monte Carlo (MC) simulation using computers was first used during the World War II Manhattan project to designate a class of numerical methods based on the use of random numbers. Von Neumann and Ulam named it Monte Carlo simulation because of the similarity between statistical simulation and games of chance. Of course, one of the most well-known center for gambling is the Monte Carlo casino [87].

3.1.3 Monte Carlo basis

Fundamental to understanding the operation of a Monte Carlo process and interpreting the results of Monte Carlo calculations, is some understanding of:

1. Elementary probability theory

2. "Pseudo" random number generators

3. Statistical theory and error estimation

Elementary probability theory

Monte Carlo (MC) simulation can be described as a statistical simulation method based on random sampling of probability density functions (PDF). A PDF is a measure[2] of

[2] "Tallying" is Monte Carlo jargon for "measuring" something, as one would do in an experiment. There are many similarities between the handling of measured and tallied data, except that the tallies in Monte Carlo simulation can be unambiguous, not obfuscated by extraneous physical detail. Monte Carlo

the likelihood of observing x. Such a $PDF(x)$ can, for example, describe the photon path length x up to the next interaction with matter. Sampling a $PDF(x)$, normalized by integration over its definition range $[a, b]$, can be performed by constructing a cumulated probability density function ($CPDF(x)$):

$$CPDF(x) = \int_0^x PDF(\zeta)d\zeta \tag{3.1}$$

A random variable ξ can be sampled by substituting a random number in the range of $[0, 1)$ for $CPDF(x)$ and solve the equation for x. If $PDF(x)$ is analytically integrable,x can be sampled in a straightforward manner. Often the $PDF(x)$ is too complex to allow analytic integration, as in the case of the Klein-Nishina formula which describes the probability of Compton scattering over angle θ. In such cases the $CPDF(x)$ can be described numerically.

"Pseudo" random number generators

The "pseudo" random number generator (RNG) is the "soul" of a Monte Carlo simulation. It is what generates the pseudo-random nature of Monte Carlo simulations thereby imitating the true stochastic or random nature of particle interactions. Consequently, much mathematical study has been devoted to RNG's [48].

Linear congruential random number generators (LCRNG) are used for most computer architectures which support 32-bit 2's-complement integer arithmetic[3]. The following equation describes a linear congruential random number generator (LCRNG) suitable for machines that employ 2's-complement integer arithmetic:

$$X_{n+1} = mod(aX_n + c, 2^{32}) \tag{3.2}$$

This LCRNG generates a 32-bit string of random bits X_{n+1} from another representation one step earlier in the cycle, X_n. In this equation a is a "magic" multiplier and c is an odd number. Although there are guidelines to determine a good multiplier, optimum

analysis also allows a deeper study into the statistical nature of the tally, something that experiments are often not able to fulfil.

[3] In 32-bit 2's-complement integer arithmetic architecture:
$00000000000000000000000000000000 = 0$
$00000000000000000000000000000001 = 1$
$00000000000000000000000000000010 = 2...$
$01111111111111111111111111111111 = 2^{31} - 1 = 2147483647$
$10000000000000000000000000000000 = -2^{31} = -2147483648$
$10000000000000000000000000000001 = -2^{31} + 1 = -2147483647$
$10000000000000000000000000000010 = -2^{31} + 2 = -2147483646...$
$11111111111111111111111111111111 = -1$

ones are determined experimentally. Particularly good examples are a = 663608941 and a = 69069. The latter has been suggested by Donald Knuth [48] as the "best" 32-bit multiplier. When c is an odd number, the cycle length of the of the LCRNG is 2^{32} (about 4 billion, in effect, creating every integer in the realm of possibility and an artifactually uniform random number when converted to floating point numbers. When c is set to zero, the LCRNG becomes what is known as a multiplicative congruential random number generator (MCRNG) with a cycle of 2^{30} (about 1 billion) but with faster execution, saving a fetch and an integer addition.

Statistical theory and error estimation

Statistical Mathematics Theory [66],[71] indicates that if:

1. The number of emitted photons is large $Nc > 10$ —usually Nuclear Medicine isotopes emit million of photons per second—.
2. The detection probability of a point source in air is lower than $\mu(A) < 0.05$ — detection probabilities on a single head SPECT camera are typically $\mu(A) < 10^{-4}$—.

the photon distribution in the detector bin A is a Poisson Distribution. A special case of a Poisson Distribution appears when the number of detected counts $\lambda > K$ is large enough to transform the Poisson distribution into a Gaussian distribution with mean and variance equal to λ. Some authors [71] situate this minimum threshold value at $K = 5$ (See Appendix A).

In fact, **most of the applications and theories used in the field of Nuclear Medicine are based on considering Gaussian distributions** at each detector bin. Such an assumption may be taken when the following conditions are accomplished:

1. The detection of an event is independent of the others
2. There is a huge number of emitted photons (decays) from the source radioisotope
3. The probability of detection is very small
4. The product of the number of emitted photons N_c and the probability of detection ($\mu(A)$) —which is the number of counts at every detector bin N_A— is higher than the threshold, i.e. $\lambda > K$

If these conditions are fulfilled, statistical techniques could be used in the fields of Nuclear Medicine:

1. Monte Carlo simulation produces Gaussian distributions of the projection data set. If the number of counts at each voxel ensures a Gaussian distribution, Monte Carlo simulations of the virtual phantom projections may be obtained directly with the correct noise estimate.

2. The models for PSFs are obtained with experimental or simulated projection data of a point source. These models are based upon high counting statistics at each bin.

3. Statistical Parametrical Mapping —SPM— analysis of reconstructed images based upon tStudent tests

Thus, the basic tool to be used in this thesis has been introduced: Monte Carlo simulation techniques.

3.2 Monte Carlo codes for particle transport

Many MC programmes are in use in the field of Nuclear Medicine or nuclear particle transport as is shown in Table 3.1. These include general purpose codes such as EGS4 [58], PENELOPE [74] or MCNP [13] among others. Some of them can simulate not only photon transport in detail, but also electron or neutron transport. Since these programmes are often designed to allow the study of a large range of photon transport problems, they are often complex to use. The generality of the programs may be a direct cause of computational inefficiency. Furthermore, existing codes such as MCNP or PENELOPE often do not allow other Variance Reduction Techniques (VRT) to be included or acceleration methods designed for a specific SPECT imaging situation, although they describe the underlying physics more accurately. This is the reason for the development of specific Nuclear Medicine codes such as SimSET [37], SIMIND [52] or UMCS [21] among others.

The first task of this work was to look for the most significant Monte Carlo codes. Afterwards, a comparison between those which are more reliable for the different applications was carried out. Table 3.1 shows the comparison of the most relevant characteristics of each code.

3.2.1 PENELOPE code

PSF modelling will be performed with a very accurate modelling of the underlying physics of particle interactions with matter, especially at high energies. Furthermore, the collimator/detector configuration requires a detailed, complex geometry description. These features may be supplied by a general-purpose code.

The PENELOPE code was chosen due to its great accuracy, wide range of energies and fast simulation transport including secondary particles (x-rays, electrons, etc.)

Codes	SPECT	PET	Coll.	Elec.	Language	Origin
EGS	no	no	no	yes	Mortran	
ITS	no	no	no	yes	Fortran	Los Alamos
PENELOPE	no	no	user	yes	Fortran	Barcelona
MCNP	no	no	user	yes	Fortran	Los Alamos
SimSET	yes	yes	yes	no	C++	Seattle
MCMATV	yes	no	yes	no	Fortran	Chapel Hill
SIMIND	yes	no	yes	no	Fortran90	Lund
SIMSPECT	yes	no	yes	yes	C	MIT
PETSIM	no	yes	yes	no	Fortran	Montreal

Tab. 3.1: Monte Carlo codes used in nuclear imaging. The first four are general purpose codes, whereas the latter five are specific Nuclear Medicine codes. Each column specifies its availability for SPECT or PET simulation, collimator/detector PSF modelling, electron simulation and the language code and place where it was developed.

through the collimator/detector system. The interaction models allow the simulation of photon/electron transport in the energy range from 100 eV to 1 GeV [73]. A detailed description of its components and features can also be found in previous publications [76, 74, 4].

Moreover, PENELOPE includes a set of geometry routines, named PENGEOM, capable of handling any object formed by homogeneous bodies limited by quadric surfaces (such as planes, cylinders, spheres, etc). In this code system, the user is responsible for writing a simple steering main program, from where some of the PENELOPE and PENGEOM subroutines are called to perform the tracking of the particles simulated in whatever geometry. In our case, the complexity associated with the description of the fan beam collimator geometry prevented us from using PENGEOM in the standard way. Instead, we introduced a new solution presented 4 and 5 for low- and high-energy photons respectively.

3.2.2 SimSET code

The simulation of virtual phantoms or the correction of the scattering in the projections needs a fast Monte Carlo code without an excessively detailed underlying physical description. Moreover, the SPECT geometry consists of a complex tomograph cylinder with a user-defined number of detector head positions at different angles, radius-of-rotation (ROR), field of view (FOV), energy window, pixel binning, etc. The MC code will include all these detailed specifications of the SPECT technique.

The **S**imulation **S**ystem for **E**mission **T**omographs (**SimSET**) [36] was the software

application chosen to overcome these problems and to provide a fast photon transport simulation in both SPECT and PET. Other reasons for this choice were the availability and the modular structure of the source code, the well-known language of the code (C++) and the reliability of the program on different computer platforms (Linux, Unix, Windows, etc.). Furthermore, the possibility to both contact and collaborate with the group which developed the program was taken into account.

SimSET was developed at the Imaging Research Laboratory at the University of Washington (Seattle, USA) for public distribution to Nuclear Medicine research centers. The purpose of the SimSET package is to simulate the transport of photons generated from a volumetric distribution of an isotope through an independent heterogeneous attenuating medium (human body, experimental phantoms, camera headers, etc.). In the final step the photons are collimated, detected and binned for obtaining the corresponding projections (sinograms). The experienced user may modify some of the modules incorporating some improvements in the code. In this thesis the Collimator Module which performs the collimation process was modified because in the original SimSET version only the geometrical component of the PSF was modelled (See Chapter 6). A new probability density function which includes scatter within the collimator and septal penetration was further developed using Monte Carlo techniques.

As input for the calculations, SimSET requires a digital representation of the activity distribution (activity or source map) and mass density distribution (attenuation or TCT map) of the patient. The Activity Object defines the spatial distribution of isotope concentration from which photons will be generated. The Attenuation Object defines the spatial distribution of attenuation material through which photons will travel. Although these two items provide different information for the simulation, they share a common geometric/parametric definition. Both items are needed to describe the Object as is shown in Figure B.2.

SimSET can use the most common virtual phantom files such as the striatal, Zubal or Hoffman brain phantom. Appendix B provides a detailed introduction to the package along with a road map to the documentation and files [38] required to use the SimSET package.

3.3 Adaptation of SimSET as a virtual phantom simulator

A lot of trouble was found in interpreting the SimSET results. After the initial stage in Seattle, the SimSET developers presented SimSET as an engineering software tool for designing hardware parts of the gamma camera. They focused on obtaining scattering rations, energy responses, efficiencies, etc. for different isotopes and camera designs using both SPECT and PET techniques. Their research did not produce the improvement or assessment of the reconstruction algorithms.

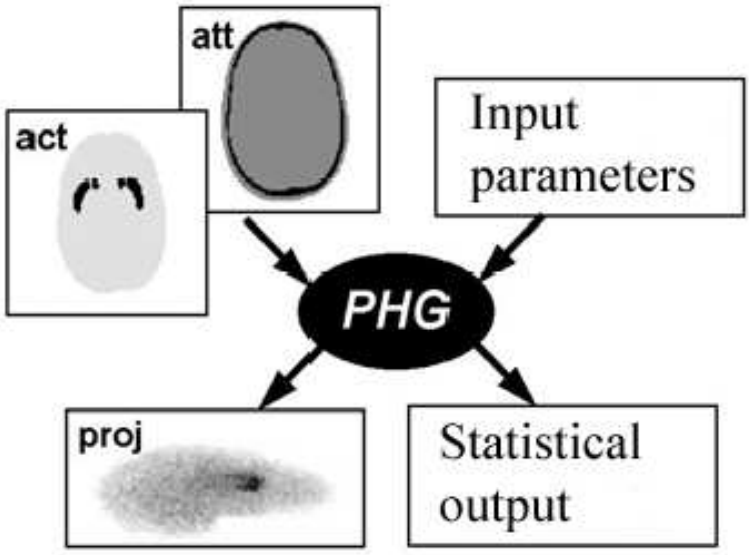

Fig. 3.1: Photon History Generator diagram. The rounded rectangles at the top represent the various parameters that are required as input to the PHG, while the rectangles at the bottom represent the PHG outputs.

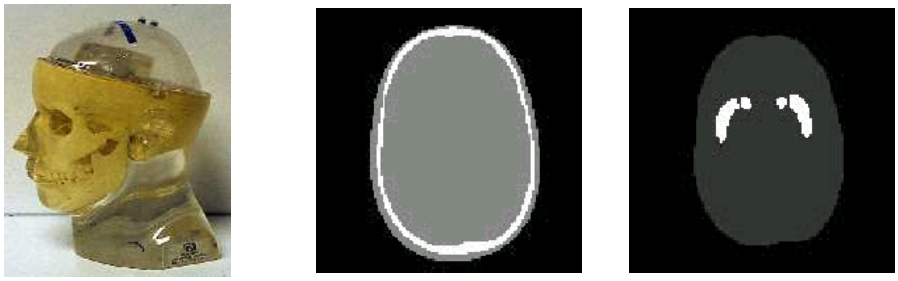

(A) (B) (C)

Fig. 3.2: Striatal phantom for neuroreceptor SPECT studies. The experimental phantom is shown in -A- and is used for validation trials. The virtual phantom with its corresponding attenuation -B- and activity -C- maps for a certain slice are also shown.

SimSET was thus not initially adapted as a virtual phantom simulator. The Monte Carlo virtual phantom simulator must control not only the mean but also the variance —the statistical noise— of projections. The level of counts of the study is a key point in the analysis of the results. The original SimSET code could simulate projections of most virtual phantoms but it did not reproduce the level of counts and the statistical noise of a "real" SPECT acquisition. Therefore, an analysis in detail of the SimSET code and the resulting statistics was needed.

This analysis is presented by comparing the design basis of SimSET and an "Analogue Monte Carlo" simulation. For a better understanding, we only include relevant results but in Appendix A the basis of each simulation is developed in more detail.

3.3.1 Interpretation of the SimSET mean

The Analogue Monte Carlo method

Monte Carlo methods are designed to find the parameters of a distribution that is governed by stochastic variables. It is important to note that the process of detection is stochastic because of its quantum nature. A parameter estimated by Monte Carlo methods is an **estimate**. Monte Carlo methods find a value for the **estimate** by working with a **sample** set of random variables in a certain **sample size**.

In a Nuclear Medicine Monte Carlo application, $\mathbf{\Omega}$ is the set of available bin detectors locations of the gamma camera, the probability distribution μ is governed by the physics of photon transport through the media (object and collimator/detector system), and N_c is the total number of emitted photons (decays of the radioisotope) in the body of the patient. Therefore, the Analogue Monte Carlo method applied to Nuclear Medicine estimates the parameters of the distribution (basically mean and variance) of counts, N_A, at bin A for a certain bin detector.

However, this underlying distribution is unknown, thus we have to perform a simulation. We execute a loop i = 1; 2; 3...; N_h over N_h Monte Carlo histories and accumulate the tally of score of χ_A. The final tally is an estimate of the mean of detected events in A:

$$E(\bar{\chi_A}) \;=\; \frac{\sum_{h=0}^{h=N_h} \chi_A(h)}{N_h} \tag{3.3}$$

The question which now arises is: How good is our estimate $E(\bar{\chi_A})$ for $\bar{\chi_A}$ is? And, which is the error of this estimate? Fortunately, if the probability density function is a properly defined with the corresponding variance and N_h is large enough, the **Central Limit Theorem** indicates that the variance of the tally is $1/N_h$ times that of a single tally. And what is more, the different estimated values themselves will tend to be normally

distributed (centered at $\bar{x}$ and with a Gaussian width $\frac{\sigma}{\sqrt{N_h}}$) even if the random variable itself is not normally distributed (See Appendix A).

Note that this makes no assumptions about the shape of the probability distribution μ, but that its second moment exists. Irrespective of the shape of μ, the estimate of its mean will be normally (Gaussian) distributed and the width of the distribution will narrow with the increase of the sampling size. This is truly one of the most remarkable results in mathematics! This fact is really important because it allows us to calculate the result as follows:

1. Calculate the mean value of $\chi_A(h)$:

$$E(\bar{\chi_A}) \;=\; \frac{\sum_{h=0}^{h=N_h} \chi_A(h)}{N_h} \tag{3.4}$$

2. Estimate the variance of the $E(\bar{\chi_A})$ using the Central Limit Theorem:

$$\mathrm{Var}(\bar{\chi_A}) \;=\; \frac{1}{N_h}\{E(\chi_A) - (E(\chi_A))^2\} \;=\; \frac{1}{N_h}\mathrm{Var}(\chi_A) \tag{3.5}$$

3. Report the final result as:

$$\chi_A \;=\; E(\bar{\chi_A}) \pm \sqrt{\mathrm{Var}(\bar{\chi_A})} \tag{3.6}$$

Thus, the deviation in our estimate is related to the deviation of the parent distribution, and it decreases with the square root of the number of histories, N_h. This is a fundamental result of classical Monte Carlo methods. Note that the first term of the equation is the variance reduction due to the Central Limit Theory, and the second term is the so-called intrinsic variance which is a random value depending on the simulation problem (geometry configuration, photon tracking, etc.).

Nevertheless the biggest problem with Monte Carlo techniques is the extremely slow convergence of the estimate. The estimate error is inversely proportional to the square of the size of the observation set (N_h). In other words, the algorithm has a convergence of $O(\frac{1}{\sqrt{N_h}})$. Thus, the quadrupled number of histories to sort only halves the error (i.e. at much more CPU time the variance can be reduced). Much of the research in Monte Carlo methods has been aimed at increasing the convergence of the estimator by decreasing its intrinsic variance $\mathrm{Var}(\chi_A)$ and getting better results from fewer samples. The intrinsic variance is constant (randomly constant) but could be changed on the basis of Monte Carlo knowledge : **Variance Reduction Techniques (VRT)** (See Appendix A).

SimSET Monte Carlo

The sampling of each history is defined in SimSET as in the Analogue Monte Carlo method, but with a difference in the initial weight. This will change the statistical results of SimSET in comparison with a standard Monte Carlo code. Whereas in the latter all the results are given **per particle emitted**, in the former the results are **absolute counts**. Then in SimSET a variable proportional of the activity is defined and is the number of decays at each voxel Nc_k and the total decayed particles in the object, Nc:

$$Nc \;=\; \sum_{k=1}^{k=K} A_k \Delta V_k \Delta t \;=\; \sum_{k=1}^{k=K} Nc_k \tag{3.7}$$

where:

1. Δt is the scan time for the SPECT acquisition[4]

2. All the voxels defined in the input of PHG have a certain volume represented by ΔV_k

3. Finally Nc_k is the number of decays at each voxel, obtained in $\frac{\mu Ci}{cm^3} cm^3 s^5$

The new sorting n_k then decays at each voxel K of the object volume and is defined according to this new decay map. The decays are sorted voxel by voxel in a sequential order as described in [37]:

$$n_k \;=\; N_h \, \frac{Nc_k}{Nc} \tag{3.8}$$

The initial weight differs from that of Analogue Monte Carlo simulation. In SimSET, the result —the number of counts received at a certain detector A— depends on the particular conditions of the scan (length of scan, activity map and object volume) whereas standard Monte Carlo simulation delivers a general result —the detected events per unit particle— which can be easily related to the conditions of the scan. So the initial weight in SimSET is set to:

[4] In the original SimSET code this variable was called **length of scan** and was defined constant for all the simulations. However we introduced changes to the original code in order to transform **length of scan into a defined user variable** in order to control the mean level of total counts in the projection data set. This is done in SimSET code at routine SubObj.c in function SubObjCalcTimeBinDecay (calculus on n_k for each voxel) and the weight is set on SubObjDecayWeightSlice

[5] The activity in each voxel is supposed constant during the length of the scan. This assumption may be taken for isotopes such as ^{99m}Tc or ^{123}I whose half-life periods are larger than the length of the scan.

$$w_0 \;=\; \frac{Nc}{N_h} \tag{3.9}$$

Once the N_h histories have been sorted with the density probability function p_k and the tracking has set a weight $w(h)$ for each, the magnitude estimated by SimSET is **directly** the number of events received at detector A, i.e. the mean value of the event $w_0(h)w(h)\chi_A(h)$:

$$E_{\text{SimSET}}(\bar{\chi_A}) \;=\; \sum_{h=1}^{h=N_h} \chi_A(h)w_0(h)w(h) \;=\; \frac{\sum_{h=1}^{h=N_h} \chi_A(h)N_c\; w(h)}{N_h} \tag{3.10}$$

From equations (3.10) and (A.26) it is clear that the relation between SimSET's mean estimator and the standard Monte Carlo's estimator is:

$$E(\bar{\chi_A}) \;=\; \frac{E_{SimSET}(\bar{\chi_A})}{Nc} \tag{3.11}$$

Similarly the variance estimator relation between the SimSET and the Analogue Monte Carlo simulation can be studied, giving:

$$\text{Var}_{MC}(\bar{\chi_A}) \;=\; \frac{\text{Var}_{SimSET}(\bar{\chi_A})}{Nc^2} \tag{3.12}$$

If we ask the question "how many particles N_A have reached the bin detector A after Nc particles have decayed from the source "? we obtain different answers depending on the type of simulation. From the Standard Monte Carlo point of view:

$$N_A \;=\; Nc\; E(\bar{\chi_A}) \tag{3.13}$$

And applying the relation between both:

$$N_A \;=\; Nc\; E(\bar{\chi_A}) \;=\; Nc\; \frac{E_{SimSET}(\bar{\chi_A})}{Nc} \;=\; E_{SimSET}(\bar{\chi_A}) \tag{3.14}$$

So the mean estimator given by SimSET is directly the number of "real counts" in detector bin A. Nevertheless, at this point there were some important questions which had not been described in the SimSET manuals:

1. Which is the detected counts distribution at each bin detector given by SimSET?

The bin detector distribution coming out from a Monte Carlo simulation follows a Gaussian distribution if the number of counts at each bin is greater than $\lambda = 5$ because of the Central Limit Theorem and the characteristics of the detection probability density function —(See Appendix A)—.

2. How could a simulated sinogram be equivalent to an experimental acquisition of a SPECT study with the same mean and variance?

3.3.2 Interpretation of the SimSET variance

There are two possible answers to the last question:

1. Simulating a study with a huge number of histories N_h such that:

$$\lim_{N_h \to \infty} \mathrm{Var}(\bar{\chi_A}) \;=\; \lim_{N_h \to \infty} \frac{1}{N_h} \mathrm{Var}(\chi_A) \;=\; 0 \tag{3.15}$$

Then the mean would be estimated without error [25]. In order to reproduce the same variance as the experimental acquisition, the Poisson distribution would be sorted at each detector bin based upon the known exact mean. The problem of this solution is the burdensome computer effort in terms of CPU time in order to reach the desired number of histories.

2. Developing a new stopping criteria for SimSET simulations. There is a point in each simulation when the variance and the mean estimator are equal to the real ones.

A new Stopping Criteria for SimSET

In this thesis a new stopping criteria for SimSET simulations in order to get "real" variance on the distribution of counts fixed by the user is presented. The different conditions which SimSET simulation has to fulfil in order to obtain a certain number of particles N_A at bin detector A after Nc particles have decayed from the source are:

1. The user should fix the correct length of scan time Δt_1 in the simulation at a certain value in order to obtain the desired number of detected events[6] N_{A_1}. The mean estimator is linear with Δt, so it is possible to perform an initial simulation ($\emptyset$) in order to obtain the slope of the linear regression:

$$\Delta t_1 \;=\; \Delta t_\emptyset \, \frac{N_{A_1}}{\sum_{h=1}^{h=N_h} w_{0_\emptyset}(h) w_\emptyset(h)} \tag{3.16}$$

[6] In Nuclear Medicine studies the quality of the image is associated with its low variance, that is the number of counts N_{A_1}.

2. With the new Δt_1 a new simulation (1) may be performed and N_{A_1} is reached as the estimated mean. The variance $\mathrm{Var}_{SimSET}(\bar{N_{A_1}})$ obtained in the simulation could be used in order to get the linear regression factor between the variance of the simulation and N_h. Once the simulation is performed, the correct number of histories N_{h_2} may be adjusted because the final variance of the simulation is known, and it is equal to the desired number of counts N_{A_1}.

$$N_{h_2} \;=\; N_{h_1}\,\frac{N_{A_1}}{\sum_{h=1}^{h=N_h} w_{0_1}(h)^2 w_1(h)^2} \tag{3.17}$$

3. The result of simulation (2) gives a counter distribution with equal mean and variance, so a "real" nuclear medicine study will be obtained.

$$N_{A_1} \;=\; \sum_{h=1}^{h=N_h} w_{0_2}(h) w_2(h) \tag{3.18}$$

$$\mathrm{Var}_{SimSET}(\bar{N_A}) \;=\; N_{A_1} \;=\; \sum_{h=1}^{h=N_h} w_2(h)^2 \tag{3.19}$$

The only condition is to have a sufficiently high-count of the distribution $N_i > 5$ in all the detector bins i for the distributions to be Gaussian —See Appendix A—.

Demonstration 1 for SimSET stopping criteria

If both images (real and simulated) have to be the same at each bin we need to obtain the same mean and if both images have the same noise, they will present the same variance. The variance $\mathrm{Var}(N_A)$ —of a Poisson distribution— then has to be equal to the mean:

$$\mathrm{Var}(N_A) \;\simeq\; N_A \;=\; Nc^2\,\mathrm{Var}_{MC}(\bar{\chi_A}) \;=\; \mathrm{Var}_{SimSET}(\bar{\chi_A}) \tag{3.20}$$

Demonstration 2 for SimSET stopping criteria

Another way to demonstrate that the estimators of the mean and the variance have to reach the same value in SimSET simulations is by comparison of the signal-to-noise ratio **SNR** parameter between both images. The SNR parameter is defined for any random variable or distribution X as:

$$SNR(X) \;=\; \frac{\sigma(X)}{\bar{X}} \tag{3.21}$$

For a real image with a stochastic distribution of N_A counts in a detector bin A, with the same assumptions as were made in the last section about the Poisson distribution of real noise, the SNR parameter is set to:

$$SNR_{real}(N_A) \;=\; \frac{\sqrt{N_A}}{N_A} \;=\; \frac{1}{\sqrt{N_A}} \tag{3.22}$$

The same parameter can be calculated for a simulated SimSET image:

$$SNR_{SimSET}(N_A) \;=\; \frac{\sqrt{\sum_{h=1}^{h=N_h} w_0^2 w(h)^2}}{\sum_{h=1}^{h=N_h} w_0(h)w(h)} \tag{3.23}$$

Moreover, the mean equals the number of counts in bin A:

$$N_A \;=\; \sum_{h=1}^{h=N_h} w_0(h)w(h) \tag{3.24}$$

Substituting the last equation in the SNR for a simulated image (3.23), it yields:

$$SNR_{SimSET}(N_A) \;=\; \frac{\sqrt{\sum_{h=1}^{h=N_h} w_0^2 w(h)^2}}{N_A} \tag{3.25}$$

Comparing both parameters and setting them equal, we obtain:

$$SNR_{SimSET} \;=\; SNR_{real} \tag{3.26}$$

$$\frac{\sqrt{\sum_{h=1}^{h=N_h} w_0^2 w(h)^2}}{N_A} \;=\; \frac{1}{\sqrt{N_A}} \tag{3.27}$$

$$\sqrt{\sum_{h=1}^{h=N_h} w_0^2 w(h)^2} \;=\; \sqrt{N_A} \tag{3.28}$$

It is important to note that there is a unique solution for the last equation as the simulation variance is a continous, monotonic decreasing function of N_h:

$$\sum_{h=1}^{h=N_h} w_0^2 w(h)^2 \;=\; N_A \tag{3.29}$$

$$\mathrm{Var}_{SimSET}(\bar{\chi_A}) \;=\; N_A \tag{3.30}$$

3.4 Validation of the modified SimSET code

In order to compare two different outputs, (i.e. an experimental image projection and a simulated image) it is common to use the $t-Student$ test. This test assumes two-normal distributions at each bin detector and it compares both testing the **null hypothesis**. The compared results between experimental and simulated projections of a geometric phantom were presented by Cot et al. [17].

3.4.1 Null hypothesis

The null hypothesis asserts the coincidence of two samples. The trial is based on the "difference distribution" and the analysis of its statistics. This new distribution is supposed to be zero or null. The $t-Student$ test is a tool used to compare images in Nuclear Medicine. The "difference distribution" is then referred to as the difference bin to bin (x_A) between images:

$$x_A - y_A \;=\; 0 \tag{3.31}$$

Once the "difference distribution" is defined, some samples of this distribution (e.g. the available images) are compared with the null image, i.e. the image with $\mu = 0$ and $\sigma = 0$. This comparison is calculated based on the statistical parameters of the different images:

$$t_S \;=\; \frac{(\bar{x_A} - \bar{y_A}) - 0}{\mathrm{Var}(x_A + y_A)} \;=\; \frac{(\bar{x_A} - \bar{y_A}) - 0}{\mathrm{Var}(x_A) + \mathrm{Var}(y_A)} \tag{3.32}$$

This test assumes normal behaviour of the two images to be compared. This condition is ensured by selecting those bins with a statistical size superior to a selected threshold ($\lambda \geq 5$, see Appendix A). It is clear that the lower the threshold, the bigger the sample becomes, and so the results are based on a large number of statistics. The results of the $t-Student$ test indicate the error when the null hypothesis is rejected. If the "difference distribution" does not fulfil a normal distribution (based on its confidence interval below $t = 1, 2, 3 \times \sigma$) then the probability of error is precisely this confidence interval.

In Nuclear Medicine applications the reference images are the experimental projections, whereas the image to be tested is the simulated image. Both are supposed to belong to the same distribution and the null hypothesis is applied. For those "difference

distributions" whose confidence intervals are below 2 σ are close to 95%, there is only a 5% error when rejecting the null hypothesis.

3.4.2 Material and Methods

The aim of this work was to validate the SimSET capacity to generate SPECT studies. In order to validate the modified SimSET simulator, the experimental projections acquired in the Nuclear Medicine Department of the Hospital Clínic were compared with those projections obtained by Monte Carlo simulation in the same conditions. It was decided to use a geometrical phantom to be imaged. Both image outputs, the experimental and the simulated ones should be compared using the t-Student test.

Experimental acquisitions

The real studies were obtained with a cylindrical lucite phantom built at the Laboratory of Biophysics and Bioengineering. It contained six 10-cm-high cylinders of 5, 4, 3, 2, 1.5 and 1 cm in diameter. They were placed describing a hexagonal shape —See Figure 7.1—.

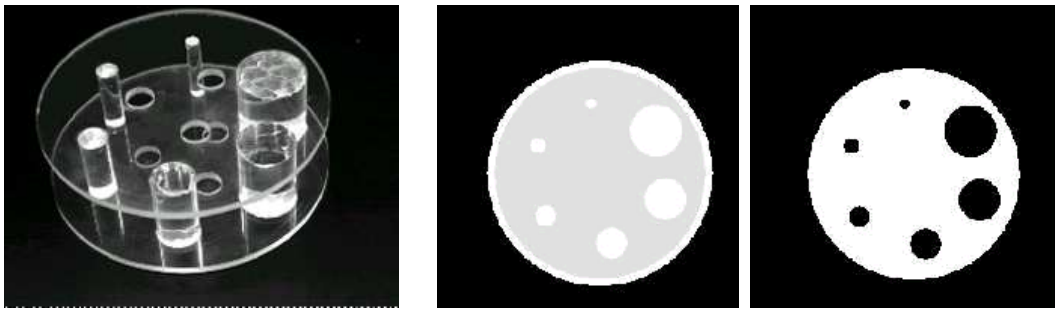

(A) (B) (C)

Fig. 3.3: Experimental phantom geometry -A- with its correspondent attenuation -B- and activity -C- maps

The cylindrical phantom was inserted in a 20-cm-diameter cylindrical tank filled with water and ^{99m}Tc. The projections were obtained in an ELSCINT SP4 gamma camera with a parallel high resolution collimator. The radius of rotation was 17 cm and the detector heads covered 360º in 60 projections of 64×64 bins. The size of each bin detector (or pixel) was $0.4717 \times 0.4717\ cm^2$. The statistical level of the study was 1.85×10^6 detected counts.

SimSET simulations

The Monte Carlo simulation was performed using the attenuation and activity maps of the object cylinder shown in Figure 7.1. The rectangular grid used was binned in 256×256 bins of 0.1179 $\frac{cm}{bin}$ and 18 slices 0.4717 cm in height. The activity value was made homogeneous for the active volume at $10^{-4}\frac{\mu Ci}{cm^3}$ of ^{99m}Tc photons at 140 keV.

The length of scan user-variable was set to 4.872 seconds in order to get the same level of counts than in the experimental acquisition. With this length of scan and activity map, the total number of decays from the object was 2.37×10^{10} during the whole study. The target cylinder was fitted with a collimator/detector system with a radius of rotation of 17 cm and a transaxial distance (normal to z-axis or tomograph axis) of 64 bins each of width 0.4717 cm. 60 angles around the object were simulated. The FWHM resolution energy of the NaI was set equal to the experimental value, that is 10% centered at 140 keV.

In order to get the same variance as the mean estimator, 3×10^8 histories representing 2.37×10^{10} decays were tracked, that is each history had an initial weight of $w_0 = 79$ "real photons decayed". After tracking, collimating and detecting these decays, the sum of the overall counters in the system reached 1.85×10^6 weights. Thus, the same number of experimentally detected counts. The computer time for the simulation on a Pentium III with 2 800MHz processors in monoprocessor mode was 9.7 hours using all the variance reduction techniques available.

3.4.3 Results

Comparison of the results are divided into two levels:

1. Quantitative: $t-Student$ test on image projections: In the first level the projections were compared with each other using a statistical comparison based on obtaining a $t - value$ at each detector bin A of the system based on the following:

$$t_A = \frac{N_{A_{SimSET}} - N_{A_{exp}}}{\sum_{h=1}^{h=N_h} w(A)^2 + N_{A_{exp}}} \tag{3.33}$$

A statistical distribution of t-values was obtained. Following the t-test conditions, if the null hypothesis was not to be rejected, then both distributions had to present $t - values$ distributed as normal variables:

Those results are presented in Table 3.3 and 3.4.

Both t-Student values at different thresholds (N_A) present similar distributions. Thus, the projection data set follows a Gaussian distribution at this level of counts.

Parameter	Distribution
Number of bins $t_A \leq 1$	68.27%
Number of bins $t_A \leq 2$	95.45%
Number of bins $t_A \leq 3$	99.73%

Tab. 3.2: T-Student values for the normal distribution z(0,1)

Parameter	Results	Distribution
Number of detector bins	3840	
Number of valid bins	2702	
Number of bins $t_A \leq 1$	1708	63.21%
Number of bins $t_A \leq 2$	2467	91.30%
Number of bins $t_A \leq 3$	2702	98.59%

Tab. 3.3: T-Student ttest30 ($N_A \geq 30$) on results of the modified SimSET.

The differences could be justified by the non-simulated phenomena of the efficiency of the crystal depending the photon energy and the noise effect.

2. Qualitative: the experimental and simulated sinogram projections may be compared in Figure 3.4.

As is shown in Figure 3.5 the variance obtained in the simulation using the stopping criteria was equal to the number of counts of the study. These results were compared with the estimated variance of SimSET using the variance estimator (QF).

3.4.4 Discussion

The results, both quantitative and qualitative, demonstrate the feasibility of SimSET as a virtual phantom simulator for SPECT studies. The application of SimSET in other

Parameter	Results	Distribution
Number of detector bins	3840	
Number of valid bins	2896	
Number of bins $t_A \leq 1$	1770	62.50%
Number of bins $t_A \leq 2$	2640	90.62%
Number of bins $t_A \leq 3$	2858	98.37%

Tab. 3.4: T-Student ttest5 ($N_A \geq 5$) on results of the modified SimSET.

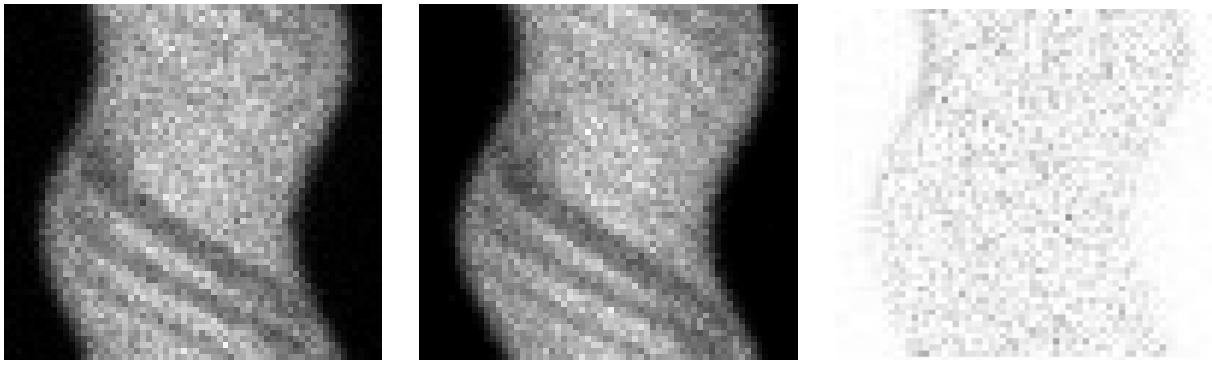

Fig. 3.4: From left to right: Experimental and simulated sinograms with their corresponding image of difference

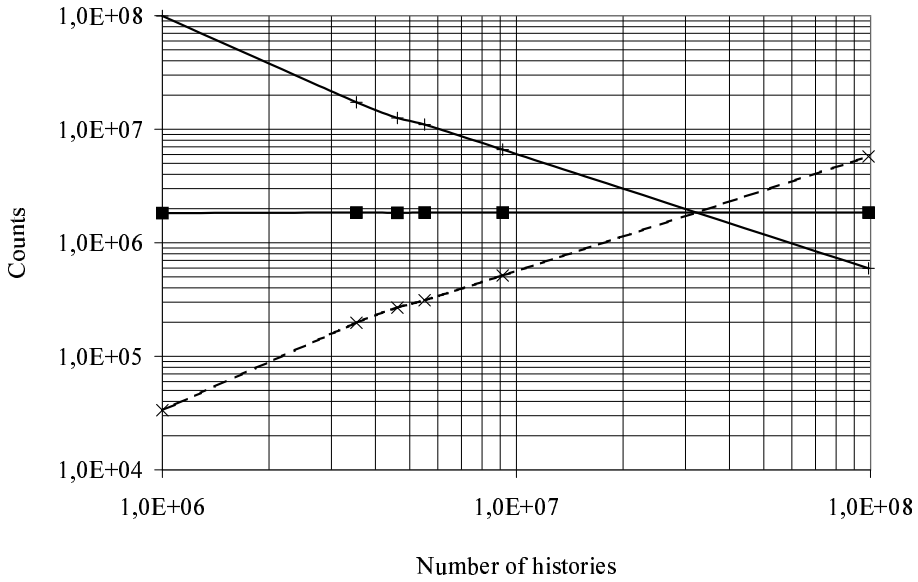

Fig. 3.5: The simulated squared sum of weights (estimated variance) is represented by the line with vertical crosses. The mean number of detected counts is shown by the line with squares. The dashed line represents the associated variance to a "real count" simulation calculated by SimSET using the QF factor and the number of accepted photons (see Appendix A). All the lines intersect at the same point: the level of detected counts of the study according to our stopping criteria.

Nuclear Medicine studies with other virtual phantom simulators such as the Hoffmann brain phantom [61, 63] or new models of cardiac phantoms [15, 75] has proved to be fesible. The modified SimSET has been revealed as a qualified tool for the optimization of reconstruction algorithms and the analysis of the wide range of parameters that have to be adjusted in clinical trials.

Including variance techniques allows a speed-up factor of 7 compared with the Analogue Monte Carlo simulation. In Chapter 6 a new variance reduction technique for the SimSET code is used in order to accelerate the simulation.

4. MC STUDY OF THE PSF FOR LEHR COLLIMATORS

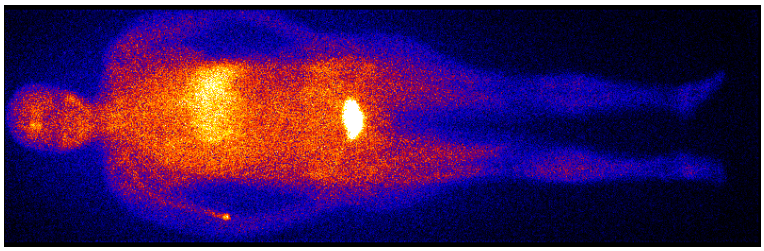

"Definition of Diagnostic (*diagnōstik*) : A compound administered for the diagnosis (*Diagnostōs*: equivalent to be distinguished) of an abnormal condition of the body or mind. That when excreted and analyzed indicates a specific pathology."
Webster's Dictionary

4.1 Introduction

Accurate modelling of the PSF is needed to perform iterative reconstruction and SPECT quantification. There are different approaches to modelling of this kind. Metz [56] and Tsui [83] models, based only on the geometric component of the point spread function (PSF), analytically determine the intersections between the aperture functions of round holes using the Fourier transform in the frequency domain. However, Frey et al. [32] improved in an easy way the modelling of the PSF using geometric approaches of the density probability per unit of area. These models determine the intersections between the aperture functions of round holes using analytical formulae in the real domain. All those models have the following limitation: only take into account the geometric component of the PSF.

Other studies model the septal penetration component by means of numerical ray tracing techniques [64], [6] in order to obtain a unique expression to describe the whole PSF without any Monte Carlo nor integral method beside. This method is limited also by only taking into account the geometric component of the PSF. An extended description of each model is presented in Chapter 6.

However, a global study including coherent (Rayleigh) and incoherent (Compton) scattering is not feasible with deterministic methods described above. A complete characterization of the collimator response requires the use of Monte Carlo simulation techniques, thus enabling the incorporation of all the PSF components for any source energy. It has been shown that Monte Carlo calculations simulate radial PSFs and energy spectra for parallel collimators in reasonable computation time [52], [84], [22]. The aim of the work presented in this section is to extend previous studies by analyzing the geometric, septal penetration, coherent and incoherent scatter components as a function of source position for a fan beam collimator with a detailed hexagonal hole array. The modelling of the collimator hole is important since the sensitivity of the system may differ due to changes in its shape [84].

De Vries et. al demonstrated that scatter component can be particularly important when the photon energy is increased [84]. This effect happens when imaging low or medium energy isotope in the presence of high energy contaminant photons which can be detected in the desired energy window after scattering. The next chapter analyzes the influence of the photon energy in the PSF functions.

4.2 Materials and Methods

4.2.1 Description of the simulation program

Simulation of photon transport was carried out by using the Monte Carlo code PENELOPE [76] [72] [3], which includes a set of geometry routines capable of handling any object formed by homogeneous bodies limited by quadric surfaces (such as planes, cylinders, spheres, etc.). The user is required to write a simple main steering program, which, among other things, keeps score of the quantities of interest—See Appendix C—.

PENELOPE performs Monte Carlo simulation of electron-photon showers in arbitrary materials. The adopted scattering models, which give a reliable description of radiation transport in the energy range from about 1 keV up to 1 GeV, combine numerical total cross sections with simple analytical differential cross sections for the different interaction mechanisms. Coherent scattering of photons is described using the classical Thompson differential cross section (DCS) and an analytical atomic form factor. Incoherent scattering is described by means of a DCS calculated from the relativistic impulse approximation, thus accounting for electron binding effects and Doppler broadening, which are non-negligible at the low photon energies encountered in our application. Cross sections for photoelectric absorption, on the other hand, are interpolated from a table generated by the XCOM program [10] and estimated to be accurate to within a few percent for energies above 1 keV. Although PENELOPE includes the simulation of pair production and secondary radiation (x-rays from vacancies in the K-shell and Auger electrons), these

interactions can be neglected for the energy window considered in our application (126 to 156 keV for ^{99m}Tc imaging).

To prevent the geometry routines from carrying all the holes each time a photon travels through the collimator, an approach that would have represented an excessively large amount of data, the description of the geometry was split into two steps. First, during the initialization, all the centers and elongations for each hole were stored in a look-up table which took into account all the characteristic parameters such as the focal length, collimator thickness, etc. This table remained unchanged during all the simulation. Each hole center was calculated using the recurrence relation defined by:

$$X_n = X_{n-1} + \frac{\Delta R_0}{\cos(\psi_{n-1})} \tag{4.1}$$

$$cos(\psi_{n-1}) = \frac{F}{\sqrt{F^2 + X_{n-1}^2}} \tag{4.2}$$

where X_n is the position of the center of the n-th hole on the fan beam axis (x-axis), ΔR_0 is the distance between two hole centers at the origin ($X_0 = 0$) in the fan beam direction, and $\frac{1}{\cos(\psi_{n-1})}$ is the elongation factor depending on the angle ψ_{n-1}, between the axis of the (n-1)-th hole and the central axis. As the point source moved away from the central axis, the elongation factor increases and the effective values of hole radius and the septa rose by 20%.

Once the two basic rows were defined with all the X_n centers, the whole collimator was filled with a set of holes obtained by a constant translation along the y-axis. The hole pattern was validated by measuring the position of the holes with a ruler. Calculated and experimental hole locations showed good agreement not only near the z-axis but also away from it.

The first elongation factor was set to $\frac{1}{\cos(\psi_0)} = 1$ and the x-coordinates to $X_0 = 0$ and $X_1 = \Delta R_0$. The parameter ΔR_0 depends on the hole shape and is measured with a ruler on the front plane collimator. This program allow the inclusion of different hole shapes which affects widely the sensibility and the final resolution:

1. Hexagonal shaped hole

2. Round shaped hole

3. Squared shaped hole

4. Others defined by the user

After setting up the look-up table, the second step consisted of tracking each photon through a local hole array around the impact point. Each time a photon reached the front

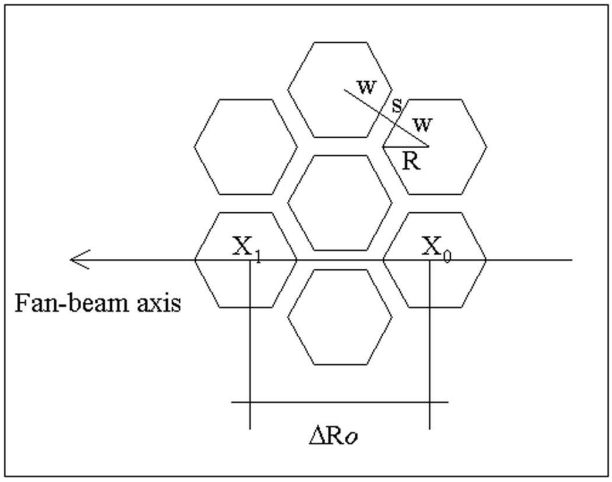

Fig. 4.1: Hole net at the front plane collimator

plane of the collimator, a set of N holes centered at the closest position to the impact point was defined using the information stored in the look-up table.

We included a study with different hole array sizes around each impact point, that is, with different values of N. The CPU time increases non linearly with N since more time is spent to track the particle through the hole surfaces. Thus, this study compared the results obtained with arrays consisting of 19, 39 and 83 holes in order to evaluate the minimum CPU time required to get correct results for different point sources. Figure 4.2 shows a hole array including 19 elements centered on the fan beam axis.

Each photon was emitted within a solid angle Ω smaller than 4π in order to save computation time. Simulation results were corrected afterwards to account for this fact by including a weight factor for each photon. Ω was selected by a geometric approach [65] using two times (safety factor = 2.0) X_M, the maximum distance reached by photons passing through collimator—for a more detailed description see Appendix C—. In this way, all the ignored holes had a negligible contribution to the studied quantities and the simulated results reach an error below 3% in worst case with a simulation time of few hours.

The simulation code controlled all the photon state variables such as energy, position, direction, weight, type of interaction, number of crossed septa, hole number and material at each particle track. The main program managed all this information in order to keep score of the quantities of interest for each study.

Each photon reaching the detector layer was flagged according to its past interactions as follows:

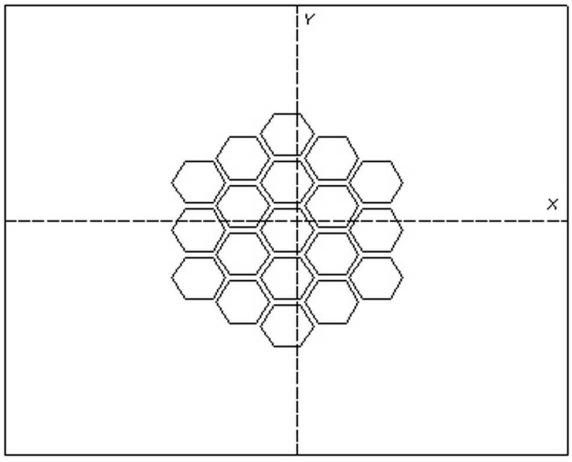

Fig. 4.2: Final size for the hole array used as for the simulation tracking inside the collimator

1. 1 for geometric photons (no interaction suffered and no septa crossed)

2. 2 for septal penetration (no interaction, one or more septa crossed)

3. 3 for photons that have undergone a coherent interaction at some point

4. 4 for photons that have undergone an incoherent interaction

This classification allowed us to differentiate contributions to the final image from the different components.

The detector layer was just a geometric plane defined at a distance B from the back-plane collimator. Thus the model used in this work only simulates the collimator effects and does not include the detector effects.

This simulation tool also allows us to explore the properties of different geometries and hole shape designs for parallel or fan beam collimators. We studied square hole shapes by modifying the parameter ΔR_0 in order to show the influence of the hole shape on the collimator sensitivity.

4.2.2 Experimental measurements

To validate the Monte Carlo calculation, sensitivity values obtained from simulated PSFs for a fan beam collimator were compared with those obtained from experimental PSFs.

To this end, a cavity (1.5 mm in diameter and 4.5 mL in volume) inside a thin piece of Lucite was filled with 15 MBq of ^{99m}Tc. This point source was placed at different heights (z equal to 5, 10, 15, 20, 25 and 30 cm) on the central axis and also displaced from the z-axis (x equal to 2, 4, 8, 12 and 16 cm). Images were acquired with a double-headed Helix (Elscint, Haifa) camera with a fan beam collimator.

In the case of an hexagonal hole geometry, (see Figure 4.1), the fan beam had a measured focal length F of 35.5 cm [65], a distance between hole centers (ΔR_0) equal to 0.2846 cm in the fan beam axis, a septal thickness s of 0.02 cm and a collimator width (L) of 4 cm. In the simulation study the detector layer was situated at a distance B of 0.8 cm. from the collimator back plane.

As shown in Figure 4.3 a Lucite holder was built in order to place the point source at different locations along the z-axis and separated from it.

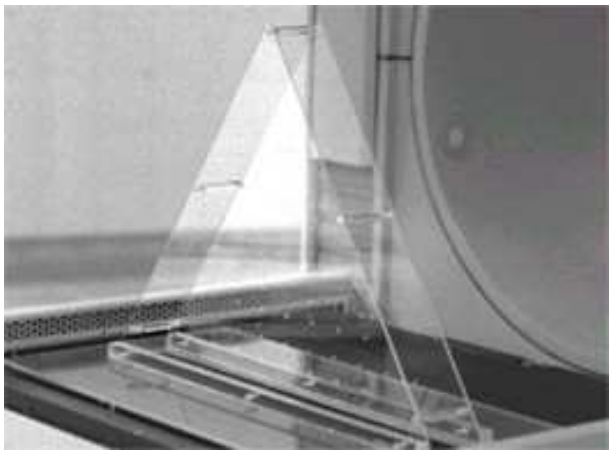

Fig. 4.3: Lucite holder for the different locations of the point source

4.3 Results

A comparison of sensitivity S for different hole array sizes N_i is presented in table 4.3. The sensitivity values were obtained as the number of photons reaching the detector per emitted photon. The PSF was taken at different heights along the central z-axis with a different number of holes (N_1, N_2 and N_3) around each impact point.

The maximum difference in sensitivity was reached at $z = 30$ cm and its value was lower than 0.5% which is of the same order as the statistical uncertainty of the Monte Carlo simulations presented in this study. The computational time needed for each simulation was $T_{N_1} = 4.7$ h, $T_{N_2} = 9.9$ h and $T_{N_3} = 46.1$ h. The ratio between the biggest and the

z (cm)	5	10	15	20	25	30
$N_1 = 19$	8.13	9.75	12.15	16.07	23.79	45.17
$N_2 = 39$	8.13	9.76	12.13	16.08	23.76	45.24
$N_3 = 83$	8.13	9.82	12.19	16.09	23.89	45.42

Tab. 4.1: Sensitivity values $\times 10^{-5}$ at different heights along the central z-axis with different array sizes

smallest array was about 10. Given the large time difference combined with the negligible change in sensitivity, we chose to perform our study with the minimum number of holes $N_1 = 19$.

Figure 7.6 shows the total PSF obtained from the Monte Carlo simulation with the source at $z = 10$ cm.

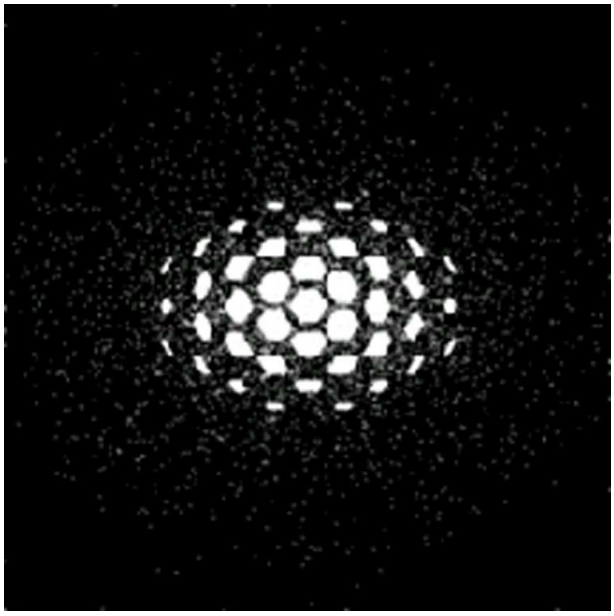

Fig. 4.4: Total PSF image at z=15 cm

In this Figure the geometric component is shown to be the predominant factor. The discrete collimator hole structure is clearly visible because the detector blurring effect has not been simulated. Other components such as septal penetration, Compton and Rayleigh scattering have a slight effect in the whole image.

Sensitivity results along z-axis heights are presented in table 4.3. The values of the first row S indicate the absolute probabilities of detecting a photon per particle emitted. The

second row $SMC/SMC5$ corresponds to the relative simulated sensitivities with respect to the sensitivity when the source is located at $z = 5$ cm. The third row S_{exp}/S_{exp5} shows the relative experimental sensitivities.

z (cm)	5	10	15	20	25	30
S ($x10^{-5}$)	8.13	9.75	12.15	16.07	23.79	45.17
S_{MC}/S_{MC5}	1.00	1.20	1.49	1.98	2.92	5.56
S_{exp}/S_{exp5}	1.00	1.21	1.51	1.99	2.88	5.32

Tab. 4.2: Sensitivity values and ratios at different heights

Figure 4.5 shows the four PSF components. The images were obtained taking into account the flags assigned to the photons when they reached the detector surface, as described above. Each image is normalized to its maximum.

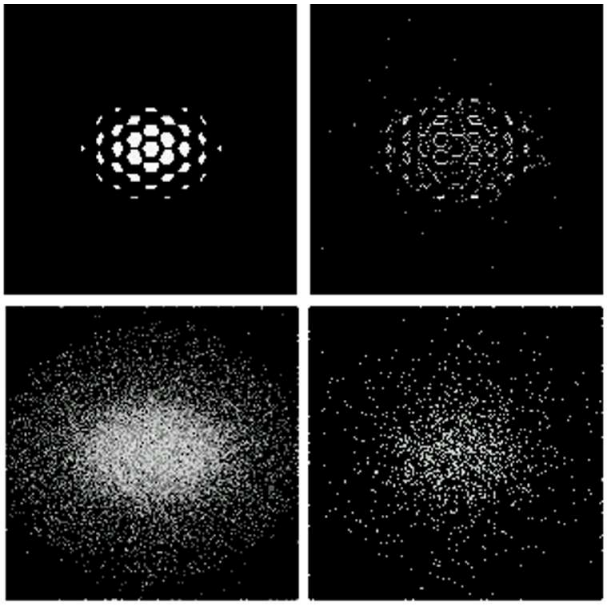

Fig. 4.5: Simulated geometric (top left), septal penetration (top right), coherent scatter (bottom left) and incoherent scatter (bottom right) PSF components for a point source located at (x,y,z) = (0,0,10) cm

The contribution of each component to the total PSF is presented in table 4.3.

These results show that for ^{99m}Tc imaging the major contribution to the fan beam PSF is the geometric component, which represents approximately 95.1% of total PSF. Septal penetration is the second major contributor, with a 3.7%, and Rayleigh photons are the

z (cm)	5	10	15	20	25	30
Geometric	95.3	95.0	95.1	95.1	95.2	95.2
Septal penet.	3.5	3.9	3.7	3.7	3.7	3.6
Coher. Scatt	1.1	1.1	1.0	1.1	1.1	1.1
Incoh. Scatt	0.1	0.1	0.1	0.1	0.1	0.1

Tab. 4.3: Contribution of each component to the PSF *in*%

third component, with a contribution of 1.1%. The incoherent scattering component is almost negligible, with an average contribution of 0.1%.

This characterization study was performed also off the z-axis. The corresponding results are presented in table 4.3. The values in the first row presents the absolute probabilities of detecting a photon per particle emitted. The second row values S_{MC}/S_{MC} correspond to the simulated sensitivities with respect to those obtained when the source is located at the same height on the z-axis. The third row S_{exp}/S_{exp5} shows the relative experimental sensitivities in the same terms. The source point locations are represented in the form (X, Z) locations.

x,z (cm)	(16,5)	(16,10)	(12,15)	(8,20)	(4,25)	(2,30)
S ($x10^{-5}$)	6.40	7.00	9.07	12.65	19.73	39.89
S_{MC}/S_{MC5}	0.78	0.70	0.71	0.79	0.84	0.93
S_{exp}/S_{exp5}	0.79	0.72	0.75	0.79	0.83	0.88

Tab. 4.4: Sensitivity values for the off-axis PSF

Table 4.3 presents the same results as table 4.3 for the off-axis case.

x,z (cm)	(16,5)	(16,10)	(12,15)	(8,20)	(4,25)	(2,30)
Geometric	95.8	95.6	95.6	95.4	95.2	95.3
Sep. penet.	3.1	3.3	3.3	3.5	3.6	3.5
Coh. Scatt.	1.0	1.0	1.0	1.0	1.1	1.1
Incoh. Scatt.	0.1	0.1	0.1	0.1	0.1	0.1

Tab. 4.5: Contributions of each component of the off-axis PSF *in*%

To provide further elements of validation, the PSF was convolved with the intrinsic response of the detector and the resulting blurred PSF was collapsed and compared with PSF obtained experimentally. Table 4.3 presents a comparison of the FWHMs (Full Width at Half Maximum) obtained in this way.

z (cm)	5	10	15	20	25	30
FWHMMC	0.56	0.85	1.36	2.18	3.83	8.33
FWHMEXP.	0.58	0.89	1.37	2.21	3.71	8.06
Relative error (%)	3	5	1	1	3	3

Tab. 4.6: Experimental and simulated FWHM *incm*

Also, Table 4.3 shows the analogous results for the FWTM (Full Width at Tenth Maximum). As in the former case, the agreement is excellent.

z (cm)	5	10	15	20	25	30
FWTMMC	1.04	1.50	2.30	3.68	6.44	14.54
FWTMEXP.	1.11	1.55	2.21	3.76	6.41	14.82
Relative error (%)	6	3	4	2	0	2

Tab. 4.7: Experimental and simulated FWTM *incm*

In Figure 4.6, the simulated geometrical PSF convolved with the intrinsic response of the detector $GPSF$ is fitted to a Gaussian. The corresponding correlation coefficient is 0.998, thus justifying the use of Gaussian functions in collimator modelling studies.

Finally, sensitivity differences between hexagonal and square shaped hole collimators are presented in table 4.3. Two different types of squares were simulated. First type, (Square 1), it was assumed the same septa thickness and same open area per hole as in the hexagonal case. Second type, (Square 2), the hole area and lead content per unit detector area were assumed to be equal than those corresponding to the hexagonal hole collimator.

z (cm)	5	10	15	20	25	30
Hexagon	8.13	9.75	12.15	16.07	23.79	45.17
Square 1	8.49	9.92	12.31	16.22	24.10	46.47
Square 2	8.51	10.19	12.64	16.73	24.79	47.40

Tab. 4.8: Sensitivity values for different hole shapes ($x10^{-5}$)

4.4 Discussion

Results of relative sensitivity from table I4.3 indicate that Monte Carlo values closely match those obtained from the experimental measurements with differences less than 2%

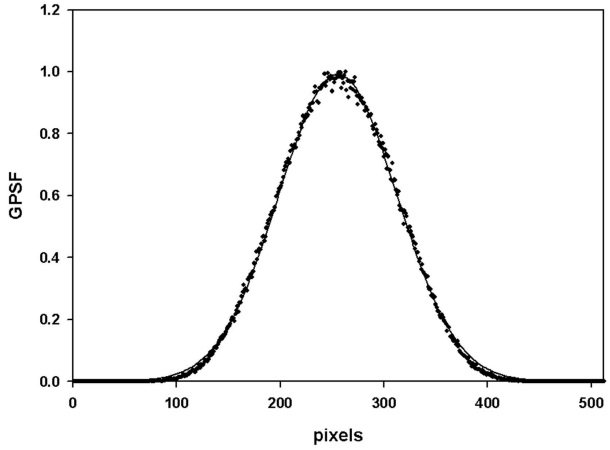

Fig. 4.6: The simulated $GPSF$ (dots) and a Gaussian function (solid line)

in the range from z=5 to 25 cm. Differences up to 5% were found at the highest source location (z=30cm), caused by the fact that when the source is placed near the focal line, small displacements around the exact position result in strong fluctuations in fan beam sensitivity. The sensitivity results off the z-axis present a maximum difference of 5.4%.

Tables 4.3 and 4.3 show that for ^{99m}Tc imaging with a fan beam collimator, the largest contribution to the sensitivity is due to the geometric component. This result is in accordance with that obtained by De Vries et al. [84] with a parallel collimator. Septal penetration is the second most important contribution, its effect being equivalent to an enlargement of the size of the collimator holes. Coherent scattering represents the main scattering effect. Incoherent scattering does not appreciably contribute to the PSF. Since, for ^{99m}Tc imaging, a large fraction of photons crossing the collimator do not change their previous direction (the sum of the geometric and septal penetration terms yields 98.9% in our case), collimator scattering corrections are expected to play a minor role in reconstruction algorithms.

The change in sensitivity on the z-axis including its four components corresponds with the results obtained by only using the geometric PSF component [51]. We can explain this behavior based on the results presented in table4.3 and 4.3, where the geometrical component is kept almost constant around 95% over the whole fan beam collimator field of view. The sensitivity pattern away from the z-axis matches the law of the square of the cosine of the aperture angle well.

Finally table4.3 shows that some hole shapes give rise to sensitivities that are 4.5% higher than those found for the hexagonal case.

Ongoing work on the transport inside the detector system and the study of the PSF extensions for different point source locations will be published elsewhere. With this simulation tool, it is also possible to compare parallel and fan beam collimators for other isotope energies and geometry designs.

5. MC SIMULATION FOR HIGH ENERGY GAMMA-RAY PSF

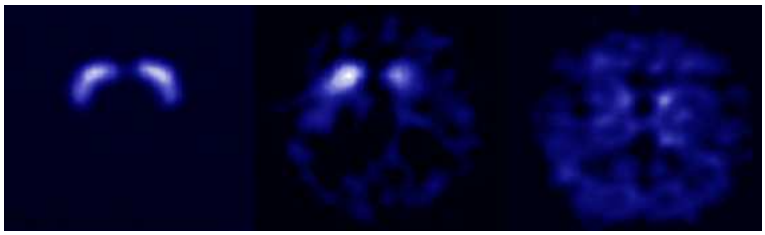

The diagnosis of Parkinson using a neurotransmission SPECT study. Normal —left— and pathological —right— situations.

5.1 Introduction

For relatively low energies, modelling of the PSF can be accomplished by only taking into account the geometric component [32, 65], that is, by transporting photons as if these particles were absorbed whenever they reach the collimator septa. The geometric component can be determined by means of deterministic models [56, 83, 32] or by having recourse to numerical ray tracing techniques [6, 62]. A different approach consists of using Monte Carlo simulation to describe radiation transport in full, a method that enables the evaluation of the relative importance of the geometric component as compared with other effects, namely, septal penetration, coherent (Rayleigh) scattering and incoherent (Compton) scattering [84, 18]. As will be seen later, the non-geometric effects turn out to be non-negligible at relatively high energies, such as those encountered when using certain radioisotopes.

The radionuclides most commonly used in neurotransmission SPECT studies are ^{99m}Tc and ^{123}I, with different ligands. In particular, ^{123}I is a gamma emitter whose photon spectrum is dominated by a line at 159 keV with a yield (relative to the other gammas) of 96.5% [85]. The energies, in keV, and relative yields (in parenthesis) of the other emission lines are as follows: 248 (0.08%), 281 (0.09%), 346 (0.15%), 440 (0.50%), 505 (0.37%), 529 (1.62%), 538 (0.44%), 624 (0.10%) and 783 (0.07%). Only those rays with a yield larger than 0.06% are considered here.

In this chapter we study the effect produced in the image by photons from ^{123}I with energies equal to 248 keV and above and how this effect, which we shall call high-energy contamination (the collimator design and the main detection window are usually arranged so as to detect the more numerous 159 keV gammas), depends on the collimator configuration. Two configurations are considered namely, the fan beam and the parallel. The ultimate goal is to provide relevant information that contributes to the future development of an accurate scattering correction algorithm for neurotransmission SPECT studies.

The rest of this chapter is organized as follows. In section 5.2, we introduce the methodology employed to simulate the detection system. Sections 5.3 and 5.4 are devoted to presenting simulation and experimental results respectively, the latter as a means of validation of the simulation tool employed in this work. Finally, in section 5.5 some conclusions are drawn.

5.2 Monte Carlo simulation

The simulation of the radiation transport process was carried out by using the Monte Carlo code PENELOPE [73, 76]. The PENELOPE package includes a set of geometry routines (PENGEOM) which is capable of handling any object formed by homogeneous bodies limited by quadric surfaces (such as planes, cylinders, spheres, etc.). In this code system, the user is responsible for writing a simple steering main program from where some of the PENELOPE and PENGEOM subroutines are called to perform the tracking of the particles that are simulated.

In our case, the complexity associated with the description of the collimator geometry prevented us from using PENGEOM in the standard way. In a previous work [18], in which we presented a study of the modelling of the PSF response to ^{99m}Tc, we relied on a trick that essentially consisted of defining only the portion of the hole structure forming the collimator that is closest to the photon location as it travels across the material system. The size of this substructure, which we shall call a reduced hole array (RHA), was set so as to ensure that the probability for a photon to leave it before being absorbed is negligible and it was centred close to the point where the photon initially entered the collimator geometry. In this previous study, a RHA with 19 holes (see figure 5.1) was sufficient due to the small photon mean free path (MFP) relative to the septa thickness. This method reduced the amount of geometry-related computing burden to a fraction of what would be necessary if the whole collimator had been described in full.

Unfortunately, this approach is not completely adequate in the current case, since the high-energy photons of ^{123}I have relatively large MFPs and, hence, a non-negligible probability of leaving the initial RHA. Indeed, at 159 keV the photon MFP in lead (Pb) is 0.05 cm whereas at 529 keV it is 0.58 cm. To overcome this difficulty, a "mobile" RHA was employed. The idea here is that each 19-hole-array structure is replaced on-the-fly by

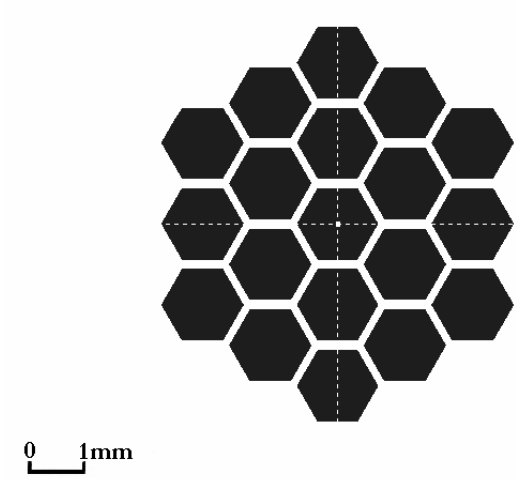

Fig. 5.1: Geometric configuration of the reduced hole array (RHA) used in the simulations of the different collimators.

a new one whenever the photon crosses its outermost limiting surface. The newly created array, whose central hole is selected among all the collimator holes by finding the closest to the photon position, substitutes the old array in the computer memory. This approach proved to be more convenient than defining a larger "static" RHA because it requires shorter simulation times and less computer memory.

Another issue refers to the optimal user-defined simulation parameters, and most importantly, to the selected absorption energies—called `Eabs` in PENELOPE. When the particle kinetic energy falls below `Eabs` (which can be different for photons and electrons), its simulation is discontinued and the energy is assumed to be deposited locally. Higher values of `Eabs` imply faster simulations, but they also reduce the accuracy with which the transport process is described. In order to achieve a convenient trade off between speed and accuracy, a set of preliminary simulations with variable `Eabs` values were performed and the corresponding photon detection probabilities calculated. The conclusion was that an absorption energy of 100 keV provides a nearly optimal compromise.

The detector was modelled as a 0.95 cm (∼3/8") NaI crystal covered upstream by an 0.12 cm-thick aluminium layer, which forms the protective casing, and downstream by a 6.6 cm-thick layer of Pyrex with a reduced density of 2.23 g/cm^3. This latter element, whose thickness has been set following the model based on the work of De Vries et al. [84], introduces a certain contribution from backscattered photons. The energy resolution was described by means of a Gaussian distribution with a full width at half maximum (FWHM) of 11% at 159 keV and was assumed to be proportional to the square root of the deposited energy.

After a photon history[1] is generated, the amount of energy actually deposited in the crystal is determined by sampling a Gaussian probability distribution centred at the nominally deposited energy (i.e. the energy calculated by PENELOPE). A detection event, represented by the addition of a unit to the corresponding counter, is scored when this "convolved" energy falls inside the detection window, which in our simulations was set from 143 to 175 keV. Furthermore, each count must be assigned to a spatial bin lying on a plane parallel to the crystal surface in order to form a 2D image. For this purpose, the nominal co-ordinate (say x) of a detection event is calculated as the weighted average of the co-ordinates (each of the x_i's) corresponding to the i-th energy deposition event occurring during the particle history. The weight of the i-th co-ordinate value is the energy deposited in that event. Similarly to the deposited energy case, the x co-ordinate actually assigned to a detection event is obtained by sampling a Gaussian distribution centred at the nominal value that comes out of the averaging process. The FWHM of this Gaussian was experimentally determined to be 0.40 cm by using a narrow pencil beam impinging perpendicularly on the crystal surface. Notice that this process of spatial blurring takes into account the intrinsic spatial resolution of the compound crystal-photomultipliers system only approximately, since a certain contribution from scattering inside the crystal is unavoidably embedded in the measurement. The validity of this approximation is verified a posteriori by noticing that the global spatial FWHM of the PSF (i.e. that arising from the transport through the collimator and produced by an isotropically emitting source) is much larger than the intrinsic component alone.

Two collimator configurations were considered. The first was a parallel collimator with a field of view of 50×25 cm^2. The holes, hexagonal in shape, had a radius equal to 0.0866 cm, a septal thickness of 0.02 cm and a length of 4 cm. The second configuration was a fan beam collimator with dimensions equal to those of the parallel case and a focal distance of 35.5 cm. The hole radii and their separation at mid-plane of the collimator were also the same as in the parallel case. Hereafter, we shall consider a co-ordinate system in which the z axis is perpendicular to the collimator front plane and intersects the focal line. The center of co-ordinates lies on the same collimator plane (see figure 5.2). In this co-ordinate system, both the separation between neighbouring holes and their radii change along the x axis, but not along the y axis. For details on how this variation is modelled, the reader is referred to [18].

Two quantities, which we have termed absolute and partial sensitivities, are evaluated for the different configurations. The absolute sensitivity, $A(E)$, is defined as the probability of scoring a count in the energy window (143 to 175 keV) when a photon of energy E is emitted isotropically from the source location. The partial sensitivity, S_i, corresponding

[1] We shall refer to the "history" of a primary particle to denote the simulation of this particle *and* of all the secondaries it generates.

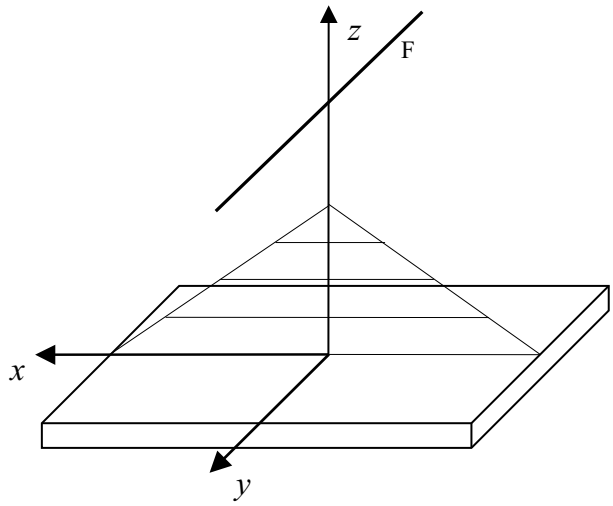

Fig. 5.2: Diagram showing the position of the co-ordinate axis with respect to the collimator surface (x-y plane). In this plot, F represents the focal line. The FOV subtended by the collimator seen from a point lying under F is shown as a triangle.

to the i-th gamma line of ^{123}I (with energy E_i) is defined as

$$S_i \equiv A(E_i)\, Y_i \tag{5.1}$$

where Y_i stands for the *relative* yield of the considered line. The sum of the Y_i's considered here adds up to 99.91%. S_i represents the probability that a photon emitted from the ^{123}I source has an energy E_i and produces a count in the energy window of the detector. The sum of all S_i's, which shall be denoted S_{I}, is interpreted as the probability of obtaining a count when a photon is emitted from the source, in other words, the detection efficiency. Obviously, both A and S depend on the source location.

5.3 Simulation results

In figure 5.3 the absolute sensitivities A of a parallel and a fan beam collimators are shown as functions of the photon energy for three different heights z centred on the central axis. In both cases, A increases almost linearly with energy between 250 and 540 keV, approximately. The steep increase of the sensitivity explains the fact that, although the 159 keV line of ^{123}I is almost 25 times more intense than the combination of all the more energetic lines, the contribution to the PSF of the latter is not negligible, as will be seen below.

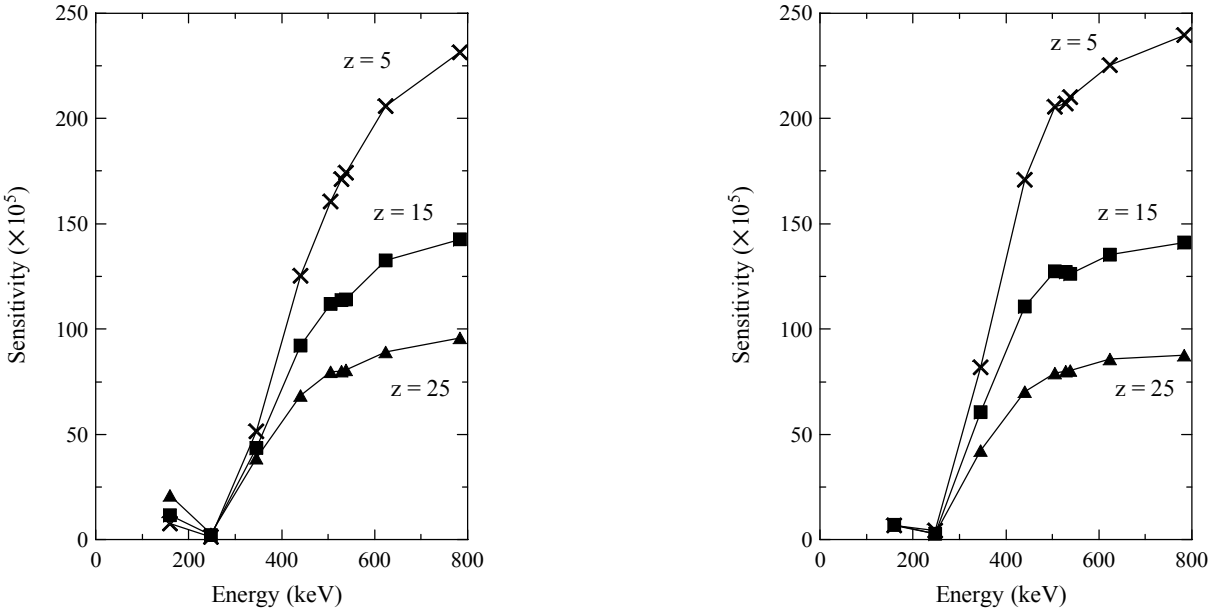

Fig. 5.3: Absolute sensitivity of a point source for the ^{123}I energies considered in this work and for three different z values on the central axis (in cm). Left– and right–hand figures display the fan beam and parallel collimator cases, respectively. Symbols have been joined by straight lines for visual aid.

The change in the sign of the partial derivative of A with respect to z at different energies for the fan beam collimator is an interesting feature that deserves some analysis. Notice that A is an increasing function of z below approximately 200 keV but it decreases above this value. This behaviour can be explained by considering the relative contribution to the PSF of the photons that have interacted in the collimator. This information is displayed in figure 5.4, where each count that contributes to the PSF is classified according to the type of the last interaction suffered by the considered photon, i.e. it is either a geometrical (no interaction and no septa crossing), a septal (no interaction and at least one septa crossing), a Rayleigh or a Compton event (last interaction).

In the energy range where the geometrical component predominates, that is, around 159 keV, A is expected to increase with respect to z (up to the focal line) since the solid angle covered by the portion of the detector "optically seen" from the source through the holes increases rapidly as its position approaches the focal line. For higher energies, on the other hand, the main contribution comes from septal penetration and Compton scattered photons. In this case, one expects the sensitivity to be mainly determined by the solid angle with which the whole collimator is seen from the source. Since this solid angle decreases with z, so does S. These effects explain, as anticipated, the trends observed in figure 5.3.

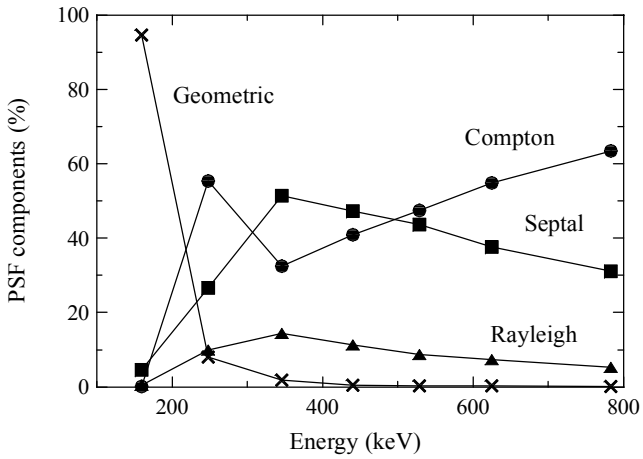

Fig. 5.4: Different contributions to the PSF of the fan beam collimator as a function of the energy of the primary photons. In all cases, the photon source was located at $z = 15$ cm. Straight lines have been used to join the symbols for visual aid.

Figure 5.5 shows the variation of the partial sensitivity with source height for the two collimators considered. The partial sensitivity S_{159} corresponding to the 159 keV rays is displayed separately from the sum of all the others. If we consider the former as representative of the "signal" and the latter as the "noise" in the image, this figure indicates that the signal-to-noise ratio is better for the fan beam collimator, even quite far away from its focal line—located at 35.5 cm.

The fraction of partial sensitivity (i.e. the ratio S_i/S_{I}) corresponding to each line in the iodine spectrum is displayed in table 5.1. This ratio represents the probability that a count in the PSF has been produced by a photon of initial energy E_i and it is therefore a clear indicator of the amount of "contamination" from high-energy rays.

Figure 5.6 presents an excerpt of this data in a graphical, and more suggestive, form. Only the most relevant gamma energies have been selected. Notice that the high-energy contribution is considerably lower for the fan beam collimator.

For the sake of completeness, we have also studied the variation of the sensitivity for emission points located off-axis. The results are shown in figure 5.7.

5.4 Experimental validation

In order to validate our simulation results, PSFs produced by 511 keV annihilation photons were obtained experimentally. This energy is close to that of the second most intense line of ^{123}I (529 keV), hence the interest of this study. A sample of ^{18}F-FDG (0.92 MBq)

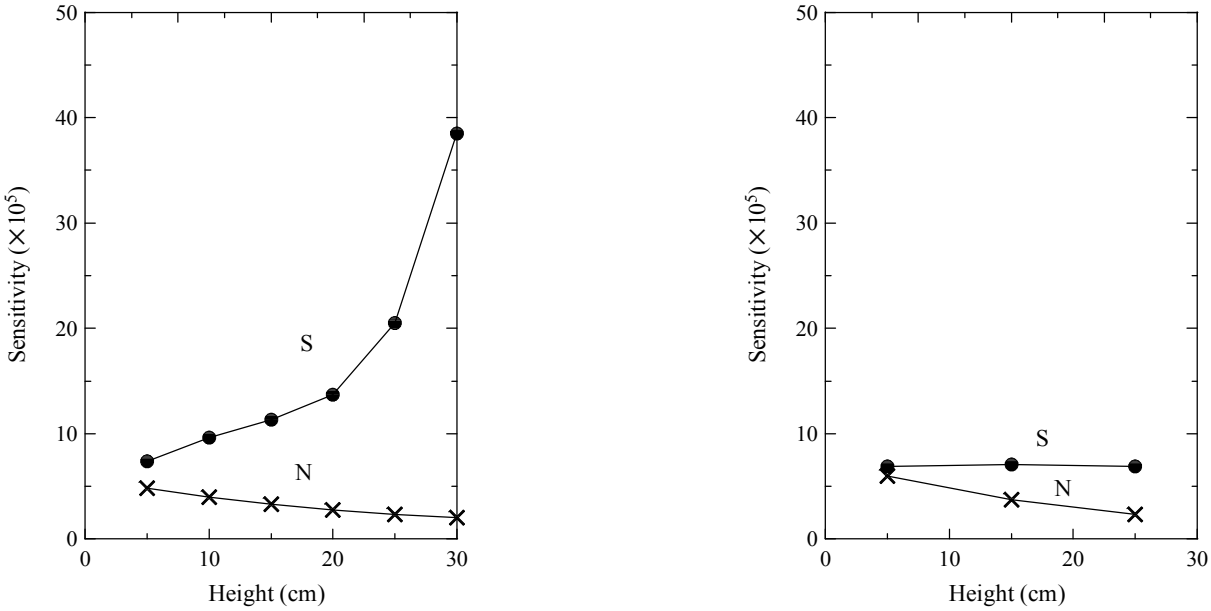

Fig. 5.5: Partial sensitivity as a function of source height for a fan beam (left) and a parallel (right) collimator. The sensitivity of the 159 keV line is marked 'S' (for 'signal') and the combined sensitivities of all the rest is marked 'N' (for 'noise'). Symbols have been joined by straight lines for visual aid.

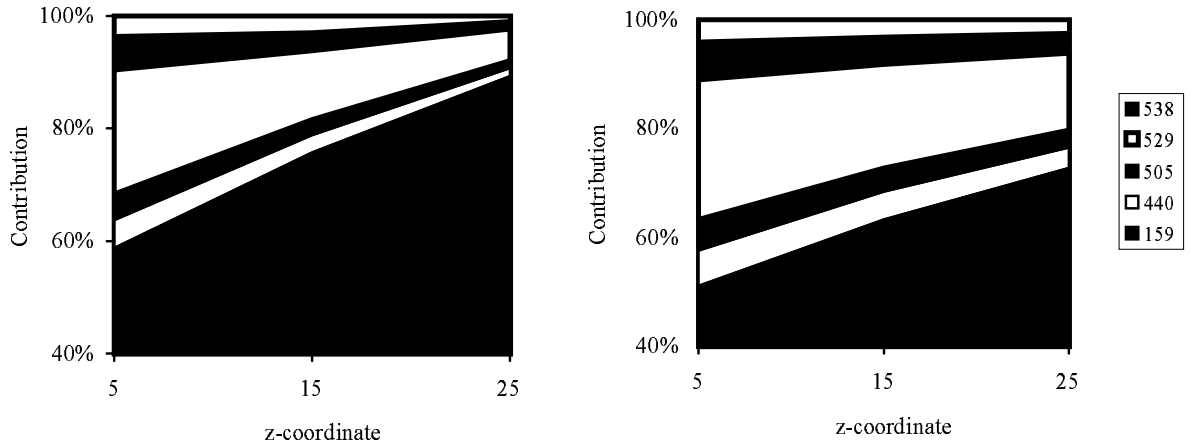

Fig. 5.6: Same data as in table 5.1. Here, the abscissas are the source height z on the central axis and the values corresponding to different energies are depicted as solid bands of alternating colours. Left– and right–graphs are fan beam and parallel collimators, respectively.

Energy (keV)	Y_i (%)	S_i/S_I (%) ($z = 5$ cm)		($z = 15$ cm)		($z = 25$ cm)	
		fan	paral	fan	paral	fan	paral
159	96.50	58.8	51.4	75.8	63.3	89.3	72.7
248	0.08	0.0	0.0	0.0	0.0	0.0	0.0
346	0.15	0.6	0.9	0.4	0.8	0.3	0.7
440	0.50	5.0	6.6	3.1	5.1	1.5	3.8
505	0.37	4.7	5.8	2.8	4.3	1.3	3.2
529	1.62	22.0	25.6	12.3	19.1	5.7	14.1
538	0.44	6.2	7.1	3.3	5.2	1.6	3.9
624	0.10	1.6	1.5	0.9	1.2	0.4	0.9
783	0.07	1.3	1.1	0.7	0.9	0.2	0.7
TOTAL	99.91	100	100	100	100	100	100
$S_\mathrm{I}(10^{-5})$		12.58	12.96	14.94	10.77	22.95	9.16

Tab. 5.1: Sensitivities of each of the ^{123}I lines considered in this work at different heights z. Left– and right–hand columns correspond to the fan beam and parallel collimator cases, respectively. The absolute uncertainty of S_i/S_I is below 5%.

was dissolved in 10 μL of water, producing a droplet with a diameter of 2.7 mm which, in our simulations, was modelled as a point source. The source was placed, by means of a Lucite holder, at various positions $(0, 0, z)$ with z equal to 5, 10, 15, 20 and 25 cm. The projections were acquired with a double-headed Helix camera (Elscint, Haifa) equipped with the fan beam collimator described above. Excellent agreement is found between experimental data and simulation results, as shown in figure 5.8. Notice also the importance of simulating the transport of secondary particles. Further calculations have provided evidence that secondary *photons* are responsible for the observed differences, i.e. secondary electrons do not play a significant role at the energies studied here, as one would expect from their short range in dense media.

In figure 5.9 the profiles obtained by summing up the counts of the PSF along either the x or the y axis are presented. Simulation and experimental results are in very good agreement and show that both profiles extend beyond the collimator boundaries, i.e. the high-energy PSF is extended over the whole FOV. This spread gives a rough idea of the difficulties associated with the development of efficient techniques to correct the PSF from contaminant high-energy rays.

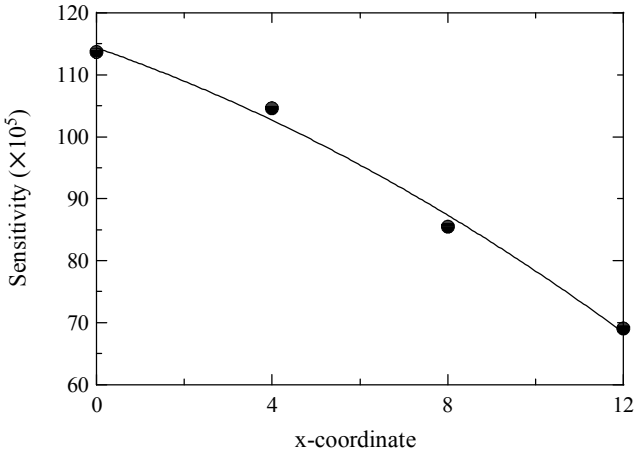

Fig. 5.7: Absolute sensitivity of 529 keV photons at different x positions and $z = 15$ cm for a fan beam collimator. The solid line is a fit performed with a second order polynomial.

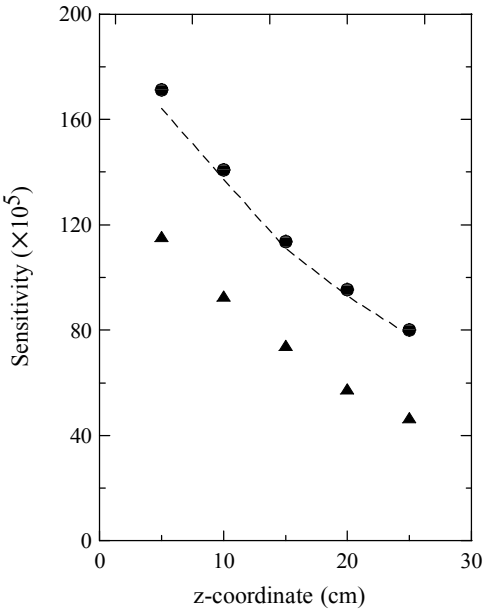

Fig. 5.8: Absolute sensitivity for 511 keV photons as a function of the distance source-collimator (z). Simulation and experimental data are the dots and the dashed line, respectively. The absolute sensitivities obtained by neglecting the transport of secondary particles are shown as triangles.

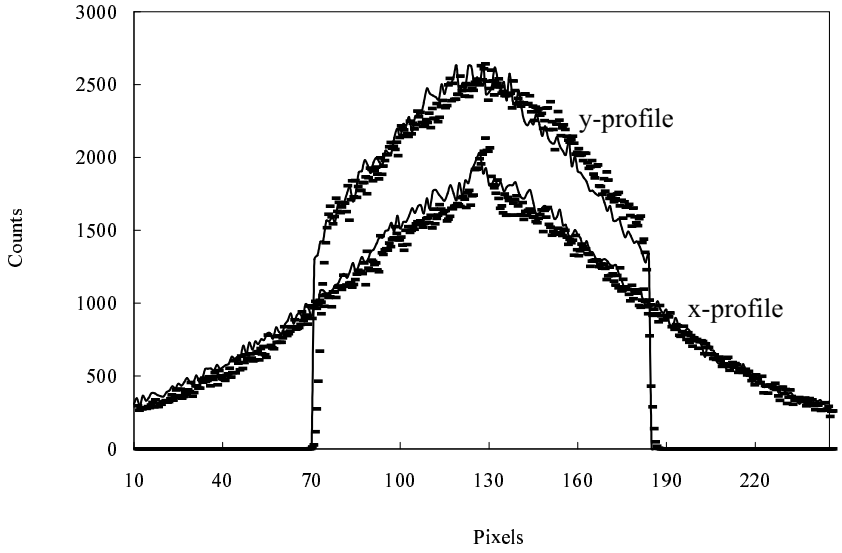

Fig. 5.9: PSF profile produced by 511 keV photons from a point source at $z = 15$ cm. Symbols represent simulated results and solid lines the experimental data. The curves labelled x and y were obtained by summing up the counts along the corresponding axis. The simulated y-profile has been normalized to the largest experimental data. The same scaling factor has also been applied to the x-profile.

5.5 Discussion

For low-energy rays, the predominant component of the PSF is determined by the geometric pattern of the holes in the collimator. These PSFs were discussed by [56, 83] for parallel collimators. For the fan beam model, various approaches have been adopted by different authors (see e.g. [51, 83, 32, 30, 34, 65]). The decrease of the absorption cross section and the increase of the Compton cross section for increasing photon energies causes the geometrical component to become less relevant compared with that of septal penetration and scattering when higher energy gamma rays come into play. The results presented in figure 5.4 reveal that septal penetration and Compton scattering take over the geometric part above approximately 200 keV. As pointed out by Dobbeleir and co-workers [23] as a conclusion of their experimental work, this implies that, in general, medium-energy collimators are the best choice for ^{123}I studies. However, in the particular case of brain SPECT imaging, a high spatial resolution is sought in order to permit accurate quantification and, therefore, Low-Energy High Resolution (LEHR) collimators are preferable.

This work has analyzed the sensitivities corresponding to two different LEHR, namely, a parallel and a fan beam collimators, showing that the former is more prone to "contamination" from high-energy rays than the latter. The probability that a detected event corresponds to a photon with an initial energy of 159 keV is larger for the fan beam collimator (59% to 89%) compared with the parallel collimator (51% to 72%), depending on the source-detector distance (see table 5.1). These differences may become even more relevant when scattering in the object (i.e. the patient) is also taken into account, because the higher absorption suffered by low-energy photons will produce noisier images than those obtained in this study. In this case, the increase in the number of "signal" detection events may be critical. In conclusion, according to the present analysis, the use of a fan beam collimator for brain SPECT imaging with ^{123}I is highly recommended.

We have also shown that the PSF obtained considering only the high-energy component of the ^{123}I spectrum extends over the whole FOV and has a non-Gaussian shape, a fact that renders its modelling a difficult task. As a consequence, any correction method for high-energy ray phenomena should take into account the particular collimator-detector configuration it is intended to be applied to. Work to model the contribution to the PSF of the high-energy effects described here is in progress and will be presented elsewhere.

6. THE MODELLING OF THE POINT SPREAD FUNCTION

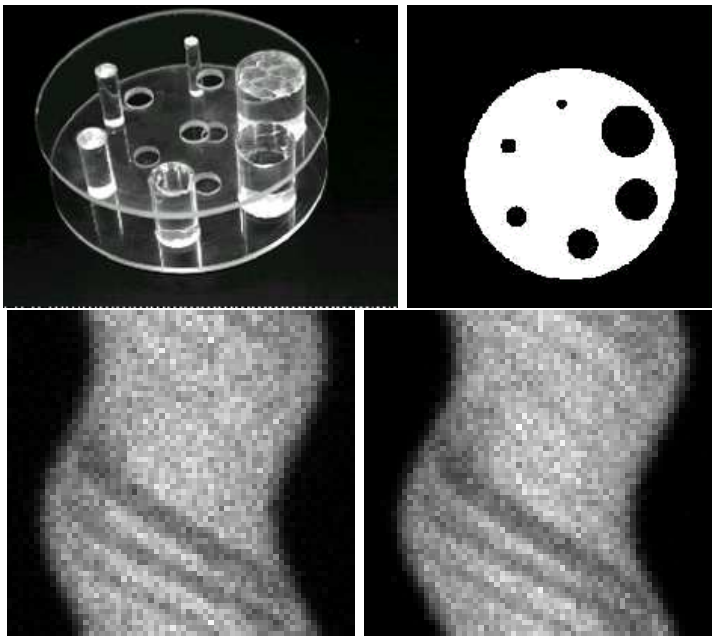

Experimental vs. Virtual phantoms.
Acquired vs. Monte Carlo simulated projections.
"Which is the difference between virtual and reality?"

6.1 Introduction

Modelling of the Point Spread Function (PSF) is required for both reconstruction algorithms and virtual phantom Monte Carlo simulators. On the one hand, iterative reconstruction algorithms require PSF modelling in order to correct the collimator/detector blurring effect in the reconstructed images. Reconstruction algorithms include the spatially dependant collimator/detector response by using PSF models. These functions are used in the calculus of the transition matrix determining the contribution of a point

source in the voxel source s_i to the projection bin p_j. On the other hand, the Monte Carlo simulators in SPECT need a PSF function in order to accelerate the tracking process through the collimator/detector system. The Monte Carlo simulation in SPECT is a slowly convergent process. As was described in Chapters 4 and 5, detailed simulation of the photon transport across the collimator/detector system using Monte Carlo techniques demands a huge computational effort. The common way to accelerate the simulation is to use a probability density function (PDF) which describes the response of the collimator/detector system. These PDFs are based on the modelling of the PSF.

PSF modelling is achieved by the following steps:

1. Individual characterization of the collimator/detector response at different source coordinates by fitting the results with known functions (Gaussian, Exponential, Linear, etc.)

2. PSF functions may be parameterized by two variables: the sensitivity η, which is defined as the number of photons detected per emitted photon and the resolution which equals the Full Width at Half Maximum (FWHM) of the image corresponding to a point source. The parameterization of these functions depends on the source coordinates and the source energy. The collimator/detector configuration is the final step.

Nevertheless, there are different approaches to modelling PSF. The direct way to obtain the PSF modelling is to measure the responses of each collimator/detector configuration experimentally. However, the experimental set up is limited to the particular configuration available at the hospital or research center. Thus this method is not useful for designing "a-priori" collimators [34] or for studying the PSF response depending on the energy of the isotope. Theoretical or non-empirical approaches are useful when modelling the "a-priori" PSF.

The "a-priori" or theoretical modelling of the PSF has been developed since the beginning of the SPECT technique. The initial derivation and basis for the Geometrical component of the Point Spread Function (PSF_G) was proposed by Metz et al. [56] in 1980. Afterwards, it was extended to convergent (cone and fan beam) collimators by Tsui et al. [83] in 1990. Both theories used the frequency domain in order to model the PSF_G but the complexity of the functions obtained did not allow their implementation in the PSF model. In 1998, Frey et al. [32] proposed a new PSF_G in the real domain. Moreover, Frey's model included the fan beam collimator geometry and took into account the enlargement of the holes due to the focalized geometry. However this model did not use the discrete nature of the hole array or the exact hole shape.

Another mathematical model proposed by Formiconi et al. [30] considered a discrete analysis for parallel and fan beam collimators, although the model did not take into account the elongation factor for the septa walls between the fan beam axis holes.

These reasons have led us to develop our own PSF models [65],[18] for parallel and fan beam collimators —see Figure 6.1— including detailed hexagonal holes and changes in the elongation of the hole as well as in the center-to-center hole distance. Both numerical ray tracing techniques (Pareto et al. [65]) and Monte Carlo simulation (Cot et al. [18]) provided sufficient information to build the new parallel and fan beam PSF_G and PSF_T for low-energy photons. As described in Chapters 4 and 5, the Total Point Spread Function (PSF_T) characterization needs Monte Carlo simulations to include all radiation-matter interactions. This procedure is more general than using ray-tracing or optical models which can only reproduce the geometrical component of the PSF, the PSF_G.

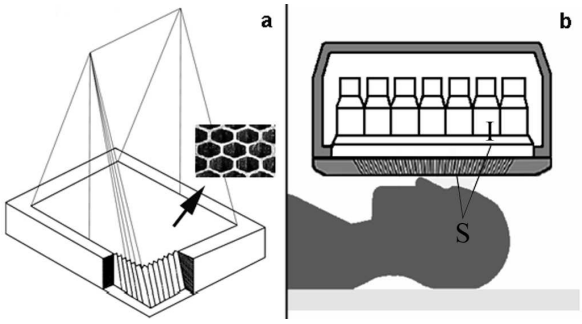

Fig. 6.1: *Figure a* shows the fan beam geometry used to model PSF_T. For each photon emitted at point **S** —see *Figure b*— there is a non-zero probability of being detected at point **I** in the back collimator plane —image plane—. This probability density function is based on the PSF_T .

Thus, the aim of this chapter is:

1. To summarize and to compare the different theoretical models for PSF characterization at low energies[1].

2. To use the most accurate Probability Density Function for parallel and fan beam collimator/detectors [2] in the Monte Carlo simulator.

3. To design and use a new Variance Reduction Technique in the SimSET code using our PSF_T.

[1] For high-energy photons, the Geometric component of the PSF (PSF_G) is not sufficient and only Total PSF_T PSF modelling obtained by Monte Carlo characterization is useful

[2] This work was restricted to MC simulations of low-energy photons. The PDF for high energy photons to pass the collimator/detector systemis under development using the PSF_T results of Chapter 5

6.2 Metz and Tsui PSF_G models

This section summarizes the theoretical basis of PSF_G functions proposed by Metz [56] and Tsui [83]. Although it includes the basic ideas for the development of PSF_G, the model includes a convolution of integrals in the frequency domain —for a detailed description, see Appendix D— which are not feasible methods in common applications.

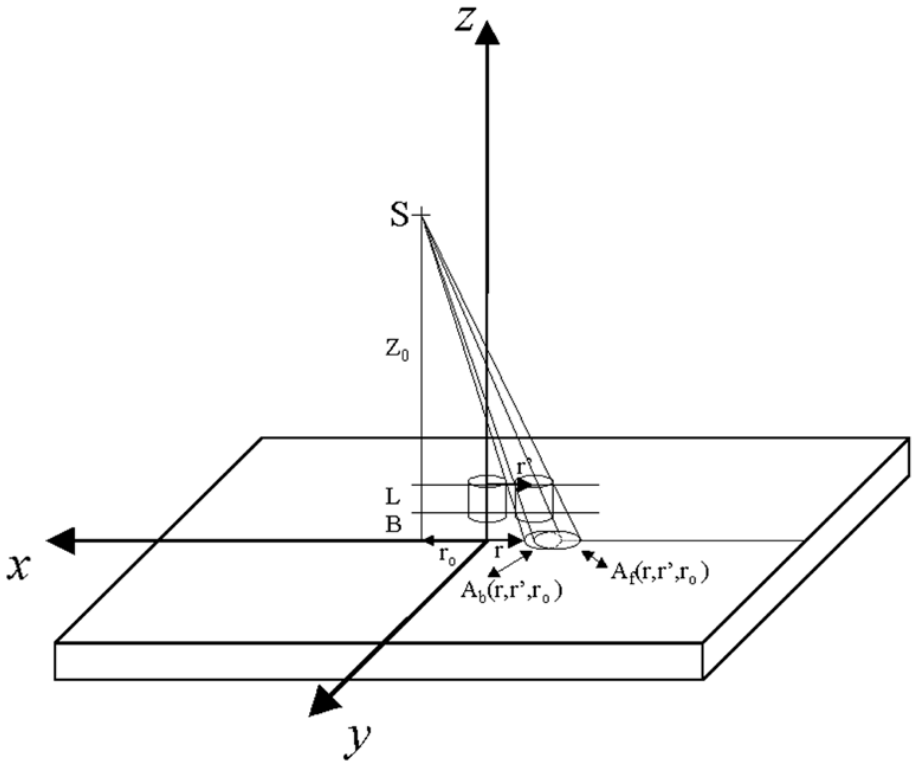

Fig. 6.2: A pair of tapered holes which are located in a parallel collimator. Geometry includes the overlapped area between the aperture functions described in Section D.1.1.

Consider a point source S located at a distance r_0 from the z-axis. The vector $\vec{r_0}$ determines the position of the orthogonal projection of the source onto the image plane. The source height from the front plane is Z. In order to obtain the PSF_G on the image plane, the projections of the point source through the front and back collimator planes are needed. Each aperture function depends on the vector $\vec{r}$ which represents the image point I seen by the source. As described above, the aperture function equals 1 when the source is seen from the image plane through the front plane. Otherwise, its value is set to 0. Similarly, another aperture function is defined for the back collimator plane. The

geometric transfer function models the intersection between both aperture functions on the image plane shown in Figure 6.2.

Let us define the fluency of photons ψ as the number of photons crossing a certain surface (detector) per unit time. In order to calculate the photon fluency, the sensitivity or efficiency η will also be defined as the number of photons reaching the detector plane per photon emitted. It is then obvious that:

$$\psi \;=\; \eta\; A(t) \tag{6.1}$$

where $A(t)$ is the activity of the photon emitter source[3] with dimension $[T^{-1}]$. Thus, the aim of PSF_G modelling is to obtain the efficiency $\eta(S)$ for a point activity source S for different collimator configurations.

The efficiency η at each point $\vec{r}$ is proportional to the integral over all the intersected aperture functions and **over the whole front plane collimator**. This integral has dimensions of surface $[L^2]$ because it is the sum over all the intersected areas:

$$\eta(\vec{r_i'}, \vec{\eta}, \vec{\varepsilon}) \;\propto\; \int\int a_f(\vec{\eta} - \vec{r_i'}) a_b(\vec{\varepsilon} - \vec{r_i'}) d^2\vec{r_i'} \tag{6.2}$$

In terms of the known variables $\vec{r}$ and $\vec{r_0}$; (6.2) can be written as:

$$\eta(\vec{r}, \vec{r_0}) \;\propto\; \int\int a_b(\vec{r}, \vec{r_i'}, \vec{r_0}) a_f(\vec{r}, \vec{r_i'}, \vec{r_0}) d^2\vec{r_i'} \tag{6.3}$$

The proportional constant k is the inverse square of the distance and the dot scalar product of the photon flux vector $\vec{IS}$ and the normal unit vector $\vec{n}$:

$$k \;= \frac{\vec{IS} * \vec{n}}{|\vec{IS}|} \frac{1}{4\pi|\vec{IS}|^2} \;=\; \frac{(x_0 - x_I, y_0 - y_I, L + B + Z)(0,0,1)}{4\pi|\vec{IS}|^3} \tag{6.4}$$

$$k \;= \frac{(L + B + Z)}{4\pi(|\vec{r_0} - \vec{r}|^2 + (L + B + Z)^2)^{\frac{3}{2}}} \tag{6.5}$$

Another formulation for the k factor includes the radiation intensity law which includes the inverse square distance ($R = |\vec{IS}|$ between point source S and image point I) and the scalar product between the photon direction and the normal plane vector, $\cos(\theta)$:

$$k \;=\; \frac{\cos(\theta)}{4\pi R^2} \tag{6.6}$$

[3] In this Chapter all the point sources emit isotropically

The sensitivity or efficiency η is equal to:

$$\eta(\vec{r},\vec{r_0}) \;=\; \frac{(L+B+Z)\int\int a_b(\vec{r},\vec{r_i'},\vec{r_0})a_f(\vec{r},\vec{r_i'},\vec{r_0})d^2\vec{r_i'}}{4\pi(|\vec{r_0}-\vec{r}|^2+(L+B+Z)^2)^{\frac{3}{2}}} \tag{6.7}$$

The efficiency may be interpreted as the integral of the probability density function for a point source to reach the detector:

$$\eta(\vec{r},\vec{r_0}) \;=\int_{\Delta_A} P(A)dA \tag{6.8}$$

where $P(A)$ is the probability density function per unit of area A. The number of counts in the detector bin N_A is directly the number of emitted photons (decays) Nc of the source multiplied by the integral of the density probability function over the detector area Δ_A, i.e. the sensitivity of the detector bin η_A:

$$N_A \;=\; Nc\;\eta_A(\vec{r},\vec{r_0}) \;=\; Nc\;\frac{(L+B+Z)\int_{\Delta_A}\int_{\Delta_A} a_b(\vec{r},\vec{r_i'},\vec{r_0})a_f(\vec{r},\vec{r_i'},\vec{r_0})d^2\vec{r_i'}}{4\pi(|\vec{r_0}-\vec{r}|^2+(L+B+Z)^2)^{\frac{3}{2}}} \tag{6.9}$$

The main problem of the frequency domain theory is the computation of the aperture functions at each source position. This model does not include the discrete nature of the hole array because the holes are considered as "mean open surfaces" seen from a source S. The result of the integral is equivalent to the average of the overlap of the aperture functions in the front plane collimator. The integral over all the front plane surface $d^2\vec{r_i'}$ when the hole aperture is moved for a fixed point source is equivalent to averaging the response spot over the image plane produced by point sources moving in a local plane $d^2\vec{r_0}$. Thus, an average PSF for the whole collimator field of view is obtained.

The method to obtain the aperture functions is presented in the Appendix D.

6.3 Frey's PSF_G model

Frey et al. [32] obtained the Geometrical component PSF_G. The average of the overlap of the area (mentioned in the last section 6.2) over the whole front plane collimator was replaced by a more detailed geometrical approach. The significant result was to obtain a PSF_G —for parallel and convergent collimators— in terms of a density probability function defined in the real domain:

$$P(\vec{r};\vec{r_0};A) \;=\; \frac{\text{Overlapped Area}}{\text{Collimator Cell Unit Area}} \;=\frac{2\arccos(\frac{\|\vec{r_0}\|}{2R})-2\frac{\|\vec{r_0}\|}{2R}\sqrt{1-\frac{\|\vec{r_0}\|^2}{4R^2}}}{2\sqrt{3}(R+S)^2} \tag{6.10}$$

where R is the hole radius, S is the septa wall and $\|\vec{r_0}\|$ is the modulus of the vector projected by the source onto the image plane.

The probability density is defined as an overlapped area —see Figure 6.2— per unit area: the hole unit cell area of the collimator. However in [32] there is no explanation nor demonstration of how the real domain function is obtained from the previous work of Tsui et al. [83]. In Appendix D the demonstration to develop this analytical model is described.

6.3.1 Hypothesis assumed in Frey's model

A summary of all the hypotheses assumed during the demonstration of the PSF_G (see Appendix D) are shown below:

1. The holes are considered to be circles instead of hexagons.

2. The image plane is considered as a virtual plane below the backplane collimator. The final image is performed inside the crystal layer. Modelling of the protective casing of aluminium, the NaI crystal itself and other backscattering layers (photomultipliers, ...) could only be simulated by Monte Carlo techniques [84], [19]

3. The probability density function is calculated in a discrete way. The basic discrete element is the hole unit cell area which is not infinitesimal, so the error in resolution is related to these dimensions.

4. Projection of the overlapped area consists of the junction of two ellipses, not circles. However, as $P(A)dA$ is finally the ratio between areas, both areas are affected by the same elongation factor so this effect may be compensated

6.3.2 Sensitivity condition

A basic condition for all the probability density functions (PDFs) is the conservation under variable changes (see Appendix D). That is, the total sensitivity of a point source emitter S is maintained constant over the whole field of view (A_{PSF}) for any model.

In the Metz model the global efficiency is:

$$\eta(S) \;=\; k \int_{\vec{r_i'}\in\ A_{PSF}} \int_{\vec{r_i'}\in\ A_{PSF}} a_b(\vec{r}, \vec{r_i'}, \vec{r_0}) a_f(\vec{r}, \vec{r_i'}, \vec{r_0}) d^2\vec{r_i'} \tag{6.11}$$

And this result is equal to the Frey model:

$$\eta(S) = \sum_{\gamma_r \in A_{PSF}} P(\vec{r}; \vec{r_0}; A) dA \tag{6.12}$$

The former model integrates the average aperture functions for any vector representing the hole center on the A_{PSF} area. The latter model solves the integral by means of Monte Carlo techniques, that is, it sorts each photon impact point γ_r over the A_{PSF} area and it assigns the corresponding probability density function to pass through the collimator.

However, other probability density functions may be used by using Monte Carlo techniques. This is the basis for improved PSF modelling including not only the geometric component but also the total PSF_T. Characterization of these functions is presented in the next section.

6.4 Pareto PSF_G model and Monte Carlo PSF_T validation

The ray-tracing method consists of determining the integral over the aperture functions by sampling "optical-rays". The transport of these rays only includes the geometrical approach without considering septal penetration, Rayleigh or Compton scattering. This is the reason for calling them "optical" methods.

Each detector bin is a discrete image plane. This plane is divided into N pixels of area Δ as shown in Figure **??**. Each pixel is sampled from its center to the source location through the collimator. The sampling covers all the detector surface and accumulates the "detected" number of optical rays ($A(\vec{r}, \vec{r_0}, Z+L+B)$). In Appendix D there is a detailed description of the ray-tracing method employed. The pixel area resolution Δ determines the accuracy of the sensitivity estimate η which is:

$$\eta = \sum_{\vec{r_i} \in \Delta_i} \frac{cos(\theta_i)}{4\pi R_i^2} A(\vec{r}, \vec{r_0}, Z + L + B)\ \Delta \tag{6.13}$$

R_i is the distance between the point source and each image point of the whole front plane collimator and the scalar product between each photon ray and the normal plane vector is $cos(\theta_i)$. If the last formula is rewritten using the same variables as the previous models of Frey and Tsui we obtain:

$$\eta(\vec{r}, \vec{r_0}) = \frac{(L + B + Z)}{4\pi(|\vec{r_0} - \vec{r}|^2 + (L + B + Z)^2)^{\frac{3}{2}}} A(\vec{r}, \vec{r_0}, Z + L + B)\ \Delta \tag{6.14}$$

Our Monte Carlo simulated results obtained for low-energy photons [18] (see Chapter 4), proved that the geometric component (PSF_G) constitutes 95% approximately of the total PSF (PSF_T) for both parallel and fan beam collimators without considering the

crystal detector[4]. Moreover, the main contribution of the septal penetration and scatter occurs in the same area as the geometric image with the result that the contribution of the tails to the total PSF is less than 1%. This is a key point in order to model the PSF_T for low energy photons. As reconstruction algorithms only work with relative values and the PSF_G always contributes the same percentage to the PSF_T, we will induce a model for the PSF_T using the numerical models obtained for the PSF_G. Moreover, a validation on resolution and sensitivity performed in the collimator only by Monte Carlo techniques provides sufficient validation for the numerical PSF model.

The PSF_T model may be split into the following parts:

1. For low-energy photons the geometric component PSF_G constitutes approximately 95% of the total PSF_T for both parallel and fan beam collimators. Modelling of the PSF_T may be carried out based on this geometric component.

2. The PSF_G can be fitted using a Gaussian distribution which can be modelled by its standard deviation (resolution) and its amplitude (sensitivity)

3. The sensitivity of a fan beam collimator system can be modelled as [51, 30]:

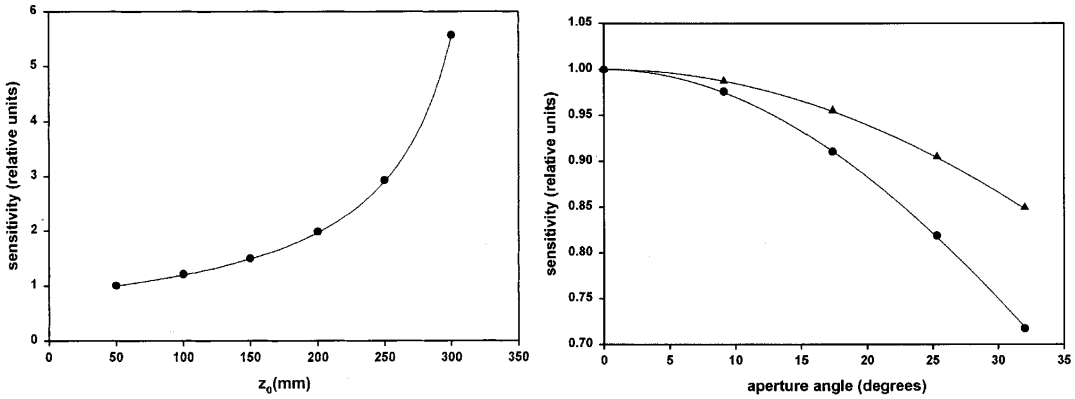

Fig. 6.3: On the left, sensitivity is plotted as a function of the z-coordinate (left) and of the x-coordinate (right) for a source point located on the z-axis. The solid lines correspond to the fitted function. Values are relative to the value obtained for a point source located at P (0; 0; 5) in cm.

$$\eta(\mathcal{Z}_{\mathcal{S}}, \cos\theta) = K\frac{F+L}{F-\mathcal{Z}_{\mathcal{S}}}\cos^2\theta \tag{6.15}$$

[4] The PSF_T model presented here may be directly used for reconstruction algorithms, whereas it only models the collimator step as a probability density function for Monte Carlo simulators. When a simulation is performed the PSF_T model is followed by a Monte Carlo simulation of each photon inside the detector crystal

4. Resolution is parameterized by the standard deviation which is modelled on the y-fan beam axis by,

$$\sigma_y(\mathcal{Z}_\mathcal{S}, \cos\theta) = \frac{a(\mathcal{Z}_\mathcal{S} + L + B)(2F + L)}{\sqrt{L^2(F - \mathcal{Z}_\mathcal{S})^2 - R^2(L + 2\mathcal{Z}_\mathcal{S})}} \frac{1}{\cos\theta} \tag{6.16}$$

and sigma on the parallel z-axis (which is similar to a parallel axis),

$$\sigma_z(\mathcal{Z}_\mathcal{S}, \cos\theta) = \frac{2aR(\mathcal{Z}_\mathcal{S} + L + B)}{L} \tag{6.17}$$

5. The parallel case is just the case of the fan beam collimator by considering $\lim_{F\to\infty}$

K is the efficiency factor which is determined by Monte Carlo simulations or experimental acquisition in order to obtain the real value because it depends on the intrinsic detector efficiency and it includes the other PSF_T components a part from the geometrical component. For reconstruction algorithms this value may be relative. F is the focal distance, L is the collimator length and Z_S is the height of the point source. The angle θ is the source aperture angle defined as the angle between the z-axis and the straight line passing through the point source and through the point in the focal line with the same y-coordinate as the point source. Angular dependence was studied to obtain the applicability conditions of each function, and $\cos(\theta)^2$ showed the best agreement according to [51] instead of $\cos(\theta)$ [30]. Notice that this method allows changes in the elongation of the hole to be included as well as in the center-to-center hole distance as a characteristic modelling for fan beam collimators.

The results of the ray-tracing method [65] for obtaining the geometric PSF in cast fan beam collimators with hexagonal holes have been presented in a complementary thesis [61]. These results were validated by experimental acquisitions and by Monte Carlo simulations with the same collimator/detector configuration (see Chapter 4).

6.5 Acceleration of SimSET

As indicated in the introduction, modelling of the PSF may be used as a Probability Density Function in the Monte Carlo simulator in order to avoid detailed tracking inside the complex collimator geometry. In this Section 6.5 a new PDF for SimSET based on our PSF modelling is described. The simulation CPU time obtained with the modified SimSET code presents a higher speed-up factor.

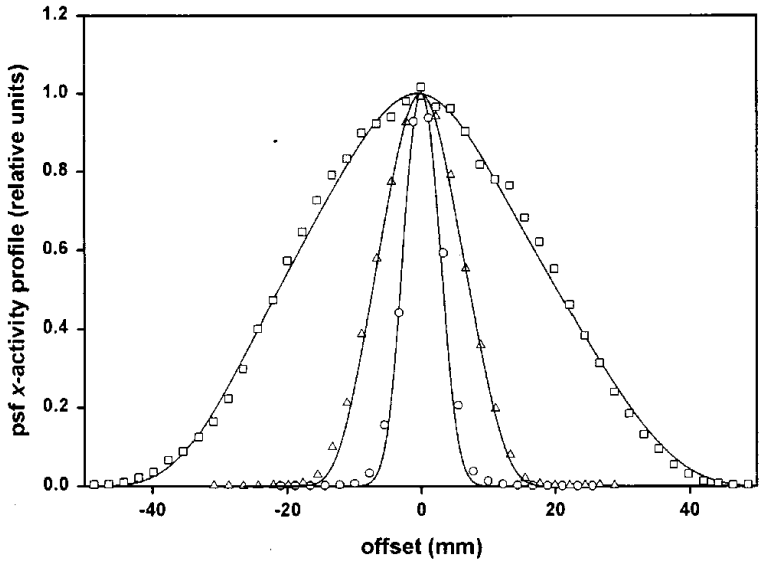

Fig. 6.4: Profiles in fan beam direction obtained from collapsed simulated (solid line) and experimental PSFs (symbols) for source points located on (a) z axis at P (0; 0; 50) (circles), P (0; 0; 150) (triangles), P (0; 0; 250) (squares) and (b) outside z axis at P (-160; 0; 50) (circles), P (-120; 0; 150) (triangles), P (-40; 0; 250) (squares) from right to left, respectively. A value of 1 has been assigned to the maximum of each profile in the two graphs.

6.5.1 SimSET original Probability Density Function

The Collimator Module originally used in SimSET [36] received photons from the PHG module and it tracked them through the collimator being modelled. The PDF used was based on the PSF_G from Frey model [32] described in Section 6.3 with the corresponding hypotheses. Parallel, fan, and cone beam collimator configurations were included in the model.

In Monte Carlo simulations, the collimator transfer function has to be used in terms of the probability density of the photon passing with a defined location and direction. When tracking photons inside the object, each photon has an initial weight w_0 (see Chapter 3). Afterwards, a weight w is assigned to the photon according to the interactions suffered in the object. The weighted photon $w_i = w_0 w$ has a defined origin point, direction cosines and track-length. Thus, the Frey model is suitable for describing the PDF per unit area $P(A)dA$ of a photon passing through a certain area of the collimator with a known relative position and direction.

The collimator/detector head rotates around the object in each SPECT study. Therefore, a photon travelling in a defined direction will have a determined probability $P_{collimator}(\Theta)$ to hit the collimator at that angle position Θ of the camera head. This probability is inversely proportional to the number of views N_{view} (see chapter 3), as the length of each projection $T_{projection}$ is constant over the length of scan T_{scan}:

$$T_{projection} = \frac{T_{scan}}{N_{view}} \tag{6.18}$$

Thus, when the photon hits the collimator with a certain direction Θ, the probability of the collimator being in such position is equal to:

$$P_{collimator}(\Theta) = \frac{T_{projection}}{T_{scan}} = \frac{1}{N_{view}} \tag{6.19}$$

Use of the Frey probability model in SimSET follows the sequence :

1. The initial photon is sorted with its direction and initial weight[5] w_0 from the point source S

$$W = w_0 \tag{6.20}$$

2. The photon is tracked through the object and the corresponding weight w is calculated:

[5] W is the final or cumulative weight of the photon at the end of tracking

$$W = w_0\ w \tag{6.21}$$

3. The probabilities of passing through all the possible collimator views Θ_i are computed using a collimator PDF. This operation is performed for each photon leaving the object and each probability $P(\vec{r}; \vec{r_0}; A_i)$ is determined for all the bin detectors A_i located in each collimator angle Θ_i. Therefore, the final weight W_i is calculated as:

$$W_i = w_0\ w\ P(\vec{r}; \vec{r_0}; A_i) \tag{6.22}$$

4. The probability of interacting with each view Θ_i of the detector system —$P_{collimator}(\Theta_i)$— is determined and included in the global weight:

$$W_i = w_0\ w\ P(\vec{r}; \vec{r_0}; A_i) dA_i\ P_{collimator}(\Theta_i) \tag{6.23}$$

5. A specific angle for detection is selected from the possibilities by a random process:

$$\{R\}_{R=1..N_{view}} \tag{6.24}$$

and the original SimSET code only bins a single detector position for each photon. The final weight of the accepted photon in the weight image is:

$$W_R = \frac{w_0\ w\ P(\vec{r}; \vec{r_0}; A_R) dA_R}{N_{view}} \tag{6.25}$$

This procedure loses computational efficiency because many of the possible detector angles Θ_i are discarded. The SimSET author thought the azimuthal angle dimension would be over sampled relative to any other dimension. This idea relies on the characterization of the PDF per unit area instead of per unit solid angle

6.5.2 A new Probability Density Function

The new PDF will not over-sample the angle dimension because it depends on the photon direction and it is defined per unit solid angle. We do not need to sort the Θ magnitude because the PDF maintains an isotropic approach in the range of neighborouring collimator angles[6]. The new PDF will improve the accuracy of the model and it will accelerate the process of detection by using all the views available to each photon. Two acceleration factors will be introduced in the new model in order to decrease the sum of square weights:

[6] We assume an isotropic probability on the exit direction when a photon scatters. We base this assumption on the low number of available collimator positions for that photon direction.

1. It allows us to select the most probable collimator Θ angle position or view without the need to discard it in the random process

2. The detected photon can be accumulated simultaneously at different collimator heads at different angles Θ_i. All the probable collimator views are included in the result and the photon is split into many weights in different collimator views and bins. Table 6.5.2 shows the number of views available for a certain photon with this new model using common collimator configurations:

Variable	Case1	Case 2	Case 3
R(cm)	20	10	10
Number of Projections	60	60	120
Δ_x (cm)	2.1	1.1	0.525
σ_i (cm)	0.17	0.17	0.17
σ_z (cm)	0.22 to 0.55	0.22 to 0.55	0.22 to 0.55
σ_y (cm)	0.25 to 3.7	0.25 to 3.7	0.25 to 3.7
N°views (Parallel)	1	1	3
N°views (Fan beam)	2	3	4

Tab. 6.1: The number of views available for a certain photon direction with the new PDF. R is the radius of rotation of the collimator/detector heads, the number of projections is N_{view}, Δ_x is the pixel detector size, σ_i is the intrinsic detector resolution and σ_y and σ_z are the fan beam and parallel axis resolutions respectively

The new PDF used in SimSET uses the following procedure:

1. The sensitivity of a fan beam collimator system is obtained as:

$$\eta(\mathcal{Z}_\mathcal{S}, \cos\theta) = K\frac{F+L}{F-\mathcal{Z}_\mathcal{S}}\cos^2\theta \tag{6.26}$$

2. The resolution is a Gaussian distribution modelled by its standard deviation:

$$\sigma_y = \frac{a(\mathcal{Z}_\mathcal{S}+L+B)(2F+L)}{\sqrt{L^2(F-\mathcal{Z}_\mathcal{S})^2 - R^2(L+2\mathcal{Z}_\mathcal{S})}}\frac{1}{\cos\theta} \tag{6.27}$$

and its sigma on the z-axis of the fan beam (which is similar to a parallel),

$$\sigma_z = \frac{2aR(\mathcal{Z}_\mathcal{S}+L+B)}{L} \tag{6.28}$$

3. The Gaussian PDF of the source S is centered at the impact point I_{FS} (juncture of the line between S -point source emission- and F -focal point closest to S in the focal line- and the backplane collimator), as shown in the Figure below. The center of the new reference system is $(\mathcal{X}_{bin}, \mathcal{Y}_{bin})$.

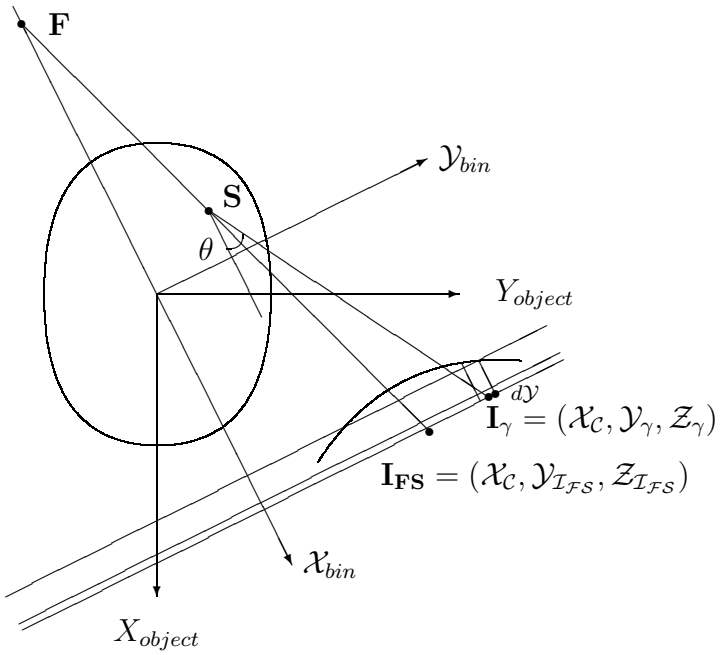

4. Once the Gaussian point spread function is calculated for a certain angle position Θ of the collimator, the volume intersected under the Gaussian over the bin detector area hit by the photon at I_γ is calculated:

$$\kappa = \frac{\eta(\mathcal{Z}_\mathcal{S}, \cos\theta)}{2.0\pi\sigma_z\sigma_y} \tag{6.29}$$

$$\int_z PSF(y,z)dz = \int_{-\frac{\Delta_z}{2}}^{+\frac{\Delta_z}{2}} \exp^{-\frac{((\mathcal{Z}_\gamma - z) - \mathcal{Z}_{\mathcal{I}_{\mathcal{FS}}})^2}{2\sigma_z^2}} dz \tag{6.30}$$

$$\int_y PSF(y,z)dy = \int_{-\frac{\Delta_y}{2}}^{+\frac{\Delta_y}{2}} \exp^{-\frac{((\mathcal{Y}_\gamma - y) - \mathcal{Y}_{\mathcal{I}_{\mathcal{FS}}})^2}{2\sigma_y^2}} dy \tag{6.31}$$

$$\Delta\Omega = \frac{\Delta_z\Delta_y}{4\pi|\vec{SI}_\gamma|^2}\cos(\theta) = \frac{\Delta_z\Delta_y\mathcal{X}_\mathcal{S}}{4\pi|\vec{SI}_\gamma|^3} \tag{6.32}$$

where the new density probability function is:

$$P(\vec{r};\vec{r_0};\Omega_i)d\Omega_i = \frac{\kappa \int_y \int_z PSF(y,z)dydz}{\Delta\Omega} \tag{6.33}$$

The bin detector area $\Delta_z\Delta_y$ is a user-defined variable. The smaller the area, the better the accuracy of the probability density function estimate. This new PDF adjusts the photon weight at each Θ angle.

5. Finally the probability of interacting with each view of the detector system $P_{collimator}(\Theta)$ is calculated independently because it has been normalized per unit solid angle:

$$W_i = w_0\ w\ P(\vec{r};\vec{r_0};\Omega_i)d\Omega_i\ P_{collimator}(\Theta) \tag{6.34}$$

6. This procedure ensures that a single photon history may contribute to different collimator bins situated at different Θ_i angles in the simulation. A new variance reduction technique has been used in SimSET. More photon histories are binned as detected events with a reduced weight value at each angle

6.6 Results

6.6.1 Comparison between Frey PSF_G and our PSF_T models

The comparison between the two models used in SimSET is shown in Figure 6.5. The simulations were performed using the SimSET code, with the PSF_G of Frey's model and the new PDF based on our PSF_T[7] The comparison was done using point sources in air with the following characteristics:

1. The PSFs compared are those obtained for different 140 keV point sources located on the central axis of a fan beam collimator with a focal length of 35.5 cm, hole length of 4.0 cm, hole septa of 0.02 cm

2. The hole radii used in the Frey model ($R_h = 0.07875cm$) correspond to round holes with an equivalent area to hexagonal holes used in our model ($R_h = 0.0866cm$)

3. Both models include the crystal effect, that is, the reduction of sensitivity due to the attenuation of photons through the detector material. In the PSF_G model, the MC simulation of the detector was performed. In the second model, experimental sensitivity acquisition without the collimator was carried out in order to determine

[7] The SimSET modules changed in the new accelerated SimSET were UncCollimator.c, Collimator.c, PhgParams.c, PhgParams.h and EmisList.c.

the absolute efficiency of the sodium iodide detector ($\eta_{NaI} = 67.5\%$). This efficiency was taken into account in the PSF_T model in order to compare the results. The numerical ray tracing method was also affected by the crystal efficiency.

4. The PSF_T model considers a normalization constant of the PSF at $z = 5$ cm. This value corresponds to 8.1277×10^{-5}, that is, the sensitivity of the fan beam collimator without the crystal effect.

The results of different PSF simulated for point sources located on the central axis are shown in Figure 6.5.

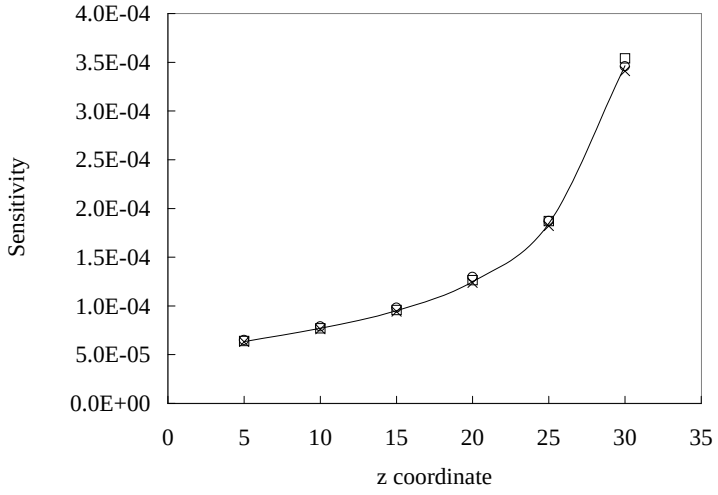

Fig. 6.5: The different sensitivity values are represented. Experimental (circles), ray tracing (squares), the PSF_G Frey model (crosses) and the PSF_T model (solid line).

The results show good agreement for central axis positions. However, some differences appear at off-axis locations. In this part of the FOV, the model of Frey et al. presents some differences due to the limitations of the geometrical hypotheses assumed. Table 6.6.1 shows these divergences compared with the experimental values.

6.6.2 Comparison between the original and the accelerated SimSET

A neuroreceptor study was simulated in order to validate the new PSF_T. Both PSFs models were employed in the simulation: the original PSF_G used in the Standard SimSET (phg) and our new PSF_T model for the PDF used in the accelerated SimSET (phg_{cot}).

Three different Variance Reduction Techniques were used : Analogue Monte Carlo, Importance Sampling at 90º and Importance Sampling at 5º. Three different noise levels

	(5,16)	(10,16)	(15,12)	(20,8)	(25,4)	(30,2)
Experiment	5.09E-05	5.54E-05	6.92E-05	1.03E-04	1.58E-04	3.21E-04
Ray tracing PSF_G model	4.98E-05	5.50E-05	7.14E-05	9.95E-05	1.64E-04	3.15E-04
Relative difference	-2%	-1%	3%	-3%	4%	-2%
Frey's PSF_G model	4.49E-05	4.75E-05	6.32E-05	8.90E-05	1.51E-04	2.91E-04
Relative difference	-13%	-16%	-9%	-15%	-4%	-10%
PSF_T model	5.02E-05	5.52E-05	7.06E-05	9.82E-05	1.61E-04	3.08E-04
Relative difference	-1%	0%	2%	-4%	2%	-4%

Tab. 6.2: Comparison of different PSF results between the PSF_G and PSF_T used in SimSET. Source positions are described as (x, y).

were simulated with a number of counts equal to 1, 3 and 5 million counts. The number of histories and the length of the scan (42.9 s, 128.7 s and 214.4 s) were adjusted in order to obtain $\sum w = \sum w^2$ (i.e. real noise).

Table 6.3 indicates that the new accelerated SimSET PDF allows a speed-up factor of 2 with respect to the original SimSET and a factor of 7 with respect to the Analogue MC. The Quality Factor (QF) obtained with the new PDF under the same conditions is smaller. The reason is that the higher number of accepted photons with a minor weight value, and thus have a smaller square weight. The higher amount of accepted photons enables the number of counts with a "real" level of noise in a shorter CPU time to be reached.

As the number of projections increases (i.e. 120 instead of 60), the speed-up factor also increases as described in Table 6.6.

Another interesting result obtained refers to the small difference in sensitivity results between PSF_T and PSF_G as shown in Figure 6.7. This difference may be explained by the small divergences of the two models in PSF sensitivities at off-axis source positions in the fan beam collimator. When both PSFs are used the initial differences are converted in relative divergences up to 5% in the sum of weights, showing the importance of correct PSF modelling.

Thus, for simulations of neuroreceptor studies, the PSF_T model should be used with the VRT corresponding to Importance Sampling a 5º.

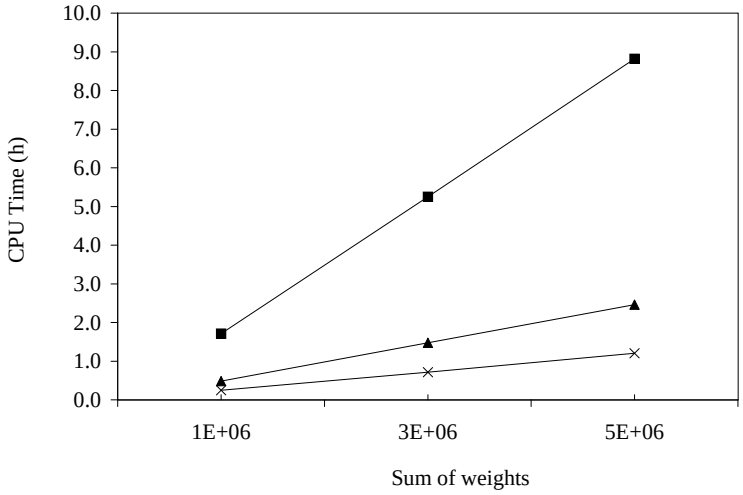

Fig. 6.6: The computation CPU time taken by each simulation type: Analogue MC (squares), PSF_G Frey model (triangles) and PSF_T model (Crosses). The CPU time is proportional to the number of weights obtained.

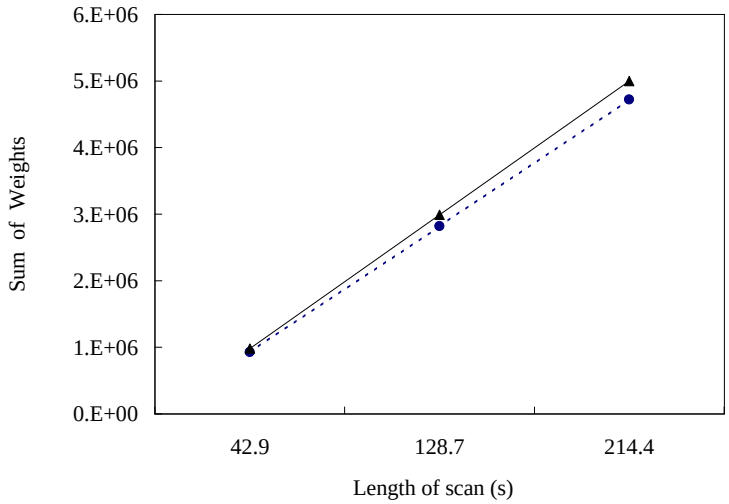

Fig. 6.7: The sum of weights obtained with the same length of scan and number of histories using the PSF_G Frey model (triangles and solid line) and PSF_T model (circles and dashed line)

	Analogue MC		Importance Sampling 5°	
	PSF_G Frey	PSF_T	PSF_G Frey	PSF_T
	$\sum w$ = 1 Million			
CPU Time (h)	1.71	0.79	0.48	0.25
Accepted photons	1.51e6	2.65e6	2.09e6	3.81e6
$\sum w$	9.81e5	9.24e5	9.82e5	9.27e5
$\sum w^2$	9.78e5	9.78e5	1.00e6	9.45e5
QF	0.65	0.33	0.458	0.239
	$\sum w$ = 3 Million			
CPU Time (h)	5.25	24.06	1.48	0.71
Accepted photons	4.61e6	8.09e6	6.50e6	11.2e6
$\sum w$	2.99e6	2.82e6	2.99e6	2.82e6
$\sum w^2$	2.98e6	2.98e6	3.01e6	3.02e6
QF	0.65	0.33	0.458	0.235
	$\sum w$ = 5 Million			
CPU Time (h)	8.82	3.84	2.46	1.20
Accepted photons	7.69e6	13.48e6	10.89e6	18.90e6
$\sum w$	5.00e6	4.71e6	5.00e6	4.72e6
$\sum w^2$	5.00e6	5.00e6	5.01e6	5.00e6
QF	0.65	0.33	0.458	0.236

Tab. 6.3: Comparison of different parameters between the PSF_G and PSF_T used in SimSET.

7. ABSOLUTE QUANTIFICATION IN SPECT

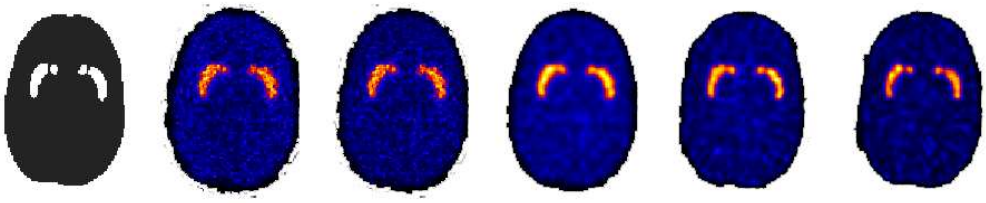

"The knowledge of our mind evolutes with the aid of computers"

7.1 Introduction

Following advances in molecular imaging, neurotransmission SPECT has become an important field in neuroimaging and is today regarded as a useful method in both clinical [80, 68] and basic research [1]. The dopamine transporter (DAT) has been shown to be a sensitive indicator of nigrostriatal dopamine function. Dysfunctions of the presynaptic dopaminergic system are involved in Parkinson Disease (PD) and, as a consequence, DAT imaging is a useful tool to confirm or exclude PD [80]. A number of cocaine analog SPECT agents, which bind to DAT sites, have been developed. These analogues include ^{123}I agents, such as the recently, available FP-CIT, and ^{99m}Tc agents such as TRODAT.

Although visual inspection is often sufficient to assess DAT imaging, quantification could improve the diagnosis accuracy of SPECT studies of the dopaminergic system. The quantification is focused on obtaining the striatal/background uptake ratio (See Figure 7.3). Quantitative accuracy in SPECT is impaired by a number of factors including noise, attenuation, scatter and collimator/detector response. All these factors degrade sensitivity and resolution of SPECT images as described in Chapter 2. Correction for these effects has been a research topic in nuclear medicine for the past two decades.

We analyzed the contribution of each correction in the quantification results for neurotransmission SPECT studies by using 2D reconstruction [63]. These results revealed that the different degrading effects affect the quantification results significantly. In particular, the scattering effect in the object and in the collimator/detector system is important. Nevertheless, collimator/detector scattering has to be taken into account when high-energy

rays like those of ^{123}I agents are imaged[1]. Thus, the scattering models should focus on scatter interactions in the object for brain neurotransmission studies like those performed with ^{99m}Tc–TRODAT [18]. The different strategies employed to make the burdensome scatter correction techniques computationally feasible are described.

The aim of the present study was the assessment of the absolute and relative quantification results for neurotransmision SPECT studies using an improved reconstruction algorithm including scatter correction. Furthermore, we designed the Scattering Monte Carlo Feedback Correction (SMFC) method as a computationally efficient full 3D reconstruction architecture with a Monte Carlo-based scatter estimation. This algorithm included a full 3D reconstruction, instead of a 2D reconstruction, with correction of attenuation, scatter and spatially variant fan beam collimator response in ^{99m}Tc-TRODAT studies.

7.2 Material and Methods

7.2.1 Full 3D reconstruction algorithm

In order to include the photon crosstalk effect between transaxial slices (along the tomographic axis), the full 3D tree-dimensional reconstruction is required. In contrast to 2D (slice-by-slice) reconstruction, full 3D uses a large matrix which enables photons that are detected in out-of-slice projection pixels to be taken into account. This further improves the accuracy of the reconstructions, albeit at the cost of a relatively high computational burden. In addition to providing improved quantitative accuracy, full 3D iterative reconstruction with accurate PSF modelling in both axes of the detector head may result in significant improvement of quantification results compared with 2D reconstruction [88, 82].

The goal of the new P3D-OSEM was to use a new 3D physical model for iterative reconstruction in SPECT and to validate it by using Monte Carlo techniques. We based our P3D-OSEM reconstruction algorithm using iterative methods. The P3D-OSEM was an upgraded version of the 2D algorithm presented by Falcon [27] which was based on the iterative Ordered Subsets Expectation Maximization (OS-EM) algorithm of Hudson and Larkin [39].

In the P3D-OSEM algorithm, each factor is a well understood physical phenomenon, and therefore corrections are included for each of the image degrading effects (See Appendix E for a detailed description). The factors are calculated separately and multiplied afterwards. The result is stored using compact design techniques thus avoiding the increase of matrix size [14]. The standard 3D transition matrix dimension equals the number

[1] As explained in Chapter 5, the collimator/detector scattering depends on the energy of the radiotracer. Correction for the collimator/detector scattering contamination is not presented in this thesis but it is under development.

of voxels multiplied by the number of detector angles and by the number of projection bins containing non-zero values of the response model. To avoid surpassing the maximum RAM memory available, the total transition matrix is split in as many submatrices (P3D-OSEM) as the number of ordered subsets.

Each P3D-OSEM submatrix includes all the object contributions to each subset of projections. At each iteration step, the corresponding submatrix is loaded, the subset of projections is reconstructed and finally it is unloaded. Although reading the submatrix at each subset is time-consuming, this strategy is a trade-off between RAM memory capacities and processing times. The amount of memory is reduced linearly with the number of subsets.

7.2.2 Scatter Monte Carlo-based correction

The scatter effect in the final image is about 15% to 40% of the total image, thus it has to be corrected in order to obtain quantification results. Nowadays this subject is an intensive field of research in SPECT techniques [57, 16]. Scattering phenomena in the object and in the collimator/detector system affects the quantification results in neurotransmission SPECT studies significantly [63]. The scattering in the collimator produced by low energy photons of ^{99m}Tc-TRODAT agents may be neglected [18]. Thus, the scattering models should focus on scatter interactions in the object for ^{99m}Tc-TRODAT brain neurotransmission studies. There are different approaches to the modelling of scattering but its stochastic behavior difficult its modelling (See Appendix E for a detailed description).

Monte Carlo simulation (MC) is the most general method for detailed modelling of scattering although it implies long computation times. We modelled the scattering effect by simulating the reconstructed image of the full P3D-OSEM algorithm with the SimSET (see Chapter 6) virtual phantom Monte Carlo simulator. The reconstructed image is the input object for the modified SimSET forward projector in order to estimate the scattering distribution. The stochastic photon transport simulation ensures the completeness of all the interaction and detection effects during the photon tracking from emission to detection. The MC simulation is a useful tool in order to determine the fraction of scattered events at each detector bin both in the object and the collimator/detector system.

7.2.3 Absolute Quantification in SPECT: the SMFC method

The Scatter Monte Carlo Feedback Correction (SMFC) is a method that we have developed which combines the P3D-OSEM reconstruction algorithm with Monte Carlo scattering correction. The SMFC also enabales an absolute activity value at each voxel of the image to be determined using a normalization procedure in the full 3D reconstruction. The absolute volumetric activities in each voxel of the object were obtained in $\frac{\mu Ci}{cm^3}$ units.

The scattering is corrected from the original projections. This operation may be repeated in the so-called feedback process. The process of forward projection, comparison and updating can be iterated until an acceptable image is obtained. The Monte Carlo simulation of forward projection includes all the image degrading effect, that is, the modelling of attenuation, collimator blurring, scattering and noise equivalent counting on the projections. The scattering estimate in the projection data is compared with theoretical values and the accuracy assessment of the quantitative image parameters such as recovery ratio, mean values and signal-to-noise ratio were compared with the 2D reconstructed image without scattering correction.

7.2.4 Validation of the SMFC method

The method was tested using simulated projections of the striatal virtual phantom. The simulations considered a gamma-camera with a fan beam collimator. The reconstructed image was evaluated by using a 3D volume evaluation procedure instead of the 2D slice-by-slice evaluation.

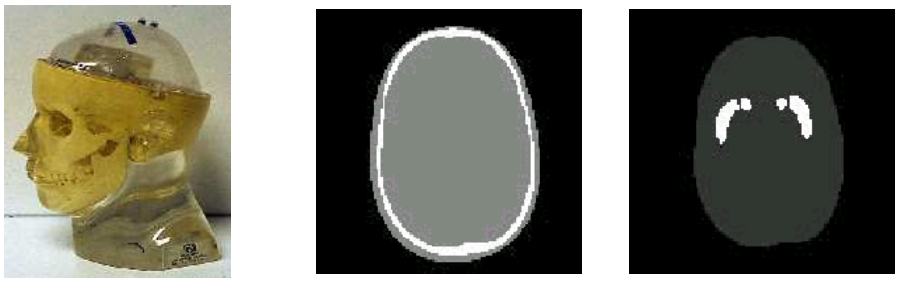

(A) (B) (C)

Fig. 7.1: Striatal virtual phantom for neuroreceptor SPECT studies. The experimental phantom is shown in -A- whereas the virtual phantom with its corresponding attenuation -B- and activity -C- maps for a central slice.

The SimSET Monte Carlo code simulated the non-pathologic conditions of a neurotransmission study: a ratio between specific uptake (basal ganglia) to non-specific uptake (occipital region) equal to 70/10 as shown in Figures 7.3 and 7.2. Primary and scattered low energy photons were collected separately, and 3,5 Mc were obtained over 120 projections with 128 bins (bin size=0.4424cm). Twelve slices (0.5 cm in width) containing the basal ganglia were reconstructed. Reconstruction was performed using the P3D-OSEM algorithm with 15 subsets[2] with compensation for attenuation and and distance-dependent collimator response PSF_T.

[2] The total transition matrix was split into 15 submatrices (P3D-OSEM) of 0.25 Gb in order to use the minimum RAM memory available, i.e. 2Gb.

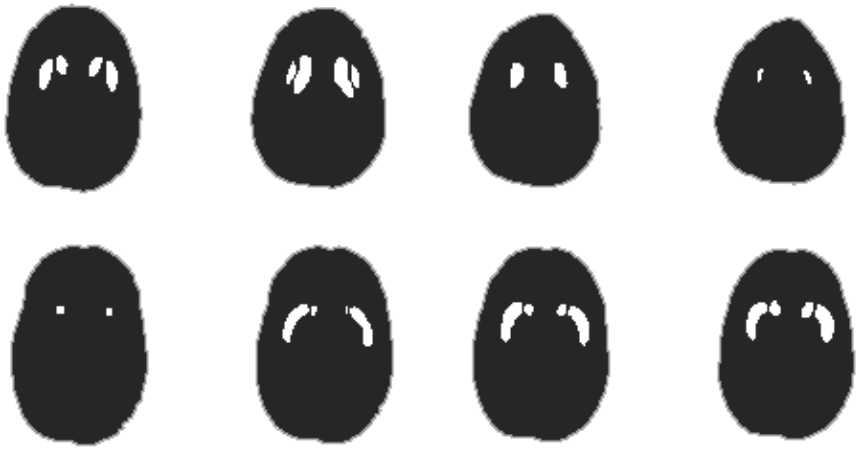

Fig. 7.2: Activity map corresponding to the striatal virtual phantom. The virtual phantom consists of 8 slices activated with 70 $\mu Ci/cm^3$ of 140 keV photons (white ganglia) and 10 $\mu Ci/cm^3$ on the background (non-specific region in grey).

An analysis of results depending on the number of iterations (n from 1 to 32) of the reconstruction process is presented. Five projection sets for low energy photons (140 keV) were simulated by using the SimSET Monte Carlo code. The quantification of the striatal to non-specific uptake ratio was carried out by using a 3D evaluation. Each volume of interest (see Figure 7.3 was analyzed including the slices above and below the slice of interest (see Figure 7.5).

7.3 Results

7.3.1 P3D-OSEM reconstructed images

The P3D-OSEM reconstruction results may be compared with the corresponding recovery ratios[3] (RR) of 2D reconstruction algorithms and 3D slice-by-slice evaluation. Table 7.1 shows the different recovery ratios depending on the corrections useed in the reconstruction algorithm:

The different reconstructed images with the evolutive reconstruction algorithms are shown in Figure 7.4:

[3] The recovery ratio is defined as the ratio between the specific and the non-specific uptake values at each region of interest compared with the theoretical value. Thus, the theoretical recovery value of this neurotransmission study is 7.

Fig. 7.3: Regions of interest (ROI) corresponding to the striatal virtual phantom. The virtual phantom consists of 8 slices containing the basal ganglia. The basal ganglia include the left caudate C_{left} (blue), the left putamen P_{left} (red), the right caudate C_{right} (orange) and the right putamen P_{right} (yellow). The background (non-specific region) corresponding to the occipital region is in grey.

Recovery ratios	RRC_{left}	RRP_{left}	RRC_{right}	RRP_{right}
3D att PSF prim+scat	91%	89%	89%	89%
2D att PSF prim+scat	77%	80%	76%	80%
2D att nPSF prim+scat	70%	73%	69%	72%
2D natt nPSF prim+scat	62%	68%	60%	65%
2D FBP prim+scat	61%	65%	61%	63%

Tab. 7.1: Different recovery ratios corresponding to primary and low energy scattered photons depending on the reconstruction algorithm. The corrections considered were attenuation (att) and PSF. The reconstruction algorithms 2D and Filtered Backprojection (FBP) were evaluated in a 2D slice-by-slice procedure whereas 3D algorithms included a 3D evaluation. Both 2D and 3D algorithms used 32 iterations.

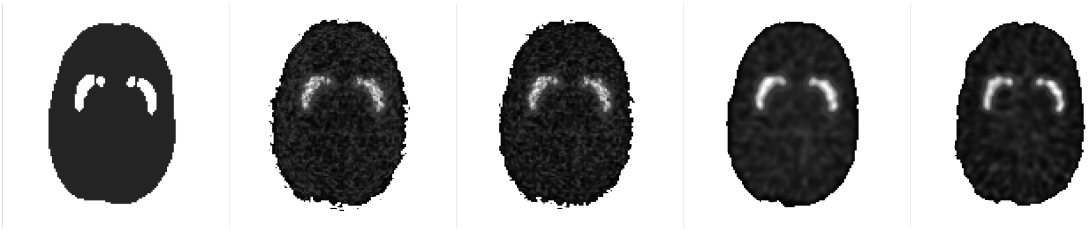

Fig. 7.4: From left to right: the theoretical activity image, a 2D reconstructed image without corrections, a 2D image with attenuation correction, 2D image with attenuation and PSF corrections and 3D image with attenuation and PSF corrections.

The reconstructed images using the P3D-OSEM algorithm at the 4th iteration are shown in Figure 7.5.

7.3.2 The MC scattering estimate

The scattering distribution estimate is shown in Figure 7.6. The total number of detected photons which have been scattered is represented for different number of iterations during the reconstruction step. Thus, different reconstructed images (at different level of iterations) were the corresponding inputs for each simulations.

The t-test comparison between original scattering image and the estimated scattering image obtained depending the number of iterations of the reconstructed image is shown in Table 7.3.2:

N° iterations	1	4	16	32
$\leq 1\sigma$	63,70%	63,04%	62,65%	63,34%
$\leq 2\sigma$	98,59%	98,37%	98,37%	98,49%
$\leq 3\sigma$	99,65%	99,71%	99,73%	99,71%

Simulation results showed good agreement between the original scattering distribution and the estimated by this method as Figure 7.7 shows.

The proposed methodology is expected to be useful for obtaining highly accurate scattering distributions in SPECT projections within lower computation times.

The images shown in Figure 7.8 correspond to the differences between the scattering corrected and uncorrected 3D reconstructions:

The full 3D reconstruction with Monte Carlo-based scattering correction of the virtual phantom (SMFC method) is shown in Figure 7.9.

Fig. 7.5: 3D reconstructed image corresponding to the striatal virtual phantom. The reconstructed image corresponds to the 4th iteration of the P3D-OSEM algorithm.

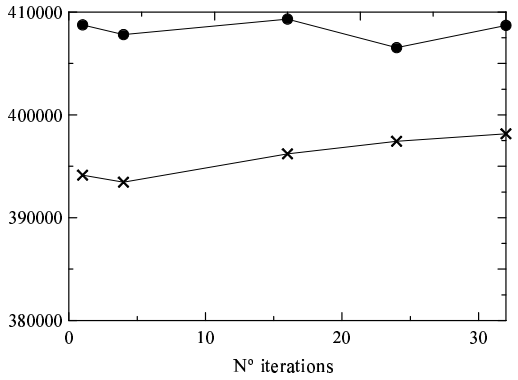

Fig. 7.6: Original number of scattering counts (squares) obtained from initial simulation of Alderson numerical phantom are compared with the the estimated number of scattering counts after simulating the reconstructed image (crosses).

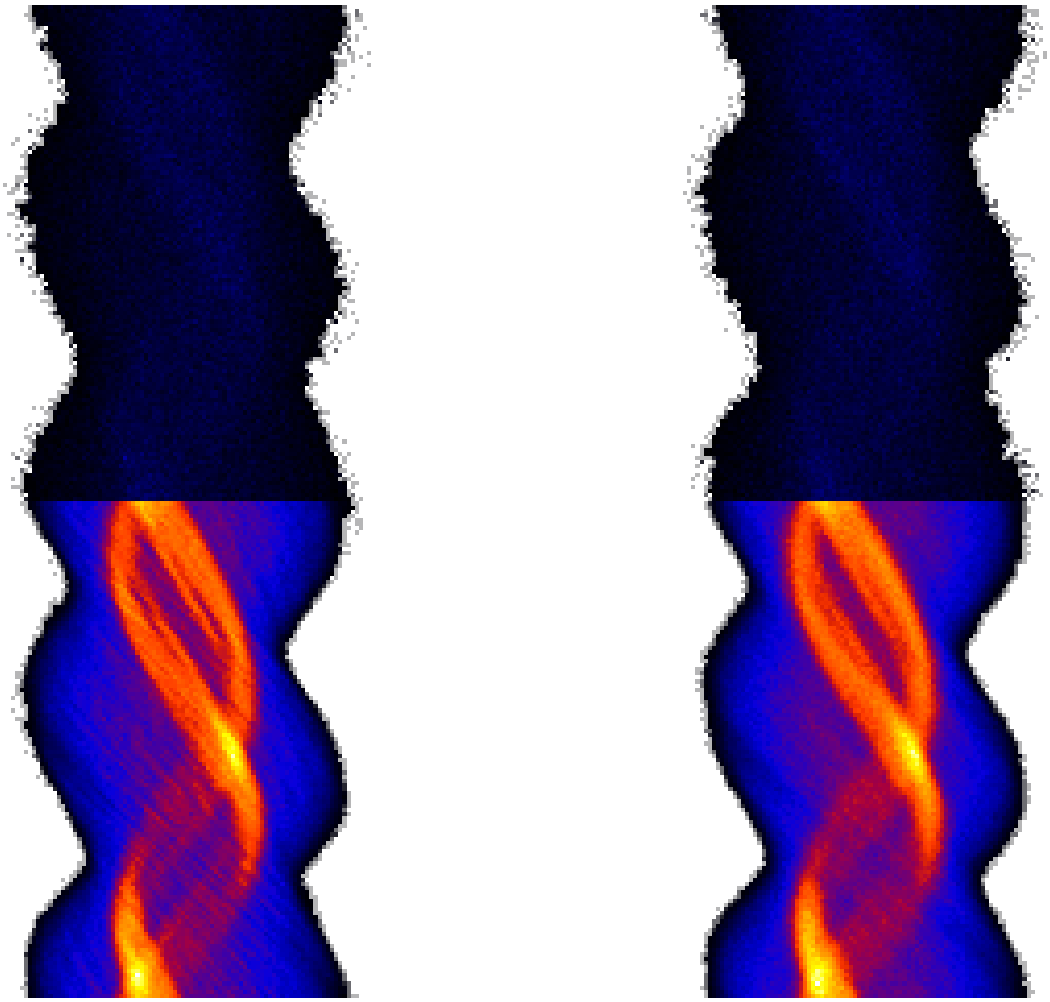

Fig. 7.7: Comparison between real noise projections —left— and estimated noise free projections —right—.

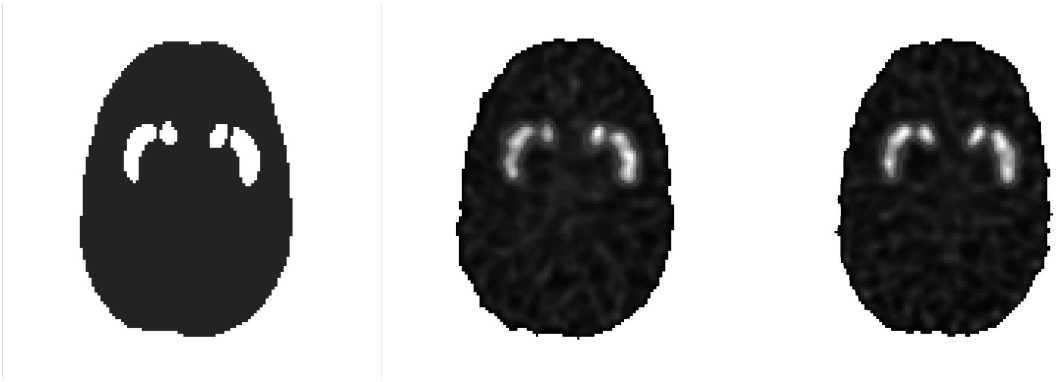

Fig. 7.8: From left to right: the theoretical activity image, the full 3D reconstructed image with corrections of attenuation and PSF, the full 3D image with attenuation, PSF and scattering correction using the SMFC method.

Fig. 7.9: 3D reconstructed image after scattering correction. The SMFC was applied to the whole striatal virtual phantom. The reconstructed image corresponds to the 4th iteration of the P3D–OSEM algorithm.

Recovery ratios	RRC_{left}	RRP_{left}	RRC_{right}	RRP_{right}
3D att PSF scat correction	97%	95%	95%	95%
3D att PSF prim+scat	90%	89%	89%	89%
2D att PSF prim+scat	77%	80%	76%	80%
2D att nPSF prim+scat	70%	73%	69%	72%
2D natt nPSF prim+scat	62%	68%	60%	65%
2D FBP prim+scat	61%	65%	61%	63%

Tab. 7.2: Different recovery ratios corresponding to primary and low energy scattered photons depending on the reconstruction algorithm. The corrections considered were attenuation (att) and PSF. All the reconstruction algorithms were evaluated in a 3D evaluation. Both 2D and 3D algorithms used 32 iterations.

Region of Interest (ROI)	Theoretical	SMFC
C_{left}	70	69.0
P_{left}	70	66.4
C_{right}	70	68.7
P_{right}	70	66.5
Background	10	9.9

Tab. 7.3: Absolute activity values of reconstructed images with the SMFC method. The corrections considered were attenuation (att), PSF and scattering. The reconstruction used 32 iterations.

7.3.3 Absolute quantitative values

The quantitative results may be compared not only with the corresponding $RRi's$ values with previous reconstruction algorithms but also with original absolute activity values at each voxel. On one hand, table 7.3 shows the different recovery ratios depending on the corrections used in the reconstruction algorithm:

On the other hand, absolute activity values corresponding to the different regions of interest (ROI's) are compared with theoretical values from the original activity virtual phantom:

Finally, the recovery ratios (RRi's) for the left caudate are compared using the primary photons only, the primary and scattered photons together (experimental projections) and the corrected values for the SMFC method applied on primary and scattered photons together. These results are shown in Figure 7.10:

We stopped the iteration $n = 32$ due to the increase of noise in the reconstructed image and the slow convergence to better quantitative results.

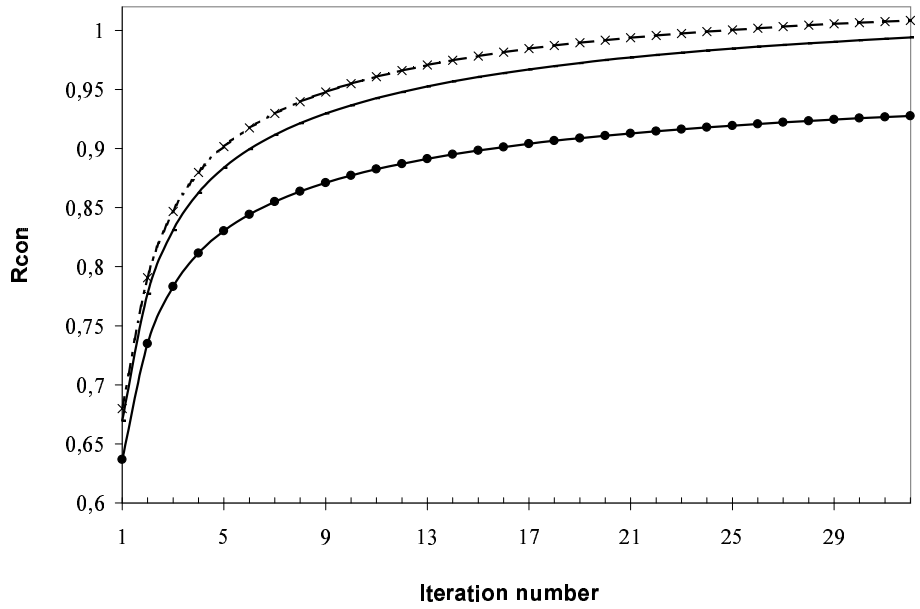

Fig. 7.10: Different recovery ratios of the theoretical values considering: primary photons only (dashed line with crosses), primary and scattered photons (line with circles) and all the photons using the SMFC method (continous line). These values correspond to the left caudate RRC_{left}.

7.3.4 Discussion

A 3D physical model for iterative reconstruction has been applied to a ^{99m}Tc SPECT neurotransmission study using a virtual phantom. The P3D-OSEM reconstruction provides a sharper image quality and improved accuracy in quantitative results.

The 3D SMFC model has been designed to be computationally fast with practical memory requirements. Several important features of the model have enabled this goal. Firstly, the scattering effect is corrected a part from the reconstruction algorithm without substantially increasing the noise. The scattering correction is handled using Monte Carlo techniques. Secondly, the size of the transition matrix is optimized by using a minimum element array threshold for the collimator blurring model. In this way, the number of array elements is reduced and also the RAM memory is decreased. Thirdly, at each iteration step only a part of the transition matrix is used corresponding to the ordered subset projection. Finally, absolute quantitative values on the reconstructed image are obtained using a normalization procedure. The reconstructed voxel values may be expressed as volumetric activity values ($\frac{\mu Ci}{cm^3}$) at each voxel of the object image. Therefore, absolute quantification is achieved.

8. SUMMARY AND CONCLUSIONS

"The relationship between humans and computers, that's the question."

The following results and concluding remarks are pointed out:

1. Monte Carlo simulations are the "gold standard" for testing reconstruction algorithms in Nuclear Medicine. We analyzed the available Monte Carlo codes and we chose SimSET as a virtual phantom simulator. A new stopping criteria in SimSET was established in order to reduce the simulation time. The modified SimSET version was validated as a virtual phantom simulator which reproduces realistic projection data sets in SPECT studies.

2. The 3D spatially variant collimator/detector response was obtained by Monte Carlo simulation including the geometric, septal penetration, coherent and incoherent scattering PSF components. The PENELOPE code was chosen as the PSF response simulator due to its great accuracy, wide range of energies and fast simulation transport including secondary particles through the collimator/detector system. A characterization of the PSF response for low-energy photons was performed for fan beam and parallel collimator configurations. A focus was made on the fan beam configuration, which is the optimal collimator for brain SPECT imaging.

3. The PSF responses for high-energy photons such those emitted by ^{123}I were obtained. Our results showed that the contribution of high-energy rays to the final image is greater in parallel collimators (49% to 28%) compared with fan beam collimators (41% to 11%). These results suggest that scattering in the collimator/detector system has to be taken into account for ^{123}I SPECT studies. The main features and variables to model such effects were described.

4. A new variance reduction method for SimSET Monte Carlo simulation was developed and assessed. We included our PSF_T model as a new PDF of the photon passing through the collimator/detector system per unit solid angle instead of the PDF per unit area based on the original SimSET code. This method provided a reduction of the simulation time greater than 2.

5. A Monte Carlo-based scattering correction method was developed. The estimated scattered photon distribution on the projections showed a good agreement with theoretical values. The use of the modified SimSET simulator accelerated the forward projection process although the computational burden is still a challenge for this technique. The use of advanced hardware architectures such as PC clusters may overcome this problem.

6. The significance of correcting degradations in reconstruction algorithms to improve quantification accuracy of brain SPECT studies was assessed. Our findings indicated that the 3D spatially variant collimator/detector response, the scattering effect and the high-energy ray contamination play a significant role in the quantification of both absolute and relative values on different structures such as the basal ganglia in neurotransmission studies.

7. Accurate 3D PSF modelling on both axes of the detector head results in a significant improvement of quantification results using full 3D iterative reconstruction (9%-13%) instead of 2D slice-by-slice reconstruction. The P3D-OSEM iterative algorithm was designed to be computationally fast with practical memory requirements. Firstly, the scattering effect was corrected a part from the reconstruction algorithm without substantially increasing the noise using Monte Carlo techniques but improving the quantification results (6%-7%). Secondly, the size of the transition matrix was optimized by using a minimum element array threshold for the collimator blurring model. In this way, the number of array elements was reduced and also the RAM memory was decreased. Thirdly, at each iteration step only a part of the transition matrix corresponding to the ordered subset projection was employed.

8. Full 3D reconstruction simultaneously applied with Monte Carlo-based scattering correction and the 3D evaluation procedure is a major upgrade technique in order to

obtain valuable, absolute quantitative estimates of the reconstructed images. This new procedure provided an improvement of 15%-20% respect to 2D slice-by-slice reconstruction without scatter correction.

9. The full 3D reconstruction method including all the corrections and a normalization procedure not only improves quantitative ratios of the image, but also supplies absolute values of volumetric activities in each voxel of the reconstructed image. The absolute reconstructed values were 95% of the theoretical values, whereas the theoretical correction limit (only primary photons calculated by Monte Carlo) yielded 97%. Thus, absolute quantification in brain SPECT imaging was achieved.

APPENDIX

A. FUNDAMENTALS OF THE MONTE CARLO TECHNIQUES

A.1 Mathematical definitions

A.1.1 Variable Definitions

Consider a measurable space ($\mathbf{H}$,Ω), where $\mathbf{H}$ is a set and Ω is a non-empty collection of subsets of $\mathbf{H}$ closed under complementarity and countable unions; the elements of Ω are measurable and independent.

A *probability measure* on $\mathbf{H}$ is a function μ that assigns to every element A of Ω a non-negative probability or measure $\mu(A)$ with the properties:

$$i)\ \mu(\mathbf{H}) \ = \ 1 \tag{A.1}$$

$$ii)\ \mu(\mathbf{\Omega_1} \bigcup \mathbf{\Omega_2} \bigcup ... \ \mathbf{\Omega_k}) \ = \ \sum_{i=1}^{k} \mu(\mathbf{\Omega_i}) \tag{A.2}$$

because Ω_1,Ω_2,... are disjoint measurable subsets of $\mathbf{H}$

If these magnitudes are translated to the field of Nuclear Medicine, $\mathbf{H}$ will be the space of all the possible detector locations. If all the space is covered by an infinite number of detectors, each decay history will be measured. The sum of probabilities for each particle to be detected, $\mu(\mathbf{H})$, would be equal to 1. However, Ω is only the subset of detector positions covered by the detector heads, and the detection probability $\mu(\Omega) << 1$.

The points of $\mathbf{H}$ are thought of as the individual outcomes of the process described by μ; an *event* is a bin detector point A of Ω (i.e. a measurable subset of the set of all possible outcomes), and $\mu(A)$ is just the probability that the event described by A will occur.

The real-valued function X on $\mathbf{H}$ is defined as the detector function which assigns a real value from a subset of events h related to the acceptable outcome of that particular detector. Then X is a *random variable* with the property that for any real number $\mathbf{K}$, the set of points $\mathbf{h}$ in $\mathbf{H}$ is such that $X(h) < K$ is measurable.

Integration with respect to μ must be defined. For suitable random variables X, the expectation or mean $E(X)$ and the variance $\mathrm{Var}(X)$ are defined as:

$$E(X) \;=\; \int X(h)d\mu(h) \;=\; \int X(h)\frac{d\mu(h)}{dh}dh \tag{A.3}$$

$$\mathrm{Var}(X) \;=\; E(X^2) - E(X)^2 \;=\; \int X^2(h)d\mu(h) - (\int X(h)d\mu(h))^2 \tag{A.4}$$

where $\frac{d\mu(h)}{dh}$ is the Probability Density Function (PDF) associated with the probability function $\mu(h)$.

A.1.2 Binomial Detector

The Binomial Detector is a certain type of function X: the characteristic function χ_Ω. It has two possible values:

$$\chi_A(A) \;=\; 1 \tag{A.5}$$

if the photon reaches the bin A, and:

$$\chi_A(H - A) \;=\; 0 \tag{A.6}$$

if the photon does not reach bin A. It is straightforward to verify that χ_A, the characteristic function of the bin detector A, is a random variable. In a measurable subset Ω of H (with non-zero measure), called the set of acceptable outcomes, the binomial detector of bin A fulfils the following properties:

$$E(\chi_A) \;=\; \mu(A) \tag{A.7}$$

$$\mathrm{Var}(\chi_A) \;=\; \mu(A) - \mu(A)^2 \tag{A.8}$$

A new variable N_A may be defined as the number of acceptable outcomes for a certain bin detector A after N_c emitted photons from the source. This variable is simply:

$$N_A \;=\; Nc\;\chi_A \tag{A.9}$$

Using statistical rules, the mean and the variance may be defined for this new variable N_A:

$$E(N_A) \;=\; Nc\; E(\chi_A) \;=\; Nc\; \mu(A) \tag{A.10}$$

$$\mathrm{Var}(N_A) \;=\; Nc^2\; \mu(A)(1-\mu(A)) \tag{A.11}$$

N_A could be considered as a binomial distribution because its characteristic function has only two values (whether it is detected or not). The binomial distribution is a well-known distribution in subjects of Statistical Mathematics [66]:

$$P(N_A = r) \;=\; \frac{Nc!}{r!(Nc-r)!}\mu(A)^r(1-\mu(A))^{Nc-r} \tag{A.12}$$

where the detector bin A measures r particles after Nc emitted photons.

In Nuclear Medicine applications, the detector set describes a target cylinder that only covers a sample of the total solid angle sphere. In addition, collimation of photons reduces the detected counts. Therefore, the probability over all the detectors for achieving one decay is really small $\mu(\Omega) << 1$.

A.1.3 Poisson Distributions

The detection probability for low energy photons of a point source in air for usual acquisition is very low, $\mu(A) < 10^{-4}$, on a single head SPECT camera. However the number of emitted photons Nc is very large. Under these conditions the Statistical Mathematics theory [66],[71] indicates that if these two conditions are satisfied:

1. If $Nc > 10$

2. If $\mu(A) < 0.05$

then the Poisson distribution appears as the limit of the binomial distribution:

$$\lim_{Nc\to\infty} P(N_A = r) \;=\; \frac{Nc!}{r!(Nc-r)!}(\frac{\lambda}{Nc})^r(1-(\frac{\lambda}{Nc}))^{Nc-r} \tag{A.13}$$

$$\lim_{Nc\to\infty} P(N_A = r) \;=\; \frac{\lambda^r}{r!}\lim_{Nc\to\infty}\frac{Nc(Nc-1)...(Nc-r+1)}{(1-\frac{\lambda}{Nc})^r Nc^r}(1-\frac{\lambda}{Nc})^N c \tag{A.14}$$

by using both limits simultaneously:

$$\lim_{Nc\to\infty} \frac{Nc(Nc-1)...(Nc-r+1)}{(1-\frac{\lambda}{Nc})^r Nc^r} \simeq \frac{Nc^r}{(1-0)^r Nc^r} = 1 \tag{A.15}$$

$$\lim_{Nc\to\infty} (1-\frac{\lambda}{Nc})^N c = e^{-\lambda} \tag{A.16}$$

and finally the well-known Poisson probability function arises:

$$\lim_{Nc\to\infty} P(N_A = r) = \frac{\lambda^r}{r!}\ 1\ exp^{-\lambda} \tag{A.17}$$

Another important parameter is the constant mean λ of the distribution:

$$E(N_A) = Nc\mu(A) = \lambda \geq 0.5 \tag{A.18}$$

In the Poisson distribution the variance equals to:

$$\mathrm{Var}(N_A) = \sum_{r=0}^{r=Nc} (r-\lambda)^2 \frac{\lambda^r}{r!} exp^{-\lambda} = \lambda \tag{A.19}$$

The main property of the Poisson Distribution is that mean and variance have the same value:

$$\mathrm{Var}(N_A) = E(N_A) = Nc\ \mu(A) = N_A = \lambda \tag{A.20}$$

A.1.4 Gaussian Distributions

A special case of the Poisson Distribution appears when the probability of detection is small $\mu(A) << 1$, but the number of events Nc is sufficiently large. In this case the number of detected counts $\lambda > K$ is large enough to convert the Poisson distribution to a Gaussian distribution with mean and variance equal to λ.

Some authors [71] situate this minimum threshold value at $K = 9$, while others situate it between $K = 5$ and $K = 30$ [36]. In Figure A.1 several Poisson distributions are shown with different λs showing convergence to the Gaussian distribution.

The χ^2 parameter between both distributions at $\lambda = 5$ was $\chi^2 = 0.0254$ with 29 degrees of freedom. The significance of this test was close to 100%. Moreover, the correlation coefficient between both distributions was 98.6%.

In fact, **most of the applications and theories used in Nuclear Medicine field are based on considering Gaussian distributions** at each detector bin. Such assumption may be taken when the following conditions are accomplished:

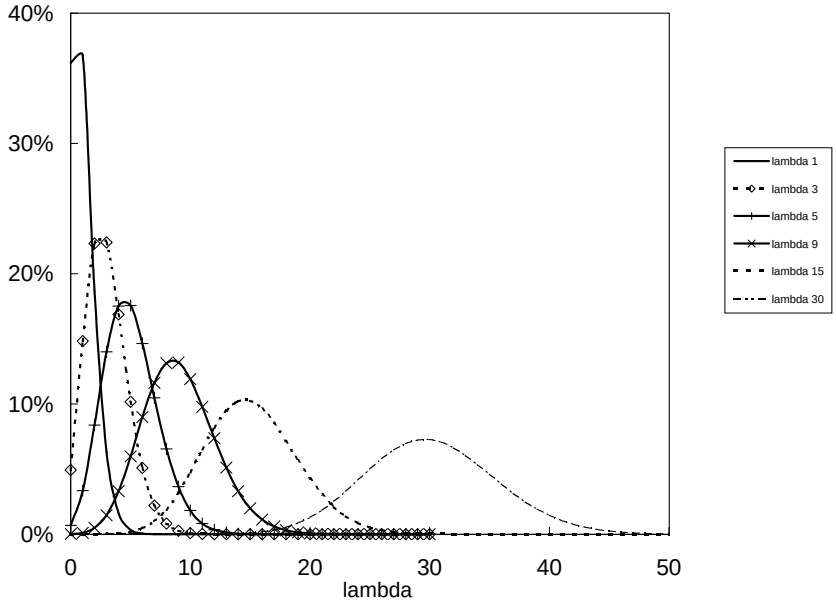

Fig. A.1: Different λ values for Poisson distributions

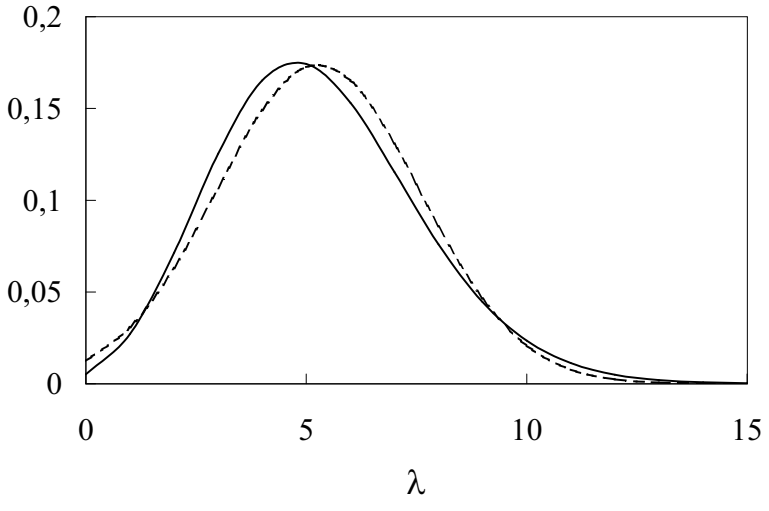

Fig. A.2: Poisson and Gaussian distribution at the same mean value $\lambda = 5$.

1. The detection of an event is independent to the others

2. There is a huge number of emitted photons (decays) from the source radioisotope

3. The probability of detection is very small

4. The product of the number of emitted photons N_c and the probability of detection ($\mu(A)$) –i.e. the counts at every detector bin N_A— is higher than the Poisson-to-Gaussian threshold, that is $\lambda > K$.

A.2 The Analogue Monte Carlo method

In Monte Carlo applications on Nuclear Medicine, the magnitude of interest is just the number of events received at a given detector A. However it is also necessary to sort an initial map of activity representing the source volume problem distributed in K voxels. In order to simulate this source volume, an initial sampling algorithm determines the initial location of the histories. The spatial probability density of the initial points of emission for each history must be proportional to the activity map.

Let us first introduce a way of achieving the estimators by a simple sorting of photons in a Standard Monte Carlo code. The sampling of each $\chi_A(h)$ history is defined by:

$$p_k(h) \;=\; \frac{A_k}{A} \tag{A.21}$$

Where the activity map is represented by a volume activity A_k in $\mu Ci/cm^3$ at each voxel k. If there are K voxels in the simulation then the activity map is:

$$\{A_k\}_{k=1..K} \tag{A.22}$$

$$A \;=\; \sum_{k=1}^{k=K} A_k \tag{A.23}$$

Thus, n_k decays are sorted at each voxel K of the object volume according the activity map. The decays are sorted voxel by voxel in a sequential order:

$$n_k \;=\; N_h \; \frac{A_k}{A} \tag{A.24}$$

with an initial weight:

$$w_0 \;=\; 1 \tag{A.25}$$

The Analogue Monte Carlo samples the detection probability function μ with no variance reduction technique. Once the N_h histories have been sorted with the density probability function p_k, they are tracked and a weight $w(h)$ is obtained at each detector bin A. The final tally is an estimate of the mean of detected events at each detector bin A. The magnitude estimated by Monte Carlo simulation is the number of events received at the detector bin A per particle simulated, that is:

$$E(\bar{\chi_A}) = \frac{\sum_{h=0}^{h=N_h} \chi_A(h) w(h)}{N_h} \tag{A.26}$$

With the variance:

$$\mathrm{Var}(\bar{\chi_A}) = \frac{\sum_{h=0}^{h=N_h} w(h)^2}{N_h^2} \tag{A.27}$$

By the **Central Limit Theorem** the variance of the tally is $1/N_h$ times that of the variance of a single tally, and what is more, the different estimated values themselves will tend to be normally distributed even if the random variable itself is not normally distributed. This fact is really important because it implies that the mean of the estimates is the same as the mean of the random variable. Thus the estimates themselves lead to a value for the mean.

$$\mathrm{Var}(\bar{\chi_A}) = \frac{1}{N_h}\{\frac{\sum_{h=0}^{h=N_h} \chi_A(h)^2}{N_h} - (\frac{\sum_{h=0}^{h=N_h} \chi_A(h)}{N_h})^2\} \tag{A.28}$$

Equation (A.28) may be simplified:

$$\mathrm{Var}(\bar{\chi_A}) = \frac{1}{N_h}\{E(\chi_A) - (E(\chi_A))^2\} = \frac{1}{N_h}\mathrm{Var}(\chi_A) \tag{A.29}$$

So the deviation in our estimate is related to the deviation of the parent distribution, and it decreases with the square root of the number of histories N_h. This is a fundamental result of classical Monte Carlo.

A.2.1 The Central Limit Theorem

If the results of an experiment are caused by a large group of independent events, each of which is individually irrelevant with respect to the group, it is expected that the results fit the normal distribution.

If N_{A0},N_{A1},...,, N_{An} are independent, random variables with mean μ_i and variance σ_i^2 and each one fits a probability density distribution —not necessarily the same— a new variable Y can be defined:

$$Y = \sum_{i=0}^{i=n} N_{Ai} \tag{A.30}$$

If n grows, the z variable defined as:

$$z = \frac{Y - \sum_{i=0}^{i=N_d} \mu_i}{(\sum_{i=0}^{i=N_d} \sigma_i^2)^{\frac{1}{2}}} \tag{A.31}$$

tends to the normal distribution N(0,1).

As a lemma, a new variable "mean of random variables" may be defined as:

$$\frac{Y}{n} = \frac{\sum_{i=0}^{i=n} N_{Ai}}{n} \tag{A.32}$$

which also fits a normal distribution (n is a constant value) with variance:

$$\mathrm{Var}(\frac{Y}{n}) = \frac{1}{n^2} \sum_{i=0}^{i=n} \sigma_i^2 = \frac{n\sigma_i^2}{n^2} = \frac{\sigma_i^2}{n} \tag{A.33}$$

In this lemma all random variables belong to the same distribution, with the same variance σ_i^2. This is the case of Monte Carlo simulations where a unique magnitude is estimated by sampling a unique PDF with random numbers.

Nevertheless, the biggest problem facing Monte Carlo techniques is the extremely slow convergence of the estimate. The estimate error is inversely proportional to the square of the size of the observation set (n). In other words, the algorithm has a convergence $O(\frac{1}{\sqrt{n}})$. Thus, to halve the error, the number of histories that have to be sorted has to be quadrupled (i.e. with a greater CPU time the variance can be reduced).

Much of the research in Monte Carlo methods has been directed towards increasing the convergence of the estimator by decreasing its intrinsic variance σ_i^2 and getting better results from fewer samples. The intrinsic variance is constant (randomly constant), but could be changed using Monte Carlo knowledge : **Variance Reduction Techniques (VRT)**.

A.3 Variance reduction techniques. Theory and Basis

There are two approaches to improve the Monte Carlo estimate. Those that do not require any a priori information about the distribution: **blind** Monte Carlo techniques:

1. Crude Monte Carlo

2. Rejection Monte Carlo

3. Weighted Monte Carlo

4. Quasi Monte Carlo

and those which use some knowledge of the distribution sampled: **informed** Monte Carlo techniques:

1. Stratified Sampling

2. Importance Sampling

3. Control variates

Let us describe the most important Variance Reduction Technique used in Nuclear Medicine applications, namely **Importance Sampling**.

A.3.1 Importance Sampling

Importance Sampling is a powerful general method for reducing the variance in many Monte Carlo calculations. The idea is that some regions of the probability density function (the "detection function") contribute more to the final estimate (detected "counts") than other regions. These are typically places where the function has a large value, or fluctuates both significantly and quickly. These regions have "more importance" than others, and the goal will be to sample these regions more densely to get a better estimate of what is happening. The compensation for non-uniform sampling is included so that the final estimate is unbiased.

Now suppose that ν is another measure, also defined on $(\mathbf{H}, \Omega)$, with the property that ν is concentrated on the set of acceptable outcomes for the subset of detectors Ω. Provided that the three conditions are covered on every subset of Ω:

1. $\nu(\Omega) \geq 0$

2. $\int_{\Omega} \frac{d\nu(h)}{dh} dh \ = \ 1$

3. On every subset of Ω with positive μ measure, the ν measure is also positive and there is essentially a unique function $\mathbf{w}(\mathbf{h}) \ = \ \frac{\mu(h)}{\nu(h)}$

4. For any real number $\mathbf{a}$, the set of points $\mathbf{h}$ in Ω such that $w(h) < a$ is measurable

The new distribution probability function $w(h)$ allows the following estimates to be found:

$$w(h) \;=\; \frac{d\mu(h)}{d\nu(h)} \tag{A.34}$$

$$E(\chi_\Omega) \;=\; \int_\Omega \chi(h) w(h) \frac{\nu(h)}{dh} d(h) \tag{A.35}$$

If $\mu(\Omega)$ is small, it follows that $w(\Omega)$ will also be small:

$$E(\chi_\Omega) \;=\; \int_\Omega \chi(h) d\mu(h) \;=\; \mu(\Omega) \tag{A.36}$$

since its mean value with respect to the new function $w(h)$ is just:

$$E(\chi_\Omega) \;=\; \int_\Omega \chi(h) w(h) d(h) \int_\Omega \frac{\nu(h)}{dh} d(h) \;=\; w(\Omega) \tag{A.37}$$

because $\int_\Omega \frac{d\nu(h)}{dh} dh = 1$ as $\nu(h)$ is concentrated on the set of acceptable outcomes from Ω.

$$E(\chi_\Omega) \;=\; \mu(\Omega) \;=\; w(\Omega) \;<<\; 1 \tag{A.38}$$

This new probability density function will also follow a Gaussian distribution and Monte Carlo techniques can be applied. The simulation will now be changed using a different sorting procedure. Compensation of this non-uniform distribution on the set of histories affects each history by a **weight factor w** in order to obtain the same estimates. We must now tally $\chi_A(h) w(h)/N_h$ for each history produced by the new simulation method. The mean and the variance of the new estimate will be:

$$E(\bar{\chi_A}) \;=\; \frac{\sum_{h=0}^{h=N_h} \chi_A(h) w(h)}{N_h} \tag{A.39}$$

$$\mathrm{Var}(\bar{\chi_A}) \;=\; \frac{1}{N_h} \{ \frac{\sum_{h=0}^{h=N_h} \chi_A(h)^2 w(h)^2}{N_h} - (\frac{\sum_{h=0}^{h=N_h} \chi_A(h) w(h)}{N_h})^2 \} \tag{A.40}$$

In this case it is not possible to substitute the variance in terms of the mean value, and a new sum must be tallied (a new variable in the simulation) in order to accumulate the $\sum w(h)^2$.

As shown in equations A.37 and A.38 the estimates of the two random variables X and $Y = wX$ are the same :

$$E_\mu(\bar{X}) \;=\; \int_A \chi(h)d\mu(h) \;=\; \mu(A) = \; w(A) \;=\; \int_A w(h)d\nu(h) \;=\; E_\nu(\bar{Y}) \tag{A.41}$$

That is, Y (sampled by the new distribution probability ν) gives an unbiased estimate of the probability of the event X occurring according to the underlying physics represented by the probability measure μ.

However the variances are very different:

$$\mathrm{Var}_\mu(\bar{X}) \;=\; \frac{1}{N_h}\{E(\bar{X}) - (E(\bar{X}))^2\} \;=\; \frac{1}{N_h}(\mu(A) - \mu(A)^2) \;\simeq\; \frac{\mu(A)}{N_h} \tag{A.42}$$

$$\mathrm{Var}_\nu(\bar{Y}) \;=\; E_\nu(\bar{Y}^2) - E_\nu(\bar{Y})^2 = \; \int_A w^2(h)d\nu(h) - (\int_A w(h)d\nu(h))^2 \tag{A.43}$$

and in particular,

$$\mathrm{Var}_\nu(\bar{Y}) \;\leq\; \int_A w^2(h)d\nu(h) \tag{A.44}$$

On the other hand, using the Cauchy-Schwartz inequality we obtain,

$$E_\nu(\bar{Y})^2 \;=\; (\int_A w(h)d\nu(h)\;)^2 \;\leq\; \int_A 1d\nu(h) \;\int_A w^2(h)d\nu(h) \tag{A.45}$$

$$E_\nu(\bar{Y})^2 \;\leq\; \nu(A)\int_A w^2(h)d\nu(h) \tag{A.46}$$

Now, if we combine the last two equations (A.45) and (A.46), we have that:

$$(1-\nu(A))\int_A w^2(h)d\nu(h) \;\leq\; \mathrm{Var}_\nu(\bar{Y}) \;\leq\; \int_A w^2(h)d\nu(h) \tag{A.47}$$

and since $\nu(A)$ is small, we obtain:

$$\mathrm{Var}_\nu(\bar{Y}) \;\simeq\; \int_A w^2(h)d\nu(h) \;=\; w(A)^2 \tag{A.48}$$

The comparison of both variances with the known unbiased mean value $w(h) = \mu(h)$ yields:

$$\mathrm{Var}_{\mu}(\bar{X}) \;=\; \frac{\mu(A)}{N_h} \neq \; \frac{w(A)^2}{N_h} \;=\; \mathrm{Var}_{\nu}(\bar{Y}) \tag{A.49}$$

when both $w(h) = \frac{\mu(h)}{\nu(h)}$ distribution functions $\mu(h)$ and $\nu(h)$ are small. As it is shown in last equation **one of the main goals of the reduction variance techniques is to maintain all the events weight** $w(h) < 1$ **using the adequate distribution function** $\nu(h)$.

A.4 Interpretation of the SimSET results

In this section we study the reliability, accuracy and interpretation of SimSET results. Two different kinds of simulations may be performed with SimSET:

1. Analogue Monte Carlo simulations: No variance reduction technique is included

2. Importance Sampling in Monte Carlo simulations: Weights are introduced to balance different distribution sampling functions

If an analogue simulation is performed, after N_h histories have been sorted, the mean and the variance estimator can be written as:

$$E(\bar{\chi_A}) \;=\; \frac{\sum_{h=0}^{h=N_h} \chi_A(h)}{N_h} \;=\; \frac{M}{N_h} \tag{A.50}$$

$$\mathrm{Var}(\bar{\chi_A}) \;\simeq \frac{1}{N_h}\{\frac{\sum_{h=0}^{h=N_h} \chi_A(h)^2}{N_h}\} \;=\; \frac{M}{N_h^2} \tag{A.51}$$

where M is the number of detected events. For the variance, the Cauchy-Schwartz inequalities can be applied and the expression becomes simplified.

On the other hand, we can use variance reduction techniques, where a different probability density function is used to sample the different histories. This new PDF can be chosen such that the new number of detected events, M', is larger than M (for the same number of simulated histories). Furthermore, the mean estimate has to be the same as that obtained in (A.50), in other words:

$$E(\bar{\chi_A}) \;=\; E(\bar{\chi'_A}) \tag{A.52}$$

$$\frac{M}{N_h} \;=\; \frac{\sum_{h=0}^{h=M'} w(h)}{N_h} \tag{A.53}$$

$$M \;=\; \sum_{h=0}^{h=M'} w(h) \tag{A.54}$$

However, the variance estimator:

$$\mathrm{Var}(\bar{\chi'_A}) \;\simeq\; \frac{1}{N_h}\{\frac{\sum_{h=0}^{h=N_h}\chi'_A(h)^2 w(h)^2}{N_h}\} \;=\; \frac{\sum_{h=0}^{h=M'} w(h)^2}{N_h^2} \tag{A.55}$$

should be reduced as much as possible. Haynor and the SimSET developement group [37] rewrote the variance estimator in the form:

$$\mathrm{Var}(\bar{\chi'_A}) \;=\; \frac{\frac{(\sum_{h=0}^{h=M'} w(h))^2}{M\ M'}}{\frac{(\sum_{h=0}^{h=M'} w(h))^2}{M\ M'}}\frac{\sum_{h=0}^{h=M'} w(h)^2}{N_h^2} \;=\; \frac{M}{N_h^2}\{\frac{M'\sum_{h=0}^{h=M'} w(h)^2}{(\sum_{h=0}^{h=M'} w(h))^2}\}\frac{(\sum_{h=0}^{h=M'} w(h))^2}{M\ M'} \tag{A.56}$$

In SimSET there is a statistical variable called the Quality Factor, QF, related to the reduction in variance caused by the non-homogenous balance distribution of weights which is defined as:

$$0 \;\leq\; \mathrm{QF} \;=\; \frac{(\sum_{h=1}^{h=M'} w(h))^2}{M'\ \sum_{h=1}^{h=M'} w(h)^2} \;\leq\; 1 \tag{A.57}$$

where the Cauchy-Schwartz inequality [79] is used as before, it can be shown that $\mathrm{QF} \leq\ 1$. Substituting both formulas (A.57) and (A.54) in the expressions obtained for the variance, $\mathrm{Var}(\chi'_A)$, yields:

$$\mathrm{Var}(\bar{\chi'_A}) \;=\; \frac{M}{N_h^2}\{\frac{1}{\mathrm{QF}}\}\frac{1}{M\ M'}M^2 \;=\; \frac{M^2}{M'\ N_h^2}\{\frac{1}{\mathrm{QF}}\} \tag{A.58}$$

Thus, the ratio between the analogue Monte Carlo variance and the variance obtained by variance reduction techniques, is given by:

$$\frac{\mathrm{Var_{VRT}}}{\mathrm{Var_{Analogue\ MC}}} \;=\; \frac{\mathrm{Var}(\bar{\chi'_A})}{\mathrm{Var}(\bar{\chi_A})} \;=\; \frac{\frac{M^2}{M'\ N_h^2}\{\frac{1}{\mathrm{QF}}\}}{\frac{M}{N_h^2}} \;=\; \frac{M}{M'\ \mathrm{QF}} \tag{A.59}$$

Analysis of the last equation (A.59) indicates that SimSET is designed such that:

1. There is an increase in the number of detected events M' (in comparison with the analogue simulation M) using alternative probability density functions (so that the

ratio $\frac{M}{M'}$ is decreased). Some of the Variance Reduction Techniques (VRT) used by SimSET are: *Interaction Forcing, Detection Forcing, Forced Non-Absorption* which allow photons to be tracked to regions of interest (e.g. critical zone, acceptance angle,...), enabling their detection.

2. An uniform map of weights is obtained. This way, QF $\rightharpoonup 1$ and a better variance reduction is reached. The upper limit for QF is obtained when all weights are equal to 1, that is, when the Analogue Monte Carlo is used. However in the VRT case, the techniques used are Russian Roulette (killing of photons whose weight undergoes a lower limit) and Splitting Particles (splitting photons whose weight is above an upper limit). The Weight Window is the control variable to avoid a great dispersion in the weight distribution (i.e. non-optimal distribution weight would reach 4 magnitude orders —from 0.01 to 100— whereas an optimal one would be set between 2 magnitude orders —from 0.1 to 10— depending on the case.

3. All the weights —artificial tracks or interactions— are adjusted with their real equivalent from underlying physics processes which have to be reproduced certainly at each step

However, what is more important for interpreting the statistical results is that: if both SimSET simulations (Analogue and VRT) have to yield the same mean (unbiased result) and the same variance (real statistical noise), then the following must be fulfilled:

$$E(\bar{\chi_A}) \;=\; M = \sum_{h=0}^{h=M'} w(h) = \; E(\bar{\chi'_A}) \tag{A.60}$$

$$\mathrm{Var}_{VRT} \;=\; \mathrm{Var}_{AnalogueMC} = \; M \;=\; M' \;\mathrm{QF} \tag{A.61}$$

However, the initial version of SimSET had no control of the mean number of counts or over the variance associated with a "real" or analogue equivalent simulation.

A.5 Adding or combining Monte Carlo simulations

Sometimes in order to obtain a first approach to the solution of a detailed problem, it is common to make a short simulation and obtain a preliminary projection image. Afterwards, when the statistics have been revised, the real noise in the image can be found with another longer simulation. The two images, A and B, can be added thus obtaining another mean and variance. Firstly, each image can be defined by its mean and variance:

$$E(\chi_A) \;=\; \frac{\sum_{h=0}^{h=N_i} w_i(h)}{N_i} \tag{A.62}$$

$$\mathrm{Var}(\chi_A) \;\simeq\; \frac{\sum_{h=0}^{h=N_i} w_i(h)^2}{N_i^2} \tag{A.63}$$

The new mean for the combined images is :

$$E(\bar{\chi_A}) \;=\; \frac{N_1\ E_1(\chi_A) + N_2\ E_2(\chi_A)}{N_1 + N_2} \tag{A.64}$$

That is, in the final form using (A.62) is set to:

$$E(\bar{\chi_A}) \;=\; \frac{\sum_{h=0}^{h=N_1} w_1(h) + \sum_{h=0}^{h=N_2} w_2(h)}{N_1 + N_2} \tag{A.65}$$

In order to calculate the new variance for the combined image, we use the statistical result of each:

$$\mathrm{Var}(E(\bar{\chi_A})) \;=\; \mathrm{Var}(\frac{N_1\ E_1(\chi_A) + N_2\ E_2(\chi_A)}{N_1 + N_2}) \tag{A.66}$$

$$\mathrm{Var}(E(\bar{\chi_A})) \;=\; \frac{1}{(N_1 + N_2)^2}\ (N_1^2\ \mathrm{Var}_1(\chi_A) +\ N_2^2\ \mathrm{Var}_2(\chi_B)) \tag{A.67}$$

Substituting the variance of each image (A.63) and (A.67) we obtain an expression for the variance of the combined image:

$$\mathrm{Var}(E(\bar{\chi_A})) \;=\; \frac{\sum_{h=0}^{h=N_1} w_1(h)^2\ +\ \sum_{h=0}^{h=N_2} w_2(h)^2}{(N_1 + N_2)^2} \tag{A.68}$$

A.5.1 Adding or combining SimSET simulations

In the case of SimSET simulations a similar result can be obtained by taking into account the differences in the definitions for the mean and the variance:

$$E(\chi_A) \;=\; \sum_{h=0}^{h=N_i} w_i(h) \tag{A.69}$$

$$\mathrm{Var}(\chi_A) \;\simeq\; \sum_{h=0}^{h=N_i} w_i(h)^2 \tag{A.70}$$

The mean for the combined images is equal to:

$$E(\bar{\chi_A}) \;=\; \frac{N_1\; E_1(\chi_A) + N_2\; E_2(\chi_B)}{N_1 + N_2} \tag{A.71}$$

Using the statistical results of each simulation we obtain:

$$E(\bar{\chi_A}) \;=\; \frac{N_1\; \sum_{h=0}^{h=N_1} w_1(h) + \;N_2\; \sum_{h=0}^{h=N_2} w_2(h)}{N_1 + N_2} \tag{A.72}$$

In order to calculate the new variance for the combined image, using the statistical results for each one of the images we have to compute:

$$\mathrm{Var}(E(\bar{\chi_A})) \;=\; \mathrm{Var}_1(\frac{N_1\; E_1(\chi_A) + N_2\; E_2(\chi_A)}{N_1 + N_2}) \tag{A.73}$$

$$\mathrm{Var}(E(\bar{\chi_A})) \;=\; \frac{1}{(N_1 + N_2)^2}\; (N_1^2\; \mathrm{Var}_1(\chi_A) + \;N_2^2\; \mathrm{Var}_2(\chi_A)) \tag{A.74}$$

$$\mathrm{Var}(E(\bar{\chi_A})) \;=\; \frac{N_1^2 \sum_{h=0}^{h=N_1} w_1(h)^2 \;+\; N_2^2 \sum_{h=0}^{h=N_2} w_2(h)^2}{(N_1 + N_2)^2} \tag{A.75}$$

B. DESCRIPTION OF THE SIMSET PACKAGE

B.1 Input data

The next section provides an introduction to the package along with a road map to the documentation and files [38] required to use the SimSET package. The flow chart of the SimSET package is presented in Figure B.1.

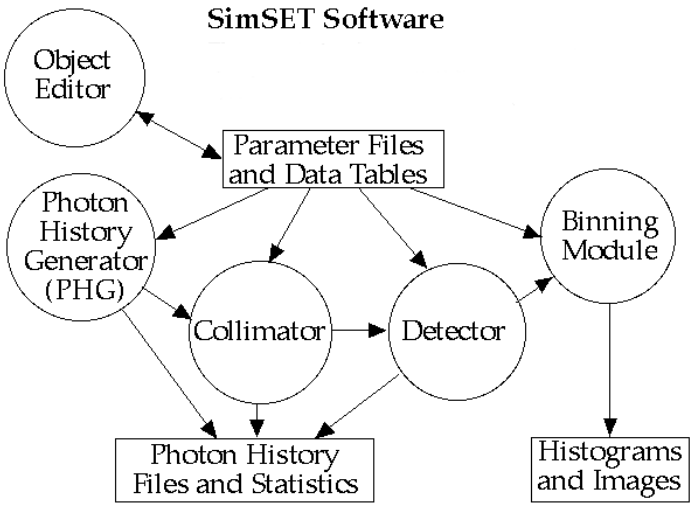

Fig. B.1: SimSET overview flow chart

The most relevant modules in SimSET are:

1. *Makeindexfile* : Data input interface (including attenuation and activity image output)
2. *Phg* : Tracking of photons through heterogenous media
3. *UncCollimator* : Collimation of the photons n Detector : Detection of collimated photons

4. *Bin* : Binning of detected photons ordered in histograms defined by the user

5. *Ttest* : T-Student test between different sinograms and projections

The core program of SimSET is the **P**hoton **H**istory **G**enerator —**PHG**—. PHG contains the physics and commands governing the transport of photons through different materials. In order to define which materials the media of transport is composed of and where the source origin of each photon, the user has to introduce the Attenuation and Activity Distribution.

The Activity Object defines the spatial distribution of isotope concentration from which photons will be generated. The Attenuation Object defines the spatial distribution of the attenuation bodies where photons will travel through. Although these two items contain different information for the simulation, they share a common geometric/parametric definition. Both items are needed to describe the Object as is shown in Figures B.2 and B.1.

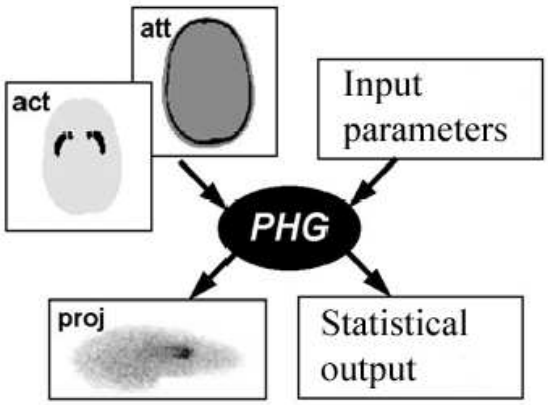

Fig. B.2: Photon History Generator diagram.The rounded rectangles at the top represent the various parameters that are required as input to the PHG, while the rectangles at the bottom represent the outputs of PHG

The Object (see Figure B.3) is defined in Cartesian coordinates as a three-dimensional grid of solid rectangular voxels. Each voxel contains an index for activity concentration and an index for attenuation values. Non-zero attenuation and activity values are restricted to the Object Cylinder, the largest right circular cylinder subtended by the three-dimensional grid. Photons are tracked to the Object Cylinder —any attenuation specified outside this cylinder is ignored—. No decays are simulated in voxels which are entirely outside the object cylinder.

The SimSET Object Editor module is **makeindexfile**, a stand-alone program which provides numerous options for setting the index values for both activity and attenuation.

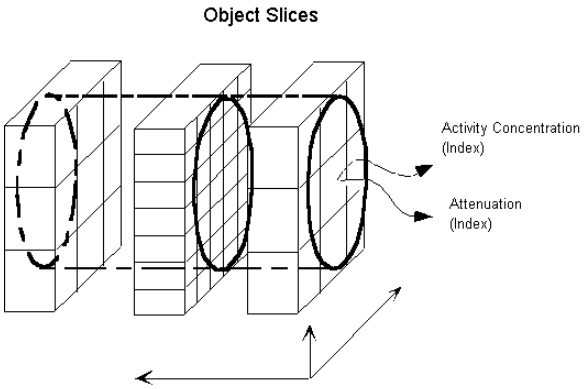

Fig. B.3: The object is defined inside the object cylinder represented in black line. This cylinder is inserted in a Cartesian three-dimensional grid of solid rectangular voxels with a user-defined value for activity and attenuation parameters

The Object Editor can use pre-existing files to initialize the object voxels on a slice-by-slice basis. This allows the simulations based on digital phantoms such as those introduced by Alderson, Hoffman and Zubal.

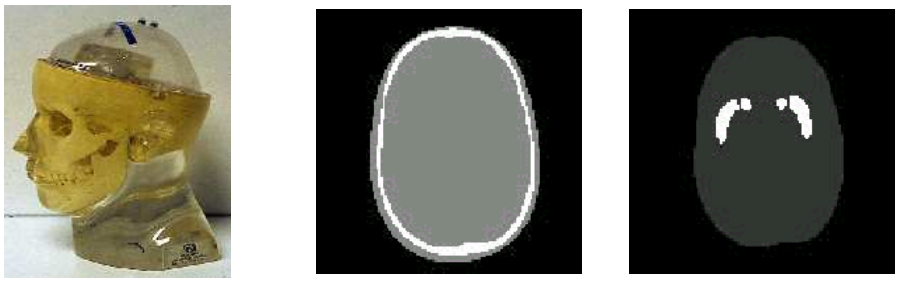

(A) (B) (C)

Fig. B.4: Alderson phantom for neuroreceptor SPECT studies. The experimental phantom is shown in —A— used for validation trials and the virtual phantom with its corresponding attenuation —B— and activity —C— maps for a certain slice.

B.1.1 Attenuation map

The Attenuation Table is initialized from a text file which contains an entry for each supported tissue type. The program contains a translation table between the integer and the material. Each material is described by a table of computed values for narrow-beam attenuation in cm^{-1} and relative probability of Compton scattering (Compton cross-section/total cross-section). The Attenuation table is ordered in steps of 1 keV from 50

keV up to 1000 keV.

The table can be generated automatically and may be modified to add new materials not currently supported. The tissue types and materials which are the most relevant in Nuclear Medicine studies are included in SimSET as described in Table B.1.

Tissue number	Name
0	air
1	water
2	blood
3	bone
4	brain
5	brain stem
6	calcium
7	cerebellum
8	cerebrum
9	cerebrospinal fluid
10	fat
11	heart
12	lung inflated
13	muscle
14	skin
15	lead
16	aluminum
17	lucite
18	tungsten
19	polystyrene
20	sodium iodide
21	perfect absorber

Tab. B.1: Tissue types defined in SimSET as default. It is also possible to include user-defined materials

B.1.2 Activity map

The activity table file contains the original radiotracer volumetric distribution. It is represented by 1 byte values at each voxel of the object. This is a list of 256 activity values in units of $\frac{\mu Ci}{cm^3}$.

Absolute Quantification will try to achieve the original absolute values in the reconstructed image.

B.1.3 Simulation Options

The PHG uses numerous data files to perform a simulation. The creation of these input files is automated whenever possible. All of the data files necessary for performing a simulation are described in a Main Parameter File. The parameter file is a text file divided into four sections:

1. The first section specifies run-time options:

1.1. *simulated stratification*: Controls the use of stratified sampling which is a variance reduction technique, consisting of sorting the initial direction of photons based upon a productivity table which sums up the most probable "detected" directions.

1.2. *simulated forced detection*: Controls the use of forced detection, another variance reduction technique based on forcing the scattered angle after a Compton interaction in order "to pass" through the collimator.

1.3. *forced non absorption*: If TRUE, photons are not absorbed as a result of interaction; instead, their weights are reduced proportionally by the probability that the interaction would result in Compton scattering. If FALSE, the probability of interaction is compared against a pseudo-random number to determine if the event will result in absorption or Compton scattering. Setting this option to TRUE will make more efficient use of each photon simulated.

1.4. *acceptance angle* (0-90 degrees): Only photons which strike the target cylinder with a direction vector whose angle with respect to the z-axis falls between $[90-\alpha, 90+\alpha]$ are considered for detection. α is the acceptance angle —See Figure B.5—.

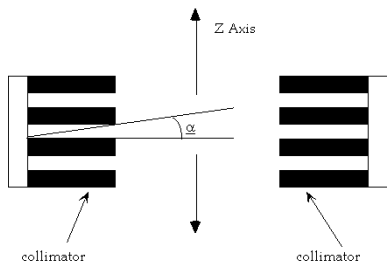

Fig. B.5: The acceptance angle is defined over the normal of the collimator. This normal is perpendicular to the z-axis, that is the tomograph axis where the object is placed.

1.5. *photon energy*: Initial photon energy (51 - 1000 keV).

1.6. *minimum energy*: Any photon whose energy falls below the minimum energy is considered to be absorbed. Photons are forced to Compton scatter until their energy drops below minimum energy and then they are discarded.

1.7. N_h: The number of histories to be simulated.

1.8. *weight window ratio*: The ratio which triggers weight-windowing in Forced Detection. It is used as a parameter in reduction variance techniques such as Russian Roulette and Splitting [e.g. weight window ratio = 3 would cause all photons whose estimated detection weight is less than 1/3 their target weight to undergo Russian roulette; a weight greater than 3 times the target weight would undergo photon splitting]. NOTE: Weight windowing is only performed when the weight window ratio is not equal to 1, the simulated forced detection option is true, and the input productivity table is not empty (i.e., the productivity table was computed in a previous run).

1.9. *point source voxels*:If set to TRUE this option causes all decays within a voxel to occur at the voxel center. Hence, a point source may be simulated by specifying activity in only one voxel and setting this flag to true.

1.10. *random seed*: This is the seed value for the random number generator. It can be any valid four-byte integer value. If it is zero, the generator is seeded from the system clock.

2. The second section specifies the overall geometry of the activity/attenuation object

3. The third section specifies the geometry of the target cylinder. This is the cylinder described by the collimator/detector planar system after rotation of 360° centered on the tomograph axis about the object.

4. The fourth section provides the path-names to the various output files

B.2 Tracking

An important part of the SimSET package is the **PHG**. It contains modules for photon generation, tracking and interaction in voxelized heterogeneous objects. It is similar in principle to other Monte Carlo-based simulation software, such as SIMIND [52], EGS [58] and MCNP [13]. The main differences from emission tomography applications are related to ease-of-use flexibility, optimization and efficiency to perform simulations in Nuclear Medicine fields.

Each photon is tracked from its starting location to the surface of the Object Cylinder. From there, the photon is projected to a bounding cylinder referred to as the Target

Cylinder. The radius and axial extent of the Target Cylinder are user-specified; they will usually be determined by the radius and axial dimensions of the detection/collimation system to be simulated. The space between the Object Cylinder and Target Cylinder is modelled as a vacuum. All photons that reach the Target Cylinder within a user-specified axial Acceptance Angle will be included in the Photon History List. The "Tracking Photons" flow chart includes a "Collimate Photon" and "Detect Photon" step as Figure B.6 shows.

Interaction tables and angular distribution data tables were generated using photon interaction data from the EPDL database and human tissue composition data from the ICRP Reference Manual. The interaction tables which include linear attenuation coefficients and data to calculate relative probabilities of photoelectric absorption, Compton scattering and coherent scattering were extended to cover the complete range of 1 keV to 1000 keV.

It should be pointed out that the forced detection algorithm, one of the importance sampling techniques previously incorporated into SimSET to increase its efficiency, is not compatible with the current use of coherent scatter. This is essentially due to the strongly forward-peaked angular distributions associated with coherent scattering, which result in an unacceptably large variation in the detected photon weights. However other importance sampling techniques used by SimSET (e.g. importance sampling, etc.) are compatible with coherent scattering, which do not imply an impact on the simulation speed.

B.3 Collimator Modules

The SPECT Collimator Module performs the collimation process of those photons which hit the target cylinder, that is those that reach the collimator surface. Tracking photons through the collimator can occur automatically during execution of the PHG, or as a post-processing step operating on the photon history list. There are three types of hole geometries supported by the collimator module, parallel (conventional), fan beam, and cone beam.

In SimSET, the probability of crossing the collimator and being detected is based on the geometric model developed by Frey et al. [32]. Steven Vannoy and Dave Lewis have adapted the PSF functions in the SimSET collimator module. For each photon that reaches the face of the collimator, the probability of passing through it without interaction is computed. The photons which would pass through the collimator whole are accepted and their weight is adjusted according to the probability density function. There is no modelling of scattering within the collimator nor septal penetration because the photon is supposed to pass only through the collimator opening using geometrical criteria. Thus, this model does not use any Monte Carlos tracking simulation in the collimator.

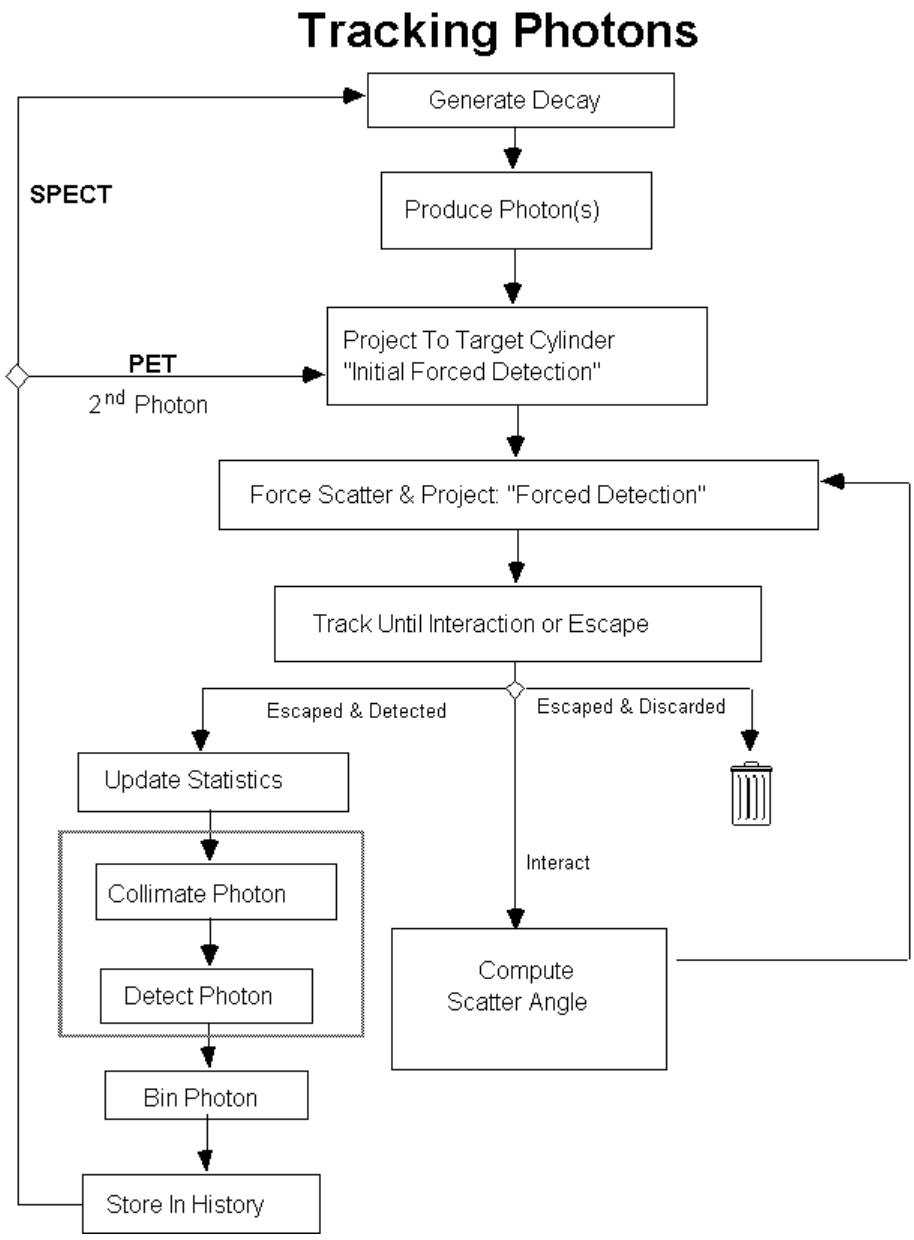

Fig. B.6: The control flow for tracking photons is described for both SPECT and PET simulations in SimSET.

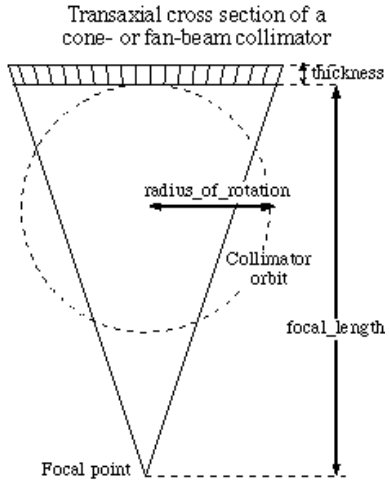

Fig. B.7: Transaxial view of a fan beam collimator

B.4 Detector Modules

The Detector module receives photons directly from the Collimator module. This module tracks photons by Monte Carlo techniques inside the specified detector and it records the deposited energy for each photon. The different interaction locations in the crystal are used to compute the centroid point of the detected event. Gaussian energy blurring may be applied due to the finite energy resolution of the crystal used as a detector. The user has to specify the energy resolution of the crystal and the detection window energy applied for each different isotope and study.

The "flat detector" mode provides a full simulation (including scatter, absorption, and penetration) of photon interactions in the detector head. The detector is modelled as layered rectangular parallelepiped (see figure B.8). The Flat Detector can be rotated around any angular range with a fixed radius or rotation and the user may specify the number of tomographic views. The radial and axial position of the detector is predetermined by the collimator module.

Flat (SPECT) and dual head coincidence (PET) detector models are currently supported, together with a "simple" model in which only the Gaussian energy blurring is performed. Photomultiplier tubes and electronic devices that are connected may be represented by an additional layer as will be discussed in Chapter 5.

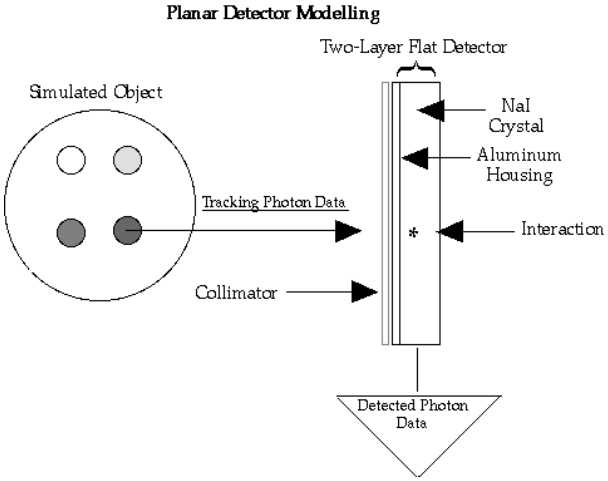

Fig. B.8: The flat detector modelling is the standard one used in SPECT gamma cameras. It allows the user to specify the thickness of each material, energy resolution of the crystal and window energy defined by the camera electronics

B.5 Output data

B.5.1 The binning of output data

For PHG the history list —the list of output photons of the simulation— only contains information of photons which reach the Target Cylinder within the acceptance parameters of the simulation. The collimator and detector module are both capable of creating a post-simulation (by Monte Carlo methods or using analytical deterministic functions) in order to create another history list output. The formats are the same, and the stand-alone binning module treats all of them equally.

The binning module will create a multi-dimensional histogram (sinogram) from a list of photons, giving the number, weight, and the sum of weight squared for each photon in each detector pixel (bin). These sinograms are stored in arrays of counts, weights and square weights as they are the simulated projections.

The binning step is defined by the user and it is another input file in the simulation.The following list of parameters describes the available binning options:

1. *scatter(s)*: splits the projection in primaries (unscattered) and scattered depending on the number of scatter interactions (max scatter - min scatter +1)
2. *Z Axis*: bins the projection according to their z-axis position in the detector head
3. *Transaxial Distance*: bins the projection according to their y-axis position in the

detector head

4. *Azimuthal Angle*: Binning by azimuthal angle is specified in terms of the range of tomograph angles within the acceptable range which is $(0 - 2\pi)$ for SPECT

5. *Energy*: Binning by energy is specified in terms of the range of acceptable energies and the number of bins within this range. It represents the detector energy window.

B.5.2 Statistical Results

Apart from the image projections onto the tomograph detectors, SimSET also presents a statistical summary with the most relevant results from the simulation.

Statistic variable	Description	Form
Started photons	Number of histories	N_h
Started primary	Number flagged primary	
Started weight	Number of initial weights	$\sum_{h=0}^{h=N_h} w_0$
Low energy photons	Photons below Emin	
Split photons	Photon weight exceed window	
Roulette attempts	Killed by Russian Roulette	
Det.photons	Photons at front collimator	
Det.primary weight	Weights of primaries	$\sum_{h=0}^{h=N_h} w_p$
Det.primary w.squared	Squared Weights of primaries	$\sum_{h=0}^{h=N_h} w_p^2$
Det.scatter weight	Weights of scattered	$\sum_{h=0}^{h=N_h} w_s$
Det.scatter w.squared	Squared Weights of scattered	$\sum_{h=0}^{h=N_h} w_s^2$
Det.photon energy histogram	Histogram by energy	
Det.photon weight scatters	Histogram by n°scatters	
Quality Factor	Measure variance reduction	QF
Real time	Simulation time	T_{CPU}

Tab. B.2: Statistical results given by a SimSET simulation

C. DESCRIPTION OF THE CODE FOR PSF MODELLING

C.1 Manual of the simulation program

The code implemented in order to simulate the PSF at different point sources locations and different collimator geometry was written in FORTRAN 77[1]. The code is based on PENELOPE code using the following routines linked with the main code:

1. *spect.f* : FORTRAN code used to initialize, track, score and save all the photons simulated. This code calls all the routines below. The geometry is initialized each time a photon is sorted. At the impact point, a new hole net is located.

2. *col3malla4.f* : FORTRAN code used to define the look-up table of all the hole centers. The output file with all the hole center positions (x1,x2,y1,y2,e1,e2) is **defcol.out**. It also creates a net of holes using the surfaces defined in PENELOPE geometry. The output files describes each body (hole) with its 6 surfaces (for hexagonal shape) described by 4 indexes, in quadric format, that is:

$$A_X x + A_Y y + A_Z z + A_0 = 0 \tag{C.1}$$

A part from quadric indexes it is also included a side pointer index which decides the orientation of body location over or under the surface using the normal vector of the plane as the positive direction. A part from the holes it is also defined the collimator body, outside the holes, with a L depth. Finally the detector body is everything else under a planar surface at $L + B$ from the front-plane collimator.

The material of each body is defined in **spect.mat** using the program material of penelope in generating this file. All the information about the material is written on the screen when executing the compiled program.

3. *penelope.f* : FORTRAN code defining the main PENELOPE routines for simulating the photon through the object. This routine call to the complete set of subroutines

[1] Its compilation used g77 from the GNU project under Linux or UNIX operating systems

defining the physics of different interaction, the track-length step, the variance reduction techniques, etc.

4. *peng2.f* : FORTRAN code used as major PENELOPE routine for defining the geometry of the simulation. It has changed from pengeom2.f (original file in PENELOPE package) the number of PARAMETER (NS=250,NB=125,NX=500) in order to enable the number of surfaces needed. PENELOPE has two parameter to be changed, in the file pengeom.f (the geometry file that manages all the looking up for the boundaries and surfaces) , NS=number of surfaces and NX=number of crossing boundaries,if it reaches more than a certain number of surfaces. The new files are peng2.f, peng5.f, etc.

5. *time2.f* : FORTRAN code defining the major PENELOPE routines for describing the lack of time of the simulation

Finally, all these files are compiled and linked in the executable program spect.x[2]. In order to execute the program, the following files are needed as input information:

1. *collimator.sim* : It describes the following parameters in cm.

1.1. L = Collimator thickness (i.e. 4 cm)

1.2. B = Image plane situation under the collimator backplane (i.e. 0.8 cm)

1.3. F = Focal height of the focus line in a fan beam (i.e. 35.5 cm). In the parallel collimator it tends to inf

1.4. Collimator height = Height of the collimator surface (i.e. 25 cm)

1.5. Collimator width = Width of the collimator surface (i.e. 50 cm)

1.6. Apothema x = Apothema in x-direction of the hexagonal hole (i.e. 0.075 cm)

1.7. Apothema y = Apothema in y-direction of the hexagonal hole (i.e. 0.075 cm)

1.8. Septa thickness = Width of the septa wall between holes (i.e. 0.02 cm). Note this septa grows with distance to z-axis with the elongation factor

2. *font.sim* : It describes the point source location in (X_0, Y_0, Z_0)

3. *spect.mat* : It describes all the materials ordered in a list. This order defines the number of each material referenced in **sup.geo**

[2] g77 spect.f peng2.f penelope.f col3 malla4.f time2.f -o spect.x

Once the program is executed two different kinds of files are written:

1. Geometry output file:

1.1. *def col.out* : it contains all the information about the center positions on the look-up table

1.2. *sup.geo* : it describes all the bodies and surfaces used in the object geometry

2. Simulation results:

2.1. *energy.out* : energy spectra of the detected photons

2.2. *stat.out* : statistical results of the detected photons ordered by different components. In this file there is the efficiency result of the point source

2.3. *g.out*, *ps.out*, *r.out*, *s.out* and *t.out* : image files with the geometrical, septal penetration, rayleigh (coherent scatter) and Compton (incoherent scatter) components of the PSF. With these files is possible to get the spatial sigma parameters

2.4. *g2.out*, *ps2.out*, *r2.out*, *s2.out* and *t2.out* : image error of the PSF results with its corresponding variances

C.2 Description of the fan beam specific geometry

To prevent the geometry routines from carrying all the holes each time a photon travels through the collimator, an approach that would have represented an excessively large amount of data, the description of the geometry was split into two steps. First, during the initialization, all the centers and elongations for each hole were stored in a look-up table which took into account all the characteristic parameters such as the focal length, collimator thickness, etc. This table remained unchanged during all the simulation. Each hole center was calculated using the recurrence relation defined by:

$$X_n = X_{n-1} + \frac{\Delta R_0}{\cos(\psi_{n-1})} \tag{C.2}$$

$$cos(\psi_{n-1}) = \frac{F}{\sqrt{F^2 + X_{n-1}^2}} \tag{C.3}$$

where X_n is the position of the center of the n-th hole on the fan beam axis (x-axis), ΔR_0 is the distance between two hole centers at the origin ($X_0 = 0$) in the fan beam direction, and $\frac{1}{\cos(\psi_{n-1})}$ is the elongation factor depending on the angle ψ_{n-1}, between the

axis of the (n-1)-th hole and the central axis. ΔR_0 was fixed to 0.1643 cm along the x-axis whereas $W = 0.075$ and $s = 0.02$ cm. As the point source moved away from the central axis, the elongation factor increases and the effective values of hole radius and the septa rose by 20%.

A difficult case of sorting photons arises in the fan beam collimator when the source is away from the center of the collimator. in this case, the main program calculate:

1. The hole center X_n which center passes through the line defined by the source point $S = (X_0, Y_0, Z_0)$ and the focal line F

$$X_n \;=\; X_0 \frac{F}{F - Z_0} \tag{C.4}$$

2. Once it has been found X_n, the program calculates its left- and right-borders X_M, that is, the maximum distance reached by photons passing through collimator at both sides of X_n [65]:

$$X_{M_{right}} \;=\; X_n \;+ X_M \;- X_0 \tag{C.5}$$

$$X_{M_{left}} \;=\; X_n \;- X_M \;- X_0 \tag{C.6}$$

3. With these two points $X_{M_{right}}$ and $X_{M_{left}}$, the program calculates the maximum and minimum aperture angles:

$$cos(\alpha_{min}) \;=\; \frac{Z_0}{\sqrt{Z_0^2 + X_{M_{right}}^2}} \tag{C.7}$$

$$cos(\alpha_{max}) \;=\; \frac{Z_0}{\sqrt{Z_0^2 + X_{M_{left}}^2}} \tag{C.8}$$

4. And as the program uses a Monte Carlo technique in order to simulate the transport, the final emission angle (in polar coordinates (α, φ))is sorted using a random number generator $\xi \in [0, 1]$:

$$cos(\alpha) \;=\; -cos(\alpha_{max}) + (cos(\alpha_{max}) - cos(\alpha_{min}))\xi \tag{C.9}$$

$$\varphi \;=\; 2\pi\xi \tag{C.10}$$

5. So the final director cosines (u, v, w) of the particle are :

$$u = sin(\alpha)cos(\varphi) \tag{C.11}$$

$$v = sin(\alpha)sin(\varphi) \tag{C.12}$$

$$w = cos(\alpha) \tag{C.13}$$

6. And the weight factor W of the photon in order to correct the isotropic emission over the 4π emission field is:

$$W = \frac{cos(\alpha_{max}) - cos(\alpha_{min})}{2} \tag{C.14}$$

In order to simulate the experimental measurements the program received as input parameters:

1. The distance between hole centers in the x-axis of the fan-beam. This value was measured with a ruler on the front collimator plane and was set constant during all the simulations.

$$\Delta R_0 = 2\ (0.1643)cm = 0.2846cm \tag{C.15}$$

2. Also, it was measured the parameter ΔRy_0 on the y-axis:

$$\Delta Ry_0 = 0.17cm \tag{C.16}$$

Both factors were constant over all the collimator array but affected by the elongation factor as presented in the above section

3. The radius circle "circumscribing" the hexagonal hole has an initial value of:

$$R_x = R_y = 0.0866cm \tag{C.17}$$

but as the center hole is away from the z-axis, the radius in x-coordinates is elongated while the radius in y-coordinates remains fixed:

$$R_{x_n} = \frac{R_x}{cos\psi_{n-1}} \tag{C.18}$$

The program uses the apothema variable for hexagonal hole shape instead of the radius variable[3].

$$W_x = W_y = R_x \cos(30^\circ) = 0.075cm \tag{C.19}$$

C.3 Equivalent results with different hole shape

The geometry model implemented in the PENELOPE's simulation reproduces the exact location of each hole on the fan beam collimator, with its exact shape. The program can manage different hole shapes. This feature is critical in the characterization of the collimator. However, other programs such as SimSET or Simind cannot simulate some specific shapes. An equivalence between different hole shape characteristics in order to obtain an equivalent result is presented:

C.3.1 Round holes

Referring at the hole shape, the program calculates similar PSF results considering equivalent areas for different hole shapes. In the case of round holes, the equivalent area to the hexagonal one is:

$$Area_{hex} = 12\frac{bh}{2} = 12\frac{\frac{R}{2}R\cos(30^\circ)}{2} \tag{C.20}$$

$$Area_{round} = \pi\hat{R}^2 \tag{C.21}$$

$$Area_{hex} = Area_{round} \tag{C.22}$$

$$\hat{R} = \sqrt{\frac{3\sqrt{3}R^2}{2\pi}} \tag{C.23}$$

Thus, the simulation results are equivalent when the hole radii $R = 0.866$ is used for the hexagonal hole, and the $\hat{R} = 0.07875$ for the round hole[4].

[3] Some authors [65] refer W as the radius variable

[4] The round hole is implemented in the standard SimSET simulations using the PSF_G Frey model

C.3.2 Square hole

This hole shape is used in the simulation code SIMIND created by Ljungberg et al. [52] and the approximation of the collimator modelled by square holes was developed by De Vries et al. [84]. De Vries indicate: "Since the values for the hole size, septal thickness and collimator thickness specified for the simulated collimator were the same as those of the collimator used in the experiments, the collimators have the same total lead content per unit area of detector surface. Therefore, we expected the radially averaged penetration and collimator scatter components to be independent of hole shape even though the penetration components exhibit a hole shape dependence in a two-dimensional image". The equivalent radii for the square hole approximation is:

$$Area_{hex} \;=\; 12\frac{\frac{R}{2}R\cos(30^\circ)}{2} \;=\; \frac{3\sqrt{3}}{2}R^2 \tag{C.24}$$

where R is the radius of the circumference that circumscribe the hexagon. If it is defined a square whith side L[5], thus:

$$Area_{square} \;=\; L^2 \tag{C.25}$$

As similar to round holes, the assumption of equivalent areas is determined by:

$$Area_{hex} \;=\; Area_{square} \tag{C.26}$$

That lasts to:

$$L \;=\; \sqrt{\frac{3\sqrt{3}}{2}R^2} \tag{C.27}$$

This relation may be expressed in terms of the hexagonal apothem, W:

$$R \;=\; \frac{W}{\cos(30^\circ)} \tag{C.28}$$

it vanishes to:

$$L \;=\; \sqrt{2\sqrt{3}W} \tag{C.29}$$

The hole array configuration of the collimator using square holes is defined by the distances between neighbor holes which is:

[5] The distance from the center to the border is $\frac{L}{2}$

$$\Delta R_0 = L + S \tag{C.30}$$

$$\Delta Y_0 = L + S \tag{C.31}$$

D. THE PSF_G MODELS AND THE PDF VARIABLE CHANGE

D.1 The PSF_G models

D.1.1 Metz and Tsui model for PSF_G

As shown in Figure 6.2, a pair of tapered holes which are located in a perfectly opaque slab of thickness L are considered. The hole axis is focused on the focal line at a distance F from the front plane collimator[1]. The distance between the collimator backplane and the image plane inside the scintillation crystal is represented by B[2]. The aperture function value equals 1 if the position vector $\vec{\eta} - \vec{r'}$ falls inside the aperture hole and 0 otherwise. Let $a_f(\vec{\eta} - \vec{r'})$ and $a_b(\vec{\varepsilon} - \vec{r''})$ be the aperture functions of the collimator holes at the front and back planes of the collimator, respectively, and let $\vec{r_i'}$ represent the position of the center of the i-th hole aperture at the front plane. $\vec{\eta}$ is the vector which moves freely on the front plane and $\vec{\varepsilon}$ moves freely in the black plane of the collimator.

First the straight line joining S (the source point) and I (the image point inside the overlapped circles) is defined in order to obtain the projected image point of the source as shown in figure D.1:

$$\mathbf{S} \equiv (x_0, y_0, L + B + Z) \tag{D.1}$$

$$I \equiv (x_I, y_I, 0) \tag{D.2}$$

The impact point of the emitted photon onto the front collimator plane is:

$$x = x_I + t(x_0 - x_I) \tag{D.3}$$

[1] This model is developed for fan beam (convergent collimators) and parallel collimators. The parallel case is just a detailed case of the convergent collimator by considering $\lim_{F \to \infty}$

[2] This is a virtual distance. It represents the "virtual" plane where the image is formed. It depends on the crystal width and is user-defined

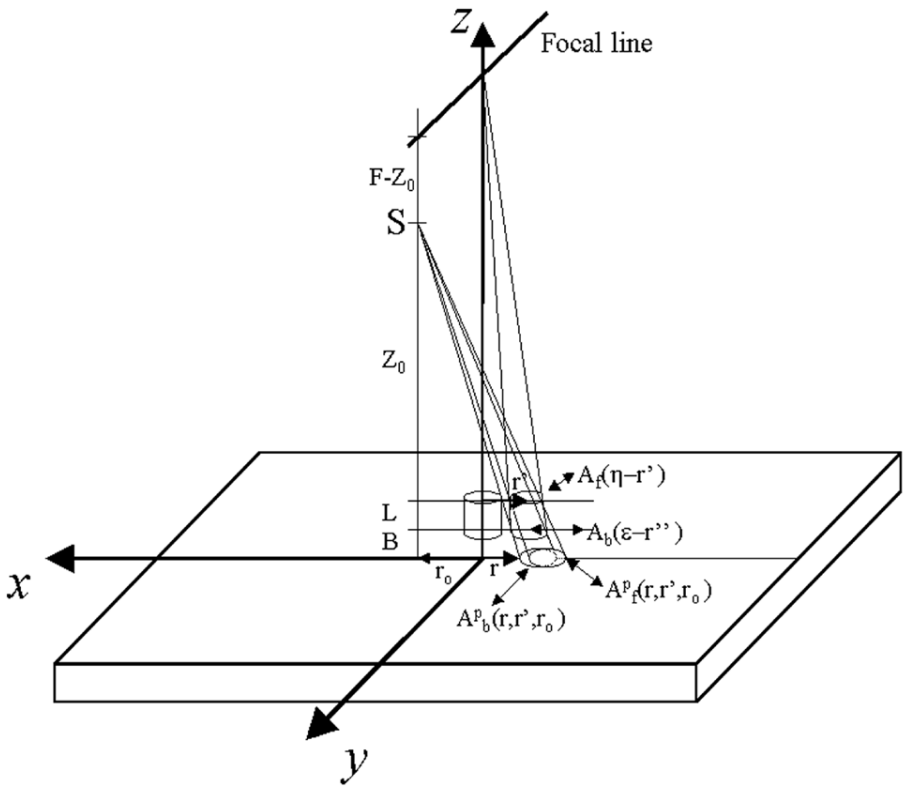

Fig. D.1: A pair of tapered holes which are located in a fan beam collimator. The geometry including all the details is described in Section D.1.1.

$$y = y_I + t(y_0 - y_I) \tag{D.4}$$

$$z = t(L + B + Z) \tag{D.5}$$

The front collimator plane is placed at a height of $L + B$ along the z-axis, i.e.:

$$z = L + B \tag{D.6}$$

The intersection parameter t is set to:

$$t = \frac{L + B}{L + B + Z} \tag{D.7}$$

and the intersection point on the front collimator plane is:

$$x = (x_I \frac{Z}{L + B + Z}, x_0 \frac{L + B}{L + B + Z}) \tag{D.8}$$

$$y = (y_I \frac{Z}{L + B + Z}, y_0 \frac{L + B}{L + B + Z}) \tag{D.9}$$

$$z = L + B \tag{D.10}$$

The last expression allows the vector $\vec{\eta}$ to be written on the front plane collimator in terms of the variables $\vec{r_i'}$ (i-th hole position on the front plane) and $\vec{r_0}$ (the source projection on the image plane):

$$a_f(\vec{\eta} - \vec{r_i'}) = a_f(\vec{r}, \vec{r_i'}, \vec{r_0}) = a_f(\frac{Z}{L + B + Z} r + \frac{L + B}{L + B + Z} \vec{r_0} - \vec{r_i'}) \tag{D.11}$$

Similarly the same expression may be deduced for the back collimator in terms of the front collimator aperture. A triangular relation between vectors $\vec{\eta}$ and $\vec{\varepsilon}$ reads:

$$\frac{\vec{\eta}}{F} = \frac{\vec{\varepsilon}}{F + L} \tag{D.12}$$

$$a_b(\vec{\varepsilon} - \vec{r_i'}) = a_b(\vec{r}, \vec{r_i'}, \vec{r_0}) = a_f(\frac{F}{L + F} \frac{Z}{L + B + Z} \vec{r} + \frac{F}{L + F} \frac{B}{L + B + Z} \vec{r_0} - \vec{r_i'}) \tag{D.13}$$

A variable change using the new variables $\vec{\sigma}$ and $\vec{r_t}$ defined as:

$$\vec{\sigma} = \vec{r_i} - \frac{L}{(Z+L+B)\vec{r}} - \frac{L+B}{(Z+L+B)\vec{r_0}} \tag{D.14}$$

$$\vec{r_t} = \frac{L}{(F+L)(Z+L+B)}((F-Z)\vec{r} - (F+L+B)\vec{r_0}) \tag{D.15}$$

and the sensitivity definition is set to:

$$\eta(\vec{r_t}) = k \int\int a_f(-\vec{\sigma}) a_f(\vec{r_t} - \vec{\sigma}) d^2\vec{\sigma} \tag{D.16}$$

After this change of variables, the sensitivity may be transformed in the Fourier space:

$$\eta(\vec{r_t}) = k \int\int a_f(-\vec{\sigma}) a_f(\vec{r_t} - \vec{\sigma}) d^2\vec{\sigma} \tag{D.17}$$

$$\eta(\vec{\mu}) = \mathcal{F}(\eta(\vec{r_t})) \tag{D.18}$$

In the general case, the new variable is substituted:

$$\eta(\vec{\mu}) = \frac{k}{\sqrt{2\pi}} \int\int \mathrm{e}^{-i\vec{r_t}\vec{\mu}} d^2\vec{r_t} \int\int a_f(-\vec{\sigma}) a_f(\vec{r_t} - \vec{\sigma}) d^2\vec{\sigma} \tag{D.19}$$

$$\vec{\nu} = \vec{r_t} - \vec{\sigma} \tag{D.20}$$

$$d^2\vec{\nu} = d^2\vec{r_t} \tag{D.21}$$

$$\eta(\vec{\mu}) = \frac{k}{\sqrt{2\pi}} \int\int a_f(-\vec{\sigma}) d^2\vec{\sigma} \int\int a_f(\vec{\nu}) \mathrm{e}^{-i\vec{\mu}(\vec{\nu}+\vec{\sigma})} d^2\vec{\nu} \tag{D.22}$$

and another substitution:

$$\vec{\kappa} = -\vec{\sigma} \tag{D.23}$$

$$d^2\vec{\kappa} = d^2\vec{\sigma} \tag{D.24}$$

Then the Fourier transform of the integral is the product of conjugate Fourier transform functions:

$$\eta(\vec{\mu}) \;=\; \frac{k}{\sqrt{2\pi}} \int\int \mathrm{e}^{+i\vec{\mu}\vec{\kappa}} a_f(\vec{\kappa}) d^2\vec{\kappa} \int\int a_f(\vec{\nu}) \mathrm{e}^{-i\vec{\mu}\vec{\nu}} d^2\vec{\nu} \tag{D.25}$$

$$\eta(\vec{\mu}) \;=\; k\,\sqrt{2\pi} A_f^*(\vec{\mu}) A_f(\vec{\mu}) \tag{D.26}$$

$$\eta(\vec{\mu}) \;=\; k\,\sqrt{2\pi} |A_f(\vec{\mu})|^2 \tag{D.27}$$

Parallel case

In the case of the parallel collimator configuration, the focal line height F tends to infinity:

$$\lim_{F\to\infty} \vec{r_t} \;=\; \frac{L}{(Z+L+B)} (\vec{r} - \vec{r_0}) \tag{D.28}$$

This means that there is an invariant probability of detection along the collimator plane if the distance between S and I is kept constant $\vec{r} - \vec{r_0} = K_0$. However , this phenomenon does not occur in fan or cone beam collimators because the efficiency η depends on $\vec{r_0}$ and not only on the distance vector. The response function is non stationary over the image plane.

Point source S on z-axis

For the particular case $\vec{r_0} = 0$ when the point source is located on the z-axis, the μ variable:

$$\eta(\vec{\mu}) \;=\; \frac{k}{\sqrt{2\pi}} \int\int \mathrm{e}^{-i\vec{r}\vec{\mu}} d^2\vec{r} \int\int a_f(-\vec{\sigma}) a_f(\vec{r_t} - \vec{\sigma}) d^2\vec{\sigma} \tag{D.29}$$

$$\vec{\nu} \;=\; \vec{r_t} - \vec{\sigma} \;= G\vec{r} - \vec{\sigma} \tag{D.30}$$

where the factor G is defined as:

$$G \;=\; \frac{L(F-Z)}{(F+L)(Z+L+B)} \tag{D.31}$$

and if a new change of variables is introduced:

$$d^2\vec{\nu} \;=\; G^2\; d^2\vec{r} \tag{D.32}$$

$$\eta(\vec{\mu}) \;=\; \frac{k}{G^2\sqrt{2\pi}} \int\int a_f(-\vec{\sigma}) d^2\vec{\sigma} \int\int a_f(\vec{\nu}) \mathrm{e}^{-i\vec{\mu}\frac{\vec{\nu}+\vec{\sigma}}{G}} d^2\vec{\nu} \tag{D.33}$$

$$\vec{\kappa} \;=\; -\vec{\sigma} \tag{D.34}$$

$$d^2\vec{\kappa} \;=\; d^2\vec{\sigma} \tag{D.35}$$

and then the Fourier transform of the integral is the product of conjugate Fourier transform functions:

$$\eta(\vec{\mu}) \;=\; \frac{k}{G^2\sqrt{2\pi}} \int\int \mathrm{e}^{+i\vec{\mu}\frac{\vec{\kappa}}{G}} a_f(\vec{\kappa}) d^2\vec{\kappa} \int\int a_f(\vec{\nu}) \mathrm{e}^{-i\vec{\mu}\frac{\vec{\nu}}{G}} d^2\vec{\nu} \tag{D.36}$$

$$\eta(\vec{\mu}) \;=\; k\; \frac{\sqrt{2\pi}}{G^2} A_f^*(\frac{\vec{\mu}}{G}) A_f(\frac{\vec{\mu}}{G}) \tag{D.37}$$

$$\eta(\vec{\mu}) \;=\; k\; \frac{\sqrt{2\pi}}{G^2} |A_f(\frac{\vec{\mu}}{G})|^2 \tag{D.38}$$

Example of a solution using the Metz model

In the last section the means to calculate the fluency for a point source over a collimator in the frequency domain was explained. In this section this result is applied to an example. Consider a collimator radius R:

$$a_f(\vec{\eta} - \vec{r_i'}) \;=\; a_f(-\vec{\sigma}) \;=\; 1 \;\; if \;\; |\vec{\eta} - \vec{r_i'}| \;<\; R \tag{D.39}$$

$$a_f(\vec{\eta} - \vec{r_i'}) \;=\; a_f(-\vec{\sigma}) \;= 0 \; else \tag{D.40}$$

first, we perform the transformation:

$$A_f(\vec{\mu}) = \frac{1}{\sqrt{2\pi}} \int\int \mathrm{e}^{+i\vec{\sigma}\vec{\mu}} a_f(-\vec{\sigma}) d^2\vec{\sigma} \tag{D.41}$$

$$A_f(\vec{\mu}) = \frac{1}{\sqrt{2\pi}} \int_{-R}^{R} d\vec{\sigma}_x \int_{-\sqrt{R^2-\vec{\sigma}_x^2}}^{\sqrt{R^2-\vec{\sigma}_x^2}} \mathrm{e}^{+i(\vec{\sigma}_x\vec{\mu}_x + \vec{\sigma}_y\vec{\mu}_y)} \; 1 \; d\vec{\sigma}_y \tag{D.42}$$

For this particular case, the convolution becomes the area of the overlapped circles with radii R.

$$A_f(\vec{\mu}) = \frac{1}{\sqrt{2\pi}} \int_{-R}^{R} \mathrm{e}^{+i(\vec{\sigma}_x \vec{\mu}_x)} \frac{2\cos(\vec{\mu}_y \sqrt{R^2 - \vec{\sigma}_x^2})}{\vec{\mu}_y \sqrt{R^2 - \vec{\sigma}_x^2}} d\vec{\sigma}_x \tag{D.43}$$

A function in the frequency domain (μ) is the result with a non trivial solution. This function will subsequently have to be transformed into the real domain using the two-dimensional Fourier function only by numerical methods in order to get the final solution.

$$\eta(\vec{r}; \vec{r}_0) \;=\; \mathcal{F}^{-1}(\Psi(\vec{\mu})) \;=\; k\,\sqrt{2\pi}\mathcal{F}^{-1}(|A_f(\vec{\mu})|^2) \tag{D.44}$$

It is clear that these type of models are not operative in practice because of their complex structures and their simplifying assumptions.

D.1.2 Frey model for the analytical PSF_G

The density probability function of being detected is defined as:

$$P(\vec{r}; \vec{r_0}; A) \;=\; \frac{\text{Overlapped Area}}{\text{Collimator Cell Unit Area}} \tag{D.45}$$

The probability density function per unit area is calculated using the ratio between two areas: the overlapped area —between the aperture functions on the front and back collimator plane, see Figure D.1— and the unit area —geometric cell area, see Figure D.2—. The collimator cell unit area is the minimum cell used to build the collimator array structure.

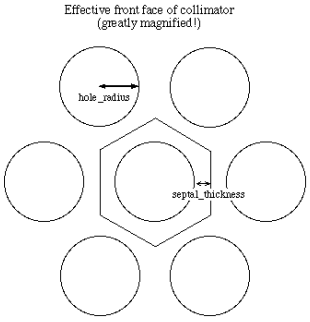

Fig. D.2: The hexagon describes the geometric unit cell of the collimator in Frey model

The geometric cell used in Frey's model presents some differences in comparison with the experimental collimator geometry:

1. The model considers round holes instead of the real hexagonal holes used in most collimators

2. This model uses a septal thickness equal to half of the septa wall —distance between two apertures— $2S_{th} = S_{wall}$. This definition is not used in the bibliography[3]

The collimator cell unit area is calculated as:

$$\text{Collimator Cell Unit Area} = 2\frac{(2R + 2S_{th})\cos(30^o)(2R + 2S_{th})}{2} = 2\sqrt{3}(R + S_{th})^2 \tag{D.46}$$

then, using the approximation $(R + S)^2 \simeq (R + S_{th})^2$, we obtain:

$$\text{Collimator Cell Unit Area} = 2\sqrt{3}(R + S)^2 \tag{D.47}$$

How do Frey et al. analytically determine the overlapped area between the two circles in a real-domain formula for a known photon direction and for a certain hole?

The solution is simple but ingenious: **using the analytical expression of the area included in the segment defined by the arc of a circle** [79] defined in equation (D.48):

$$\text{Half Overlapped Area} = \frac{1}{2}R^2(\theta - \sin(\theta)) \tag{D.48}$$

This area —represented in Figure D.3— is half of the overlapped area between two circles of the same radius:

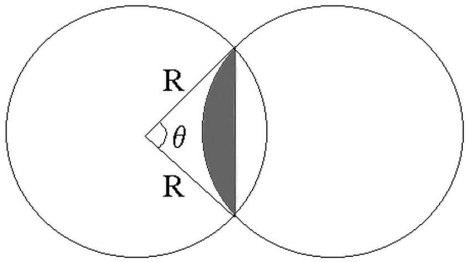

Fig. D.3: The dark area represents half of the overlapped area between two circles

This area can be calculated (in (D.49)) once the direction of the photon and the geometry of the collimator are determined as Figure D.4 shows.

[3] Nevertheless, in SimSET simulations the user may enter the standard septa thickness as in most collimators $R \gg S$, so $(R + S)^2 \simeq (R + S_{th})^2$.

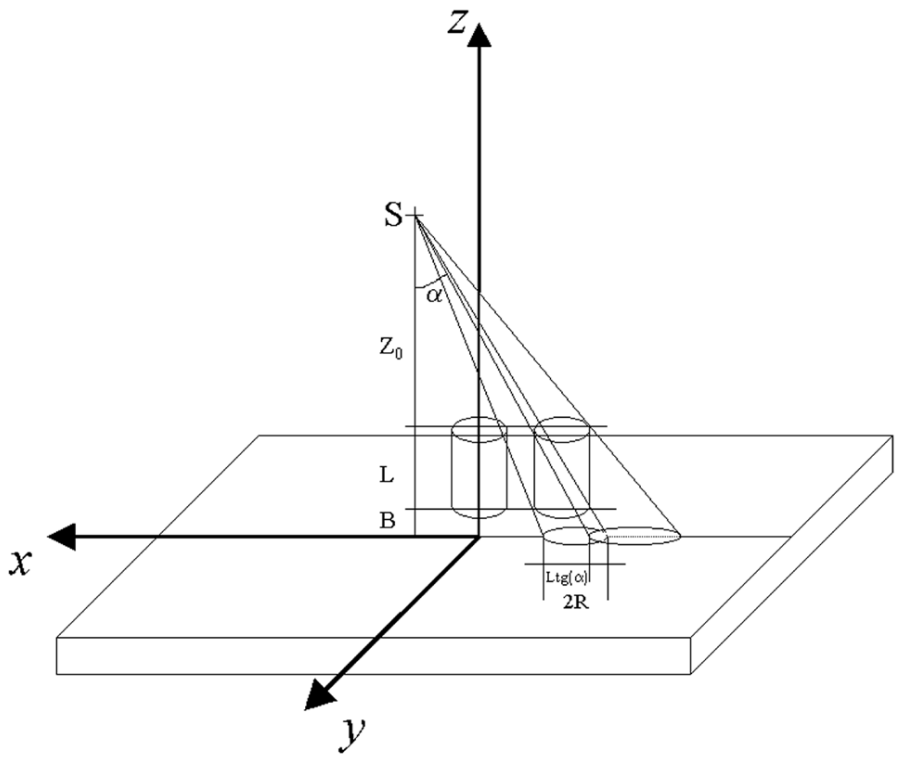

Fig. D.4: The non-overlapped distance is shown as a function of the angle of the photon and the characteristics of the hole

$$\text{Non overlapped length} \;=\; L\ \tan(\alpha) \tag{D.49}$$

where α is the direction of the photon with respect to the z-axis. Thus, the overlapped length will be the rest of the circle diameter:

$$\text{Overlapped length} \;=\; 2R - L\ \tan(\alpha) \tag{D.50}$$

Therefore, we can calculate the overlapped area[4] using (D.48) and the parameters shown in Figure D.5:

$$\cos(\frac{\theta}{2}) \;=\; \frac{R - \text{Half Overlapped Length}}{R} \;=\; \frac{R - \frac{2R - L\ \tan(\alpha)}{2}}{R} \;=\; \frac{L\ \tan(\alpha)}{2R} \tag{D.51}$$

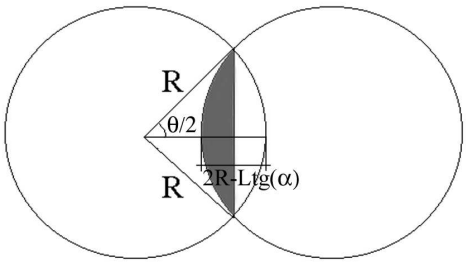

Fig. D.5: The dark area represents half of the overlapped area between two circles. The parameters used in the Frey model are illustrated.

$$\theta \;=\; 2arcos(\frac{L\ \tan(\alpha)}{2R}) \tag{D.52}$$

$$sin(\theta) \;=\; 2\sin(\frac{\theta}{2})\cos(\frac{\theta}{2}) \;=\; 2\cos(\frac{\theta}{2})\sqrt{1 - (\cos(\frac{\theta}{2}))^2} \tag{D.53}$$

Then, the overlapped area will be twice the half overlapped area calculated with the analytical formula:

$$\text{Overlapped Area} \;=\; 2\frac{1}{2}R^2(\theta - sin(\theta)) \tag{D.54}$$

[4] The $tg(\alpha) = \frac{2R}{L}$ value limits the maximum "acceptance angle" of a parallel collimator. When the $\cos(\theta)$ equals 1 and $\theta = 0$.

$$\text{Overlapped Area} \;=\; R^2(2arcos(\frac{L\ \tan(\alpha)}{2R}) - 2\frac{L\ \tan(\alpha)}{2R}\sqrt{1-(\frac{L\ \tan(\alpha)}{2R})^2} \quad \text{(D.55)}$$

If we change the variables $\|\vec{r_0}\| = L\ tg(\alpha)$, the overlapped area for a certain photon direction remains:

$$\text{Overlapped Area} \;=\; 2arccos(\frac{\|\vec{r_0}\|}{2R}) - 2\frac{\|\vec{r_0}\|}{2R}\sqrt{1-\frac{\|\vec{r_0}\|^2}{4R^2}} \quad \text{(D.56)}$$

and using the expressions in (D.56) and (D.47), the density probability function of Frey's model becomes the formula that was presented at the beginning of this section ((D.45)):

$$P(\vec{r};\vec{r_0};A) \;=\; \frac{\text{Overlapped Area}}{\text{Collimator Cell Unit Area}} \;= \frac{2\arccos(\frac{\|\vec{r_0}\|}{2R}) - 2\frac{\|\vec{r_0}\|}{2R}\sqrt{1-\frac{\|\vec{r_0}\|^2}{4R^2}}}{2\sqrt{3}(R+S)^2} \quad \text{(D.57)}$$

For convergent beam collimators an extension of the previous density probability function is presented. In the case of the fan beam collimator we have to introduce the elongation factor defined as:

$$\gamma(\vec{r}^{\,\prime}) \;=\; \frac{1}{\cos(\vartheta)} \;= \frac{\sqrt{(F+L+B)^2+|\vec{r}^{\,\prime}|^2}}{(F+L+B)} \quad \text{(D.58)}$$

where ϑ is the angle between each pin used to build the fan beam collimator holes and the normal to the front plane collimator. The vector $\vec{r}^{\,\prime}$, which is the position of each hole center, is obtained with the elongation factor and the variable $\vec{r_0}$:

$$\frac{\vec{r_0}}{\gamma(\vec{r}^{\,\prime})} \quad \text{(D.59)}$$

In the fan beam collimator the radius and septa thickness of the border collimator hole is 20% larger than the central hole.

D.1.3 Pareto model for PSF_G

Fluency of photons at point $I = (\vec{r}, 0) = P(x, y, -L-B)$ on the image plane for a given point source located at $S = (\vec{r_0}, L+B+Z) = P(x_0, y_0, z_0)$ was defined in the expression obtained in Section 6.2.

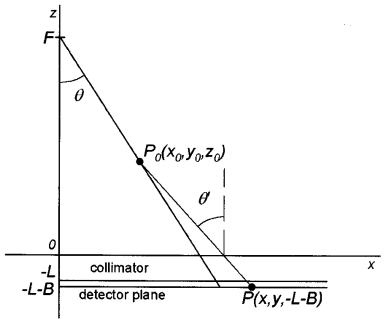

Fig. D.6: with the parameters needed in our PSF_T model.

The ray-tracing technique consists of defining a new "aperture hole function" $A(\vec{r}, \vec{r_0}, Z+L+B) = 1$. If the optical ray reaches any bin or pixel detector, the aperture function has the value 1. Otherwise, it is 0.

$$A(\vec{r}, \vec{r_0}, Z+L+B) \;=\; \int\int a_b(\vec{r}, \vec{r_i'}, \vec{r_0}) a_f(\vec{r}, \vec{r_i'}, \vec{r_0}) d^2\vec{r_i'} \tag{D.60}$$

Each detector bin is a discrete image plane. This plane is divided into N pixels with area Δ. Each pixel is sampled from its center to the source location through the collimator. The sampling covers all the detector surface and accumulates the "detected" number of optical rays ($A(\vec{r}, \vec{r_0}, Z+L+B)$). The pixel area resolution Δ determines the accuracy of the sensitivity estimate η which is:

$$\eta(\vec{r}, \vec{r_0}) \;=\; \frac{(L+B+Z)}{4\pi(|\vec{r_0}-\vec{r}|^2+(L+B+Z)^2)^{\frac{3}{2}}} A(\vec{r}, \vec{r_0}, Z+L+B)\;\Delta \tag{D.61}$$

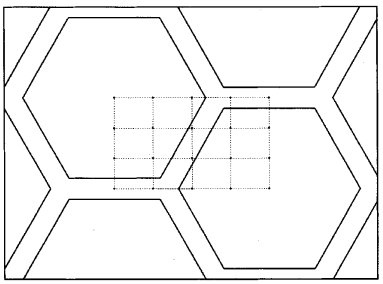

Fig. D.7: A detailed part of the collimator where optical rays are sampled along the discrete pixel areas Δ

In other words, the expression is:

$$\eta = \sum_{\vec{r_i} \in \Delta_i} \frac{cos(\theta_i)}{4\pi R_i^2} A(\vec{r}, \vec{r_0}, Z + L + B)\ \Delta \tag{D.62}$$

Where R_i is the distance between the point source and each image point of the whole front plane collimator and the dot product between each photon ray and the normal plane vector results in $cos(\theta_i)$.

D.2 The Probability Density Function change in Monte Carlo

This section shows an important operation in Monte Carlo techniques: the PDF variable change in order to reduce the variance of the simulation. A detailed example for simulating photons in a reduced range of angles is described[5].

In a Monte Carlo simulation, the emission angle of the photons is not isotropic. The photon directions should be oversampled in a certain range close to the 0^o direction. Thus, this implies that the "real-photon" history associated with the track of a particular photon must be reflected in the weight of the photon because it is not sorted isotropically. This deviation is maintained including a new weight W which relates to the ratio between the "real-probability" of the photon (p_r) and the new probability ($p_w^{'}$) assigned in order to accelerate the simulation with photons exiting with a certain Ω solid angle, that is:

$$p_r \ = \ w p_w^{'} \tag{D.63}$$

The w factor is the Monte Carlo weight in order to assign a "real" value to each history using variance reduction techniques as was explained in chapter 3. The probability density function has to be normalized in the whole domain:

$$\int_\Omega p(\Omega) d\Omega \ = \ 1 \tag{D.64}$$

$$p(\Omega) \ = \ \frac{1}{\int_{4\pi} d\Omega} \ = \ \frac{1}{4\pi} \tag{D.65}$$

Similarly, if the emission is isotropic, we can describe the same equation ((D.64)) with the variables φ, ϑ:

$$\int_\Omega p(\Omega) d\Omega \ = \ \int_\varphi p(\varphi) d\varphi \int_{cos(\vartheta)} p(\cos(\vartheta)) d\cos(\vartheta) \ = \ 1 \tag{D.66}$$

[5] This change of PDF was applied in the PSF_T Monte Carlo code

As each variable has to be normalized,

$$\int_{\varphi} p(\varphi) d\varphi \;=\; 1 \tag{D.67}$$

$$p(\varphi) = \frac{1}{\int_0^{2\pi} d\varphi} \;=\; \frac{1}{2\pi} \tag{D.68}$$

and similarly:

$$\int_{cos(\vartheta)} p(\cos(\vartheta)) d\cos(\vartheta) \;=\; 1 \tag{D.69}$$

$$p(\cos(\vartheta)) \;=\; \frac{1}{\int_{-1}^{1} d\cos(\vartheta)} \;=\; \frac{1}{2} \tag{D.70}$$

If we restrict the isotropic decay in a certain range of angles to the ϑ variable (from α_{min} to α_{max}) :

$$p_w \;=\; \frac{1}{\int_0^{2\pi} d\varphi} \frac{1}{\int_{cos(\alpha_{min})}^{cos(\alpha_{max})} d\cos(\vartheta)} \;=\; \frac{1}{2\pi} \frac{1}{\cos(\alpha_{max}) - \cos(\alpha_{min})} \tag{D.71}$$

Thus, applying equation (D.63) the final value for the weight W is:

$$W \;=\; \frac{\frac{1}{4\pi}}{\frac{1}{2\pi} \frac{1}{(\cos(\alpha_{max}) - \cos(\alpha_{min}))}} \;=\; \frac{\cos(\alpha_{max}) - \cos(\alpha_{min})}{2} \tag{D.72}$$

Another case of interest is the calculation of the new PDF based on the relationship between the two variables. In this Monte Carlo simulation, the emission angle of the photons is not isotropic. The photon directions should be oversampled in a certain range close to the 0^o direction. In this Monte Carlo simulation, in order to improve the sensitivity near the $\vartheta = 0$ a typical change for the probability density function is,

$$\vartheta \;=\; \cos(\vartheta) \tag{D.73}$$

The equation to be maintained is:

$$p'(\cos(\vartheta)) d\cos(\vartheta) \;=\; p'(\vartheta) d\vartheta \tag{D.74}$$

Thus:

$$p'(\cos(\vartheta)) \;=\; |\frac{d\vartheta}{d\cos(\vartheta)}|p'(\vartheta) \tag{D.75}$$

It is simply calculated that:

$$|\frac{d\vartheta}{d\cos(\vartheta)}| \;=\; \frac{1}{sin(\vartheta)} \tag{D.76}$$

$$p'(\cos(\vartheta)) \;=\; \frac{1}{sin(\vartheta)}\frac{1}{\pi} \tag{D.77}$$

This new density probability function should be normalized:

$$p(\vartheta) \;=\; \frac{1}{\int_0^\pi \vartheta} \;=\; \frac{1}{\pi} \tag{D.78}$$

$$\int_{-1}^{1} p'(\cos(\vartheta))d\cos(\vartheta) \;=\; 1 \tag{D.79}$$

$$\frac{1}{\pi}\int_{-1}^{1}\frac{1}{sin(\vartheta)}d\cos(\vartheta) \tag{D.80}$$

by changing the variable $|dcos(\vartheta)| = sin(\vartheta)d\vartheta$, the integration limits change to:

$$\frac{1}{\pi}\int_{\frac{-\pi}{2}}^{\frac{\pi}{2}}\frac{1}{sin(\vartheta)}sin(\vartheta)d\vartheta \;=\; 1 \tag{D.81}$$

The weight using (D.63) associated with the new probability density function is:

$$p'(\cos(\vartheta)) \;=\; \frac{1}{sin(\vartheta)}p(\vartheta) \tag{D.82}$$

Then,

$$wp_w^{'} \;=\; p_r \tag{D.83}$$

The real probability for isotropic emission is:

$$p_r \;=\; p(\cos(\vartheta)) = \;\frac{1}{2} \tag{D.84}$$

and the new probability density function which is not isotropic:

$$p_w \;=\; p'(\cos(\vartheta)) \;=\; \frac{1}{sin(\vartheta)}\frac{1}{\pi} \tag{D.85}$$

Then:

$$W \;=\; \frac{p_r}{p'_w} \;=\; \frac{\pi}{2sin(\vartheta)} \tag{D.86}$$

E. THE P3D-OSEM ALGORITHM AND SCATTERING CORRECTION METHODS

E.1 Full 3D Reconstruction Algorithm: P3D–OSEM

E.1.1 Iterative Reconstruction algorithms

The aim of tomographic reconstruction is to obtain cross-sections of an object from projections of that object. Two different approaches are commonly used for SPECT reconstruction. Until recently, Filtered Back Projection (FBP) was the universal method because of its simplicity and speed. As soon as computations burden were speeded with advanced computers, a more accurate technique was used: Iterative reconstruction algorithms.

In iterative algorithms, using an initial estimate of the activity distribution (image s_i^0), estimated projection data are generated by means of a forward projector ($\sum_l t_{lj} s_l^0$). These calculated projections are compared with the measured projections (p_j). On the basis of this comparison, one can obtain a better estimate of the image using an update step (s_i^1). This process of forward projection, comparison and updating can be iterated n times until an acceptable image is obtained (s_i^n). The model of forward projection is represented by the transition matrix (t_{ij}) which is used in the iterative algorithm. The more accurate this transition matrix is modelled, the better the agreement will be between the estimated images and the real activity distribution.

Iterative reconstruction algorithms based on maximum-likelihood expectation-maximization methods (MLE-EM) [77, 49] are attractive because they place non-negativity constraints on the reconstructions, they have attractive noise properties and they enable Poisson noise to be accounted for in the projection data. The ML-EM algorithm updates all image elements s_i of the estimated image at iteration $k+1$ according to:

$$s_i^{k+1} = \frac{s_i^k}{\sum_j t_{ij}} \sum_j \frac{t_{ij} p_j}{\sum_l t_{lj} s_l^k} \tag{E.1}$$

where s_i^k represents the unknown and the input data are the transition matrix ($T = [t_{ij}]$) and the measured projection set ($P = [p_j]$). Furthermore, realistic models that include effects of camera blurring and attenuation can be incorporated into the transition

matrix during reconstruction. The elements of a matrix column represents the probabilities of photons emitted from a single voxel to be detected in each pixel of the projection image. This part of the matrix closely represents an attenuated point spread function (PSF). The exact matrix (or a complete set of attenuated PSFs) depends on acquisition parameters, the gamma camera system, and the density distribution of the patient.

E.1.2 The OS-EM algorithm

In order to render ML-EM fast enough to be used in a clinical setting, the scheme is often accelerated, for example using block iterative methods such as the Ordered Subsets Expectation Maximization (OS-EM) algorithm of Hudson and Larkin [39]. OS-EM involves grouping projection data into an ordered sequence of Ω subsets:

$$p_j \;=\; p^1 \bigcup p^2 \cdots \bigcup p^{\Omega} \tag{E.2}$$

The EM algorithm is then applied to each subset[1] ω taking into account the results of $\omega - 1$ at the same iteration number k:

$$s_i^{k(\omega)} \;=\; \frac{s_i^{k(\omega-1)}}{\sum_j t_{ij}} \sum_j \frac{t_{ij} p_j^{\omega-1}}{\sum_l t_{lj} s_l^{k(\omega-1)}} \tag{E.3}$$

and the result is used as the starting estimate for processing the next image estimate s_i^{k+1}.

Ordering of subsets should be established in such a way that each subset ω includes the most independent information possible. It has been shown that OS-EM can reach acceleration factors that are close to the number of subsets Ω used [39, 44], while achieving image quality that is similar to standard ML-EM.

E.1.3 Description of P3D-OSEM

Despite the fact that physical effects occur both within and across transaxial planes, most iterative methods used to date treat each transaxial plane independently due to computational considerations. One would expect, however, improved image quality from the more accurate three-dimensional (3D) reconstruction methods —those that model in-plane and cross-plane effects— compared with 2D methods [35].

We based our P3D-OSEM reconstruction algorithm on using OS-EM iterative algorithms. The P3D-OSEM was an upgraded version of the 2D algorithm presented by

[1] The image values are initialized with the mean value of the projection data set $s_i^0 = \bar{p_j}$

Falcon [27]. In the P3D–OSEM algorithm each factor is a well-understood physical phenomenon, and therefore corrections are included for each of the image degrading effects. The transition matrix includes full 3D PSF and attenuation factors:

1. The correction of collimator blurring by using accurate models of spatially-dependent camera blurring during iterative reconstruction improves signal-to-noise ratio (SNR) and resolution [46, 82, 88]. The PSF factor consists of determining the contribution of each voxel of the object to each bin detector or projection pixel. This factor corresponds to the integral of the full 3D PSF in the projection pixel. The 3D PSF function is the PSF_T model (see Chapter 6) for both parallel and fan beam collimators.

The tails of the Gaussian PSF_T beyond 3σ from the center were truncated to zero in order to reduce the size of the transition matrix. A minimum weight value $min(t_{ij})$ of 0.0003 was chosen[2] and all the matrix elements $t_{ij} \leq min(t_{ij})$ below this threshold were discarded in order to avoid an excessive amount of small weights. The total PSF volume over the whole FOV was normalized depending on the source-to-collimator distance and the aperture angle from the central ray.

2. The attenuation factor was calculated by ray tracing following the proposal of Siddon et al. [78]. The attenuation factor included the fraction of transported photons from the center of each voxel in the image to the center of each pixel of the projection. The track-length of the ray in each voxel was determined by the intersection between the parametric equation of the ray and the equations which define each plane. The parametric values were sorted to determine the order of the crossed voxels. The distances were calculated by simple substraction of the consecutive parametric values because an unitary vector was used in order to define the ray equation.

Both factors were calculated separately and multiplied afterwards. The result is stored using compact design techniques, thus avoiding the increase of matrix size [14]. The standard 3D transition matrix dimension equals the number of voxels multiplied by the number of detector angles and by the number of projection bins containing non-zero values of the response model. Its elements have a four-byte, floating-point format. A common 128×128 activity object of 12 slices projected onto 128 bins located at 120 angles represents a "standard" transition matrix size of 5 Gb. To avoid surpassing the maximum RAM memory available[3], the total transition matrix is split into the same number of (P3D-OSEM) submatrices as the number of ordered subsets.

[2] This parameter is an user-defined variable which has to be calculated previously. The value has to be determined between the maximum and minimum weight of the transition matrix. It depends on geometrical data and collimator/detector configurations of each SPECT study.

[3] The maximum RAM memory available depends obviously on the computer size. Our different computers had a RAM memory size between 0.5 and 2 Gigabytes

Each P3D-OSEM submatrix includes all the object contributions to each projection subset. The attenuation and detector response factors are pre-computed in each submatrix. At each iteration step, the corresponding submatrix is loaded, the subset of projections is reconstructed and finally it is unloaded. In this way the transition matrix is reduced and it only includes information related to the projection angles included in each subset. Although reading the submatrix at each subset is time-consuming, this strategy is a trade-off between RAM memory capacities and processing times. Once the iteration is performed all the submatrix have been used. The amount of memory is reduced linearly with the number of subsets.

E.2 Scattering correction methods

There are different methods for scattering correction in reconstruction algorithms. The scatter effect in the final image is about 15% to 40% of the total image, thus it has to be corrected in order to obtain quantification results. Nowadays this subject is an intensive field of research in SPECT techniques [57, 16]. Scattering phenomena in the object and in the collimator/detector system significantly affects the quantification results in neurotransmission SPECT studies [63]. Scattering in the collimator produced by low energy photons of ^{99m}Tc-TRODAT agents may be neglected [18]. Thus, the scattering models should focus on scatter interactions in the object for ^{99m}Tc-TRODAT brain neurotransmission studies. There are different approaches to the modelling of scatter but its stochastic behaviour difficult its modelling.

Monte Carlo simulation (MC) is the most general method for detailed modelling of scatter although it implies long computation times. We modelled the scattering effect by simulating the reconstructed image of the full P3D-OSEM algorithm with the modified SimSET (see Chapter 6) stochastic virtual phantom MC simulator. The modified SimSET accelerated the simulation step.

E.2.1 Analytical correction methods

Nowadays Monte Carlo simulation (MC) is the most general method for detailed scattering modelling. The problem associated with Monte Carlo-based statistical SPECT reconstruction approaches is the prohibitively long computation times and excessive computer memory requirements [7]. However, at present hardware architectures such as clusters and multiprocessor computers are available. They allow Monte Carlo simulations to be parallelized in order to speed-up the process.

In order to simplify and accelerate the scatter degradation, deterministic models were derived from empirical data such as Dual window, Triple Energy Window, TDCS, etc. Among the different deterministic models, there are:

Triple Energy Window (TEW)

At present, a much-used scatter correction method is the deterministic Triple Energy Window (TEW) method which includes acquisition data in triple-energy windows of the gamma camera [60, 40]. This method consists of estimating scatter photons in each projection bin from the detected photons in two additional energy windows W_1^{sc}, W_2^{sc} each 4 keV on either side of the central window. The counts of the central window are then corrected by the lateral windows.

$$p_j^{sc} \;=\; p_j - (\tau\ p_j^1 - \upsilon p_j^2) \tag{E.4}$$

However, due to the small size of the windows used in this technique, noise can be substantially increased in the corrected scatter data and accurate results are not always obtained. As an advantage, TEW neither requires careful instrument-dependent calibration nor need a transmission scan.

Transmission Dependent Convolution Substraction (TDCS)

A second class of methods, which includes acquisition data of a transmission scan (TCT-ECT), is the Transmission Dependent Convolution Substraction (TDCS) technique [55, 57]. The scatter is estimated deterministically by first convolving the observed photopeak projection data p_j, with a radially symmetric mono-exponential scatter function, SC, to reduce variation of scatter with depth and provide an initial estimation of scatter p_j^{sc}:

$$p_j^{sc} \;= p_j \otimes SC(r) \;=\; p_j \otimes \zeta \exp^{-\kappa r} \tag{E.5}$$

Pixel-by-pixel scatter fraction values $k(x, y)$ were estimated for emission projections from the transmission projections as follows:

$$k(x,y) \;=\; 1 - \frac{1}{A - Bt(x,y)^{\frac{\beta}{2}}} \tag{E.6}$$

where $t(x, y)$ is the transmission factor at detector bin position (pixel (x, y)) and A, B and β are constants. The corrected scatter data p'_j are then given by the difference of the projection and the estimated scatter fraction pixel by pixel:

$$p'_j(x,y) \;= p_j(x,y) - k(x,y) p_j^{sc}(x,y) \tag{E.7}$$

E.2.2 Monte Carlo methods

Monte Carlo methods can readily handle media of non-uniform density and large-angle scattering. To make the —notoriously slow— MC simulation feasible for scatter correction in SPECT, acceleration methods using variance reduction techniques (VRTs) are often applied [37]. The most common VRTs are forced detection (FD) to increase photon yield on the detector and importance sampling (IS) to sort photon directions at locations where it is more probable to count the particle. VRTs that have been proposed more recently include photon tracking combined with Convolved Point Spread Functions (CPSF) which allow a two-fold extra acceleration. These methods have been found to be accurate for scatter simulations in the photo-peak window and they are presented in this thesis. When a combination of these VRTs is used, MC becomes computational feasible for full 3D scatter correction in routine clinical iterative image reconstruction.

Different methods of scatter correction can be applied using MC tools:

1. The Inverse Monte Carlo (IMOC) method computes the entire transition matrix T_{ij}. MC provides solutions to the photon transport equation for SPECT detection from a unit source activity $s_i = 1$ in each reconstruction source voxel [28, 29]. In the photon transport equation, scatter is included as well as attenuation and collimator blurring by modelling PSF functions and attenuation factors. The inputs are the physical characteristics of the acquisition apparatus such as energy window setting, system energy and spatial resolution, radius of rotation and an attenuation map of the body and its contours. Due to photon cross-talk between slices, caused by collimator blurring and scattering, full 3D SPECT reconstruction (instead of slice-by-slice (2D) reconstruction) is required for optimal image quality [9]. Unfortunately, hundreds of Giga-bytes up or even several Tera-bytes of memory are required to store the complete non-sparse transition matrix when the full 3D MC matrix approach is used, and it can take several months to generate the full matrix on a state-of-the-art workstation. In addition, the procedure has to be repeated for each patient.

2. Slab Derived Scatter Estimation (SDSE) first calculates and stores the scatter responses in tables of point sources behind slabs for a range of thicknesses, and then tunes these responses to various object shapes with uniform density [8, 31]. A table occupying only a few megabytes of memory is sufficient to represent this scatter model for full 3D reconstruction [9]. A full 3D reconstruction of a ^{99m}Tc cardiac study based on SDSE can be performed in only a few minutes on a state-of-the-art single processor workstation. A disadvantage of SDSE compared with matrices generated by IMOC techniques is that it only includes the first-order Compton scattering and the photoelectric effect, so it neglects multiple-order Compton scattering, coherent scatter and high-energy scatter contamination (i.e. in ^{123}I for example). The scatter responses are calculated by specific Monte Carlo techniques such as the

Utrecht Monte Carlo System (UMCS) [21] which uses a three-dimensional source emission-distribution (activity image), a mass density distribution (attenuation image) and the geometry and characteristics of the SPECT system. These scatter responses are used in the probability density functions (PDFs) describing the physics of photon transport, including emission, scatter and detection processes.

3. The scatter estimate through an accelerated Monte Carlo virtual phantom simulator. Some authors have developed fast Monte Carlo simulations with precalculated scatter responses [7] in order to accelerate the simulation of projections. A combined 3D reconstruction with a fast MC simulator is used. Following this strategy this work presents a combined MC-3D full reconstruction algorithm with an accelerated MC simulator which obtains a scatter estimate model.

F. GLOSSARY

$\sum w$ Sum of Weights
$\sum w^2$ Sum of Squared Weights
1D one-dimensional
2D two-dimensional
3D three-dimensional
ART Algebraic Reconstruction Techniques
CFOM Computation Figure of Merit
CT Computed Tomography
FBP Filtered Back Projection
FD Forced Detection
FOM Figures Of Merit
FOV Field of View
FWHM Full Width at Half Maximum
FWTM Full Width at Tenth Maximum
IS Importance Sampling
LEGP Low Energy General Purpose (collimator)
Lucite geometric cylinder (phantom)
MBq Megabecquerel = 27.03 μCi
MC Monte Carlo
MCAT Mathematical Cardiac Antromorphic Thorax (phantom)
MLE-OSEMMaximum Likelihood Estimator Ordered Subsets
MRI Magnetic Ressonance Imaging
NaI sodium iodine (crystal)
Nh Number of Histories
PDF Probability Distribution Function
PET Positron Emission Tomography
PHG Photon History Generator
PSF Point Source Function
Pb Lead
Pixel bin detector image element
QF Quality Factor
ROI Region of Interest

SMFC Scatter Monte carlo Feedback Correction
SNR Signal to Noise Ratio
SPECT Single Photon Emission Computed Tomography
SimSET Simulation System for Emission Tomography
VRT Variance Reduction Technique
Voxel object source element

7. AGRAïMENTS

En primer lloc vull ressaltar que aquesta tesi és el resultat d'una col.laboració entre grups de diferents Universitats. Per tant, vull fer un agraïment especial a l'esforç i la dedicació del Dr. Domènec Ros com a director de tesi per part de la Universitat de Barcelona i dels Dr. Francisco Calviño i Dr. Josep Sempau per part de la Universitat Politècnica de Catalunya perquè en tot moment han aportat la seva experiència i col.laboració amb aquest treball.

Aquesta tesi és el resultat del treball en equip desenvolupat durant els darrers 5 anys. Insisteixo en el fet del treball conjunt ja que sense la contribució de cadascú, no s'hagués arribat fins aquí. En l'equip d'investigació han participat els Dr. Carles Falcón, Dr. Xavier Pavía, Dra. Deborah Pareto i Dr. Santiago Bullich. Vull ressaltar també les contribucions rellevants del Dr. Enric Jané, Dr. Ignasi Juvells i el José Tamajón que han participat en diversos treballs de la tesi. Una menció de reconeixement cap al grup d'investigació de la Universtitat de Barcelona (Francesc Salvat, José María Sánchez-Varea i Josep Sempau) que ens van aconsellar en la utilització del codi PENELOPE. Així com al grup d'investigació de Seattle (Robert Harrison, Tom Lewellen, David Haynor i Mitch Kaplan) que van compartir amb mi els seus coneixements a través del codi de SimSET.

Finalment, unes paraules d'agraïment als familiars i amics que m'han donat el seu suport i els ànims per seguir endavant i arribar fins aquí. Molt especialment a la Caroline, a l'Eduard i als meus pares.

Moltes gràcies.

Barcelona, 8 de Juny del 2003

BIBLIOGRAFIA

[1] P. D. Acton, S.-R. Choi, K. Plössl, and H. F. L. Kung, *Quantification of dopamine transporters in the mouse brain using ultra-high resolution single-photon emission tomography*, Eur J Nucl Med, 29 (2002), pp. 691 – 698.

[2] H. O. Anger, *Scintillation camera*, Rev. Sci. Instru., 29 (1958), pp. 27 – 33.

[3] J. Baro, M. Roteta, J. M. Fernandez-Varea, and F. Salvat, *Analytical cross sections for Monte Carlo simulation of photon transport*, Radiat. Phys. Chem., 44 (1994), pp. 531 – 552.

[4] J. Baro, J. Sempau, J. M. Fernandez-Varea, and F. Salvat, *An algorithm for Monte Carlo simulation of the penetration and energy loss of electrons and positrons in matter*, Nucl. Instrum. and Meth., B100 (1995), pp. 31 – 46.

[5] D. Bax, *Hieronymus Bosch, His Picture-writing Deciphered* , vol. I, Rotterdam, 1979.

[6] R. N. Beck and L. D. Redtung, *Collimator design using ray-tracing techniques*, IEEE Trans. Nucl. Sci., NS-32 (1985), pp. 865 – 869.

[7] F. J. Beekman, H. W. A. M. de Jong, and S. van Geloven, *Efficient Fully 3-D Iterative SPECT Reconstruction With Monte Carlo-Based Scatter Compensation*, IEEE Trans. Med. Imag., 21 (2002), pp. 867 – 877.

[8] F. J. Beekman, E. G. J. Eijkman, M. A. Viergever, G. F. Borm, and E. T. P. Slijpen, *Object Shape Dependent PSF Model for SPECT imaging*, IEEE Trans. Nuc. Sci., 40 (1993), pp. 31 – 39.

[9] F. J. Beekman, C. Kamphuis, and M. A. Viergever, *Improved Quantitation in SPECT Imaging Using Fully 3D Iterative Spatially Variant Scatter Compensation*, IEEE Trans. Med. Imag., 15 (1996), pp. 491 – 499.

[10] M. J. Berger and J. H. Hubbell, *National Bureau of Standards*, Report NBSIR, 87-3797 Wasington (1987).

[11] A. F. Bielajew, *Fundamentals of the Monte Carlo method for neutral and charged particle transport*, vol. 1, University of Michigan, 1st ed., 2001.

[12] M. H. Bourguignon, E. K. J. Pauwels, C. Loc, and B. Maziere, *Iodine-123 labelled radiopharmaceuticals and single-photon emission tomography: a natural liason*, Eur. J. Nucl. Med., 24 (1997), pp. 331 – 344.

[13] J. F. Briesmeister, *MCNP-A General Monte Carlo N-Particle Transport Code Version 4B*, Los Alamos National Laboratory, Report LA-12625-M (1993).

[14] G. Brozolo and M. Vitaletti, *Conjugate Gradient Subroutines for the IBM 3090 Vector Facility*, IBM J. Res. Develop., 33 (1989), pp. 125 – 135.

[15] S. Bullich, *Procesado de estudios de SPECT cardiaco: cuantificacion de la perfusion y de la funcion cardiaca*, PhD thesis, Unitat de Biofísica i Bioenginyeria. Dpt. Ciencies Fisiologiques I. Facultat de Medicina. Universitat de Barcelona, 2002.

[16] I. Buvat, M. Rodriguez-Villafuerte, A. Todd-Pokropek, H. Benali, and R. D. Paola, *Comparative assessment of nine scatter correction methods based on sepctral analysis using Monte Carlo simulations*, J. Nucl. Med., 36(2) (1995), pp. 1476 – 1496.

[17] A. Cot, D. Ros, F. Calviño, and J. Pavía, *Simulació de MonteCarlo en SPECT*, Proceedings XV Jornades Científiques de la Mediterrània, 1 (1999), p. 8.

[18] A. Cot, J. Sempau, D. Pareto, S. Bullich, J. Pavía, F. Calviño, and D. Ros, *Evaluation of the Geometric, Scatter, and Septal Penetration Components in Fan-Beam Collimators Using Monte Carlo Simulation*, Trans. Nuc. Sci., 49 (2002), pp. 12 – 16.

[19] ——, *Quantification of contamination by high-energy gamma rays in ^{123}I brain SPECT imaging using Monte Carlo simulation*, Phys. Med. Biol., (submitted) (2003).

[20] G. C. de Buffon, *Essai d'arithmètique morale*, vol. 4, Supplément à l'Histoire Naturelle, 1777.

[21] H. W. A. M. de Jong, E. T. P. Slijpen, and F. J. Beekman, *Utrecht Monte Carlo System for SPECT*, Tech. Report 99-1 Nuclear Medicine Physics Group, Utrecht University Hospital, (1999).

[22] Y. K. Dewaraja, M. Ljungberg, and K. F. Koral, *Characterization of scatter and penetration using Monte Carlo simulation in 131I imaging*, J. Nucl. Med., 41(1) (2000), pp. 123 – 130.

[23] A. A. Dobbeleir, A. E. Hambÿe, and P. R. Franken, *Influence of high-energy photons on the spectrum of iodine-123 with low- and medium-energy collimators: consequences for imaging with iodine-123 labelled compounds in clinical practice*, Eur. J. Nucl. Med., 26 (1999), pp. 655 – 658.

[24] M. P. Ekstrom, *Digital Image Processing Techniques*, vol. I, Academic Press, Inc., 1984.

[25] G. E. Fakhri, P. Maksud, M. F. Kijewski, R. E. Zimmerman, and S. C. Moore, *Quantitative simultaneous Tc-99m/I-123 SPECT: Design study and validation with Monte Carlo simulations and physical acquisitions*, IEEE Trans. Nucl. Sci., 49 (2002), pp. 2315 – 2321.

[26] G. E. Fakhri, S. C. Moore, P. Maksud, A. Aurengo, and M. F. Kijewski, *Absolute Activity Quantitation in Simultaneous 123I/99mTc Brain SPECT*, J. Nucl. Med., 42 (2001), pp. 300 – 308.

[27] C. Falcon, *Métodos iterativos de reconstrucción tomográfica en SPECT*, PhD thesis, Unitat de Biofísica i Bioenginyeria. Dpt. Ciencies Fisiologiques I. Facultat de Medicina. Universitat de Barcelona, 1999.

[28] C. E. Floyd, R. J. Jaszczak, K. L. Greer, and R. E. Coleman, *Inverse Monte Carlo: a unified reconstruction algrithm for SPECT*, IEEE Trans. Nuc. Sci., 32 (1985), pp. 779 – 786.

[29] ——, *Inverse Monte Carlo as an unified reconstruction algorithm for ECT*, J. Nucl. Med., 27 (1986), pp. 1577 – 1585.

[30] A. R. Formiconi, *Geometrical response of multihole collimators*, Phys. Med. Biol., 43 (1998), pp. 3359 – 3379.

[31] E. C. Frey and B. M. Tsui, *A Practical Method for Incorporating Scatter in a Projector-Backprojector for Accurate Scatter Compensation in SPECT*, IEEE Trans. Nuc. Sci., 40 (1993), pp. 1107 – 1116.

[32] E. C. Frey, B. M. W. Tsui, and G. T. Gullberg, *Improved estimation of the detector response function for converging beam collimators*, Phys. Med. Biol., 43 (1998), pp. 941 – 950.

[33] K. A. Frey, *Can SPET imaging of dopamine uptake sites replace PET imaging in Parkinson's disease?*, Eur. J. Nucl. Med., DOI 10.1007/s00259-002-0815-4 (2002).

[34] P. Gantet, J. P. Esquerré, B. Danet, and R. Guiraud, *A simulation method for studying scintillation camera collimators*, Phys. Med. Biol., 35 (1990), pp. 659 – 669.

[35] D. R. Gilland, R. J. Jaszczak, H. Wang, T. G. Turkington, K. L. Greer, and R. E. Coleman, *A 3D model of non-uniformattenuation and detector response for efficient iterative reconstruction in SPECT*, Phys. Med. Biol., 39 (1994), pp. 547 – 561.

[36] R. L. Harrison, S. Vannoy, and T. Lewellen, *http://depts.washington.edu/∼simset/html/simset_main.html*, (1998).

[37] D. R. Haynor, R. L. Harrison, and T. K. Lewellen, *The use of importance sampling techniques to improve the efficiency of photon tracking in emission tomography simulations*, Med Phys Biol, 18 (1991), pp. 990 – 1001.

[38] D. R. Haynor, R. L. Harrison, T. K. Lewellen, A. Bice, C. P. Anson, S. B. Gillispie, and R. S. Miyaoka, *Improving the efficiency of emission tomography simulations using variance reduction techniques* , IEEE Trans. Nucl. Sci., 37 (1990), pp. 749 – 753.

[39] H. M. Hudson and R. S. Larkin, *Accelerated image reconstruction using ordered subsets of projection data*, IEEE Trans. Med. Imag., 13 (1994), pp. 601 – 609.

[40] T. Ichihara, K. Ogawa, N. Motomura, A. Kubo, and S. Hashimoto, *Compton scatter compensation using the triple-energy window method for single- and dual-isotope SPECT*, J. Nucl. Med., 34 (1993), pp. 2216 – 2221.

[41] K. A. Jellinger, *Neurodegenerative disorders with extrapyramidal features: a neuropathological overiew*, J. Neural Transm., 46 (1995), pp. 33 – 57.

[42] B. Johannsen and H. J. Pietzsch, *Development of technetium-99m-based CNS receptor ligands: have there been any advances?*, Eur J Nucl Med, 29 (2002), pp. 263 – 275.

[43] M. H. Kalos and P. A. Whitlock, *Monte Carlo methods*, vol. I, John Wiley and Sons, New York, 1986.

[44] C. Kamphuis, F. J. Beekman, and M. A. Viergever, *Evaluation of OS-EM for 1D, 2D and fully 3D SPECT Reconstruction*, IEEE Trans. Nucl. Sci., 43 (1996), pp. 2018 – 2024.

[45] M. S. Kaplan, R. L. Harrison, and S. D. Vannoy, *Coherent scatter implementation for SimSET*, IEEE Trans. Nucl. Sci., 45(6) (1998), pp. 3064 – 3068.

[46] M. S. Kaplan, R. S. Miyaoka, S. K. Kohlmyer, D. R. Haynor, R. L. Harrison, and T. K. Lewellen, *Scatter and attenuation correction for 111In based on energy spectrum fitting*, Med Phys Biol, 23 (1996), pp. 1277 – 1285.

[47] G. F. Knoll, T. F. Knoll, and T. M. Henderson, *Light Collection Scintillation Detector Composites for Neutron Detection*, IEEE Trans. Nucl. Sci., NS-35 (1988), p. 872.

[48] D. E. Knuth, *Seminumerical algorithms.*, vol. II, Addison Wesley, 1997.

[49] K. Lange and R. Carson, *E.M. Reconstruction algorithms for emission and transmission tomography*, J.Comput.Assist.Tomog., 8 (1984), pp. 306 – 316.

[50] P. S. Laplace, *Theorie analytique des probabilités*, vol. 7 of 2, In Oeuvres complètes de Laplace, L'académie des Sciences, Paris, 1886.

[51] C. B. Lim, L. T. Chang, and J. Jaszczak, *Performance analysis of three camera configurations for photon emission computed tomography*, IEEE Trans. Nucl. Sci., 27 (1980), pp. 559 – 568.

[52] M. Ljungberg and S. E. Strand, *A Monte Carlo program for the simulation of scintillation camera characteristics*, Comp. Meth. Prog. Bio., 29(4) (1989), pp. 257 – 272.

[53] M. Maisey, *Medicina Nuclear. Aspectos clínicos*, vol. 1, Ediciones Doyma, 1st ed., 1983.

[54] S. H. Manglos, C. E. Floyd, R. J. Jaszczak, K. L. Greer, C. C. Harris, and R. E. Coleman, *Experimentally measured scatter fractions and energy spectra as a test of Monte Carlo simulations*, Phys.Med.Biol., 32 (1987), pp. 335 – 343.

[55] S. R. Meikle, *Quantitative emission computed tomography using simultaneous emission and transmission measurements*, PhD thesis, University of NSW, 1994.

[56] C. E. Metz, F. B. Atkins, and R. N. Beck, *The geometric transfer function component for scintillation camera collimators with straight parallel holes*, Phys. Med. Biol., 25 (1980), pp. 1059 – 1070.

[57] Y. Narita, S. Eberl, H. Iida, B. F. Hutton, M. Braun, T. Nakamura, and G. Bautovich, *Monte Carlo and experimental evaluation of accuracy and noise properties of two scatter correction methods for SPECT*, Phys. Med. Biol., 41 (1996), pp. 2481 – 2496.

[58] W. R. Nelson, H. Hiayama, and D. O. Rogers, *The EGS4 code system*, Stanford Linear Accelerator Center Report SLAC-265, (1985).

[59] J. L. Neumeyer, S. Wang, and R. A. Milius, *N-omega-fluooalkyl analogs of (IR)-2 beta-carbomethoxy-3 beta-(4-iodophenyl)-tropane (beta-CIT): radiotracers for positron emission tomography and single photon emission computed tomography imaging of dopamine transporters*, J Med Chem, 37 (1994), pp. 558 – 561.

[60] K. Ogawa, Y. Harata, T. Ichihara, A. Kubo, and S. Hashimoto, *A practical method for position-dependent Compton-scatter correction in SPECT*, IEEE Trans. Med. Imag., 10 (1991), pp. 408 – 412.

[61] D. Pareto, *Processament d'estudis de SPECT cerebral. Reconstrucció, quantificació i estandardització*, PhD thesis, Unitat de Biofísica i Bioenginyeria. Dpt. Ciencies Fisiologiques I. Facultat de Medicina. Universitat de Barcelona, 2002.

[62] D. Pareto, A. Cot, C. Falcon, I. Juvells, J. Pavia, and D. Ros, *Geometrical Response Modeling in Fan-beam collimators. A numerical simulation*, Trans. Nucl. Sci., 49 (February 2002), pp. 17 – 24.

[63] D. Pareto, A. Cot, J. Pavia, C. Falcon, I. Juvells, F. Lomeña, and D. Ros, *Iterative reconstruction with compensation of the spatial variant fan beam collimator response in neurotransmission SPET imaging*, submitted to Eur J Nuc Med, (2003).

[64] D. Pareto, J. Pavia, I. Juvells, C. Falcon, A. Cot, and D. Ros, *A numerical simulation of PSF in fan beam collimators*, Abstracts in European Journal of Nuclear Medicine, 27(8) (2000), p. 1192.

[65] ——, *Characterization of fan beam collimators*, Eur J Nuc Med, 28 (2001), pp. 144 – 149.

[66] D. Peña, *Estadística. Modelos y Métodos*, vol. 1 of 1, Alianza Universidad Textos, 1, 11 ed., 1999.

[67] P. Photonics, ed., *Photomultiplier tubes, principles and applications*, vol. 1 of 1, Philips Export B.V., F-19106 Brive(France), 1 ed., 1994.

[68] L. S. Pilowsky, *Probing targets for antipsychotic drug with PET and SPET receptor imaging*, Nucl. Med. Comm., 22 (2001), pp. 829 – 833.

[69] C. Prunier, P. Payoux, D. Guilloteau, S. Chalon, B. Giraudeau, C. Majorel, M. Tafani, E. Bezard, J. P. Esquerré, and J. L. Baulieu, *Quantification of Dopamine Transporter by 123-I-PE2I SPECT and the Noninvasive Logan Graphical Method in Parkinson's Disease*, J. Nuc. Med., 44 (2003), pp. 663 – 669.

[70] P. Radau, R. Linke, P. J. Slomka, and K. Tatsch, *Optimization of automated quantification of 123I-IBZM uptake in the striatum applied to parkinsonism*, J. Nucl. Med., 41 (2000), pp. 220 – 227.

[71] L. Sachs, *Estadística aplicada*, vol. 1 of 1, Editorial Labor, 1, 4 ed., 1978.

[72] F. Salvat and J. M. Fernandez-Varea, *Semiempirical cross sections for the simulation of the energy loss of electrons and positrons in matter*, Nucl. Instrum. and Meth, B63 (1992), pp. 255 – 269.

[73] F. Salvat, J. M. Fernández-Varea, E. Acosta, and J. Sempau, *PENELOPE – A Code System for Monte Carlo Simulation of Electron and Photon Transport*, Nuclear Energy Agency (OECD/NEA), Issy-les-Moulineaux, France, 2001.
Available in pdf format on the web at `http://www.nea.fr`.

[74] F. Salvat, J. M. Fernandez-Varea, J. Baro, and J. Sempau, *PENELOPE, an algorithm and computer code for Monte Carlo simulation of electron- photon showers*, Informes Técnicos CIEMAT, 799 (1996).

[75] S.Bullich, D.Ros, A.Cot, C.Falcon, A.Muxi, and J.Pavia, *Dynamic model of the left ventricle for use in simulation of myocardial perfusion SPECT and*

gated-SPECT Submitted and accepted to Medical Physics, Med. Phys., accepted (2003).

[76] J. Sempau, E. Acosta, J. Baro, J. M. Fernandez-Varea, and F. Salvat, *An algorithm for Monte Carlo simulation of coupled electron-photon transport*, Nuclear Instruments and Methods, B132 (1997), pp. 377 – 390.

[77] L. A. Shepp and Y. Vardi, *Maximum likelihood Reconstruction for emission tomography*, IEEE Trans. Med. Imag., 1 (1982), pp. 113 – 122.

[78] R. L. Siddon, *Fast Calculation of the exact radiological path for a Three-Dimensional CT Array*, Med. Phys., 12 (1985), pp. 252 – 255.

[79] M. R. Spiegel, *Manual de formulas y tablas matematicas*, vol. 1, Mc Graw Hill, New York, 2 ed., 1970.

[80] K. Tatsch, *Imaging of the dopaminergic system in parkinsonism with SPET*, Nucl. Med. Comm., 22 (2001), pp. 819 – 827.

[81] ——, *Can SPET imaging of dopamine uptake sites replace PET imaging in Parkinson's disease?*, Eur J Nucl Med, 29 (2002), pp. 711 – 714.

[82] B. M. W. Tsui, E. C. Frey, X. Zhao, D. S. Lalush, R. E. Johnston, and W. H. McCartney, *The importance and implementation of accurate 3D compenstion methods for quantitative SPECT*, Phys. Med. Biol., 39 (1994), pp. 509 – 530.

[83] B. M. W. Tsui and G. T. Gullberg, *The geometric transfer function for cone and fan beam collimators*, Phys. Med. Biol., 35 (1990), pp. 81 – 93.

[84] D. J. D. Vries, S. C. Moore, R. E. Zimmerman, S. P. Mueller, B. Friedland, and R. C. Lanza, *Development and Validation of a Monte Carlo Simulation of Photon Transport in an Anger Camera*, IEEE Trans. Med. Imag., 9 (1990), pp. 430 – 438.

[85] W. B. Walters and R. A. Meyer, *Levels of ^{123}Te and ^{125}Te and the decay of 13.3h ^{123}I and 2.7 yr ^{125}Sb*, Phys. Rev. Comm., (November 1976), pp. 1925 – 1934.

[86] H. M. H. M. D. Yahr, *Parkinsonism: onset, progression and mortality*, Neurology, 17 (1967), pp. 427 – 442.

[87] H. Zaidi, *Relevance of accurate Monte Carlo modeling in nuclear medical imaging*, Med. Phys., 26 (1999), pp. 574 – 608.

[88] G. L. Zeng, G. T. Gullberg, B. M. W. Tsui, and J. A. Terry, *Three-dimensional iterative reconstruction algorithms with attenuation and geometric point response correction*, IEEE Trans. Nuc. Sci., 38 (1991), pp. 693 – 702.